




Advances in the study of supercooled water

Paola Gallo^{1,a} , Johannes Bachler², Livia E. Bove^{3,4}, Roland Böhmer⁵, Gaia Camisasca¹, Luis E. Coronas⁶, Horacio R. Corti⁷, Ingrid de Almeida Ribeiro^{8,b}, Maurice de Koning^{8,9,c}, Giancarlo Franzese⁶, Violeta Fuentes-Landete², Catalin Gainaru⁵, Thomas Loerting^{2,d}, Joan Manuel Montes de Oca¹¹, Peter H. Poole^{10,e}, Mauro Rovere¹, Francesco Sciortino³, Christina M. Tonauer², and Gustavo A. Appignanesi¹²

¹ Dipartimento di Matematica e Fisica, Università degli Studi Roma Tre, Via della Vasca Navale 84, 00146 Roma, Italy

² Institute of Physical Chemistry, University of Innsbruck, Innrain 52c, A-6020 Innsbruck, Austria

³ Dipartimento di Fisica, Sapienza Università di Roma, Piazzale A. Moro 5, 00185 Roma, Italy

⁴ Sorbonne Université, CNRS UMR 7590, IMPMC, 75005 Paris, France

⁵ Fakultät Physik, Technische Universität Dortmund, 44221 Dortmund, Germany

⁶ Secció de Física Estadística i Interdisciplinària-Departament de Física de la Matèria Condensada, Universitat de Barcelona, & Institut de Nanociència i Nanotecnologia (IN2UB), Universitat de Barcelona, C. Martí i Franquès 1, 08028 Barcelona, Spain

⁷ Departamento de Física de la Materia Condensada, Centro Atómico Constituyentes, Comisión Nacional de Energía Atómica, B1650LWP Buenos Aires, Argentina

⁸ Instituto de Física “Gleb Wataghin”, Universidade Estadual de Campinas, UNICAMP, 13083-859 Campinas, São Paulo, Brazil

⁹ Center for Computing in Engineering & Sciences, Universidade Estadual de Campinas, UNICAMP, 13083-861 Campinas, São Paulo, Brazil

¹⁰ Department of Physics, St. Francis Xavier University, Antigonish, NS B2G 2W5, Canada

¹¹ Pritzker School of Molecular Engineering, University of Chicago, Chicago, IL 60637, USA

¹² INQUISUR, Departamento de Química, Universidad Nacional del Sur (UNS)-CONICET, Avenida Alem 1253, 8000 Bahía Blanca, Argentina

Received 14 July 2021 / Accepted 17 October 2021

© The Author(s), under exclusive licence to EDP Sciences, SIF and Springer-Verlag GmbH Germany, part of Springer Nature 2021

Abstract In this review, we report recent progress in the field of supercooled water. Due to its uniqueness, water presents numerous anomalies with respect to most simple liquids, showing polyamorphism both in the liquid and in the glassy state. We first describe the thermodynamic scenarios hypothesized for the supercooled region and in particular among them the liquid–liquid critical point scenario that has so far received more experimental evidence. We then review the most recent structural indicators, the two-state model picture of water, and the importance of cooperative effects related to the fact that water is a hydrogen-bonded network liquid. We show throughout the review that water’s peculiar properties come into play also when water is in solution, confined, and close to biological molecules. Concerning dynamics, upon mild supercooling water behaves as a fragile glass former following the mode coupling theory, and it turns into a strong glass former upon further cooling. Connections between the slow dynamics and the thermodynamics are discussed. The translational relaxation times of density fluctuations show in fact the fragile-to-strong crossover connected to the thermodynamics arising from the existence of two liquids. When considering also rotations, additional crossovers come to play. Mobility–viscosity decoupling is also discussed in supercooled water and aqueous solutions. Finally, the polyamorphism of glassy water is considered through experimental and simulation results both in bulk and in salty aqueous solutions. Grains and grain boundaries are also discussed.

We wish to dedicate this paper to the memory of two great scientists of this field that we sadly lost this year: Prof. Charles Austen Angell (Arizona State University) and Prof. Sow-Hsin Chen (Massachusetts Institute of Technology).

^a e-mail: paola.gallo@uniroma3.it (corresponding author)

^b e-mail: iribeiro@ifi.unicamp.br

^c e-mail: dekoning@ifi.unicamp.br

^d e-mail: thomas.loerting@uibk.ac.at

^e e-mail: ppoole@stfx.ca

1 Introduction

It is well known that water plays a fundamental role in a huge number of phenomena related to our life. For this reason, the properties of water are extensively studied in many fields of research such as physics, biology, and chemistry. Fundamental studies in statistical mechanics focus on the anomalous behavior of water

that falls in a large part of its phase diagram. Many studies were addressed to the range of pressures and temperatures where liquid water can exist in a supercooled state below melting [1–5].

In fact, water presents a large number of structural, dynamic, and thermodynamic anomalies [6], including polyamorphism phenomena [7–10] and crystal polymorphs [11], the origin of which is still debated [1, 12, 13]. Many of these anomalies are more evident in the supercooled region, where the fluctuations of volume and enthalpy increase, rather than decrease as in normal, i.e., argon-like liquids [1, 14].

To explain the origin of these anomalies, four main thermodynamic scenarios have been proposed: (i) the stability-limit conjecture (SLC) [15]; (ii) the liquid–liquid critical point (LLCP) [16] hypothesis; (iii) the critical-point-free scenario (CPF) [17, 18]; and (iv) the singularity-free scenario (SF) [19, 20]. These conjectures are reviewed in ref. [1]. In Sect. 2 of this review, we discuss these scenarios in more in detail, and we show how a two-state model can describe, upon proper tuning of parameters, results that turn from the CPF scenario with a re-entrant spinodal as predicted by the SLC to a LLCP scenario. We also discuss the Widom line which is an important thermodynamic line pointing to a second-order critical point [21]. We reconsider this discussion also in Sect. 4, within the context of a cooperative model [22] reproducing all the four scenarios by tuning the HB cooperativity from zero (SF), to moderate (LLCP), to large (CPF and SLC) [23].

An ample and solid corpus of experimental and computational evidence that favors the water two-liquid scenario [16] has accumulated since its proposition; see for recent examples [24–26]. The unambiguous detection of the two intervening states is nonetheless a rather difficult task. For this reason, simulation studies are crucial in this field.

From the computational point of view, the identification of an order parameter capable of yielding clear bimodal distributions becomes crucial to firmly establish the existence of two well-defined different local environments in water, even far from the liquid–liquid critical point, and to determine their precise nature and relative abundance. Indeed, several structural indicators to quantify such molecular classes and, if possible, to classify water molecules in molecular dynamics simulations have been proposed over time [27–38]. In Sect. 3 of this review, we discuss recent developments on certain popular structural parameters as well as a brand new energy-based proposal.

In the context of the supercooled phase diagram of water, Sect. 4 is devoted to nanodroplets that can be used to bypass crystallization and Sect. 5 to cooperativity effects and their importance for the phase diagram of supercooled water and its possible scenarios.

Supercooled water is indeed very peculiar also from the point of view of its dynamical properties that

were studied with both simulations and experiments. In 1996, it was shown with computer simulations that supercooled water behaves like a glass former that follows the mode coupling theory (MCT) in the region of mild supercooling [39, 40]. This behavior was confirmed by experiments with time-resolved spectroscopy [41]. An important link between the MCT crossover temperature and the thermodynamic singular temperature of water T_s [6] was found in those papers, underlying a clear connection between dynamical and thermodynamical quantities [39, 40]. The dynamics of supercooled water upon further supercooling crosses from that of structural relaxation to a hopping dominated dynamics and corresponding the structural relaxation time shows a crossover from a fragile to a strong behavior [42–51]. It was later found that the dynamics of supercooled water when the LLCP is present is strictly related to the presence of the Widom line, and in fact, the fragile-to-strong crossover appears on crossing the Widom line [49–53]. For a model that shows a SF scenario, it has been shown that this crossover coincides with the line of specific-heat maxima [54], see discussion in Sect. 8. Studies on the dynamics have been performed also on water confined in silica pores [46, 47, 55–57], in contact with different environments, and in solution, where signatures of a liquid–liquid transition have been found [52, 58, 59]. These studies show that also for such types of systems dynamical anomalies are closely related to peculiar thermodynamic behavior. In Sect. 6, we review the main results on the slow translational dynamics of water in the supercooled regime. In Sect. 7, we review the results on the connections between dynamics and thermodynamics.

Experiments on water confined in silica pores [46, 47, 60–62], water hydrating lysozyme proteins [63, 64], and DNA [65] show dynamic crossovers. Although the interpretation of these results is debated [66, 67], they are confirmed by simulations of water hydrating pores [57], trehalose [68, 69] lysozyme [70–72], and DNA [73]. In particular, molecular dynamics simulations show two distinct translational slow relaxations for density fluctuations of lysozyme hydration water [70–72] and trehalose hydration water [68, 69]. Further experiments for lysozyme at low hydration reveal the occurrence of two distinct dynamic crossovers for the proton relaxation time in the supercooled regime [74]. In Sects. 7 and 8, we review results on both the translational and the rotational dynamics of water hydrating biomolecules. In Sects. 9 and 10, we review the diffusion anomaly and the decoupling of translation and rotation both in water and in aqueous solutions.

Research on amorphous ices is often carried out with the goal to understand water's liquid state. This approach assumes a thermodynamic connection between amorphous water and the supercooled liquid [3]. In this view, amorphous ices represent immobilized, low-temperature proxies of liquid H_2O . In Sect. 11 and

in Sect. 12, we describe recent experimental and simulations results on this topic.

Water in nature always contains dissolved ionic species which play a crucial role in various chemical and biological phenomena occurring in aqueous environments. For this reason, the study of aqueous ionic solutions has attracted over the years disparate communities with complementary interests and approaches. Ice nucleation is strongly affected by the presence of ionic species as the electric field generated by the ions prevents the water dipole from locally arranging in stable ordered structures. Solvation of salts in water depresses indeed the freezing point temperature and favors disordered phases and vitrification. For this reason, salt solutions have been largely investigated since the pioneering studies of Angell and Kanno [75–82] to circumvent the no-man’s land impenetrability and address the thermodynamic and structural properties of deeply supercooled water [1], in regions not otherwise accessible because of ice nucleation. In Sect. 13, we describe the structural transformations of LiCl aqueous solutions upon cooling.

Due to the relevance of glaciers and ice sheets to the Earth climate, it is fundamental to model and understand how these large ice masses behave. In this context, the study of mechanical deformation processes is an important step. For instance, grain-boundary (GB) sliding during polycrystalline ice flow is one of the mechanisms of creep [83]. From the microscopic point of view, GB melting or interfacial melting [84–87] is one of the most important and least studied subjects of pre-melted ice [84,88,89]. The challenge lies in directly observing the networks composed by the GBs in ice at the molecular level. On the other hand, computer simulations can provide unique views of structural changes that occur during pre-melting. We describe the results of a simulation in Sect. 14.

We close this review with the last section Conclusions and Perspectives (Sect. 15).

2 Two-state models and water thermodynamic scenarios

Ongoing research continues to clarify the range of permissible thermodynamic scenarios that might correspond to the behavior of supercooled water and water-like liquids.

In the liquid–liquid critical point (LLCP) scenario [16], there is a liquid–liquid first-order phase transition ending in a critical point occurring deep into the supercooled liquid region of the water phase diagram. The LLCP would generate critical thermodynamic fluctuations in a region that could be explored in experiments. The scenario occurs in ST2-water [16,90–94], in TIP4P/2005 and TIP4P/Ice [95], and it is consistent with other water models and experiments [1]. The low-density state is characterized by a short-range tetrahedral order, while in the high-density state, the

molecules are arranged in a more disordered local structure. Starting from the LLCP, maxima of the correlation length exist in the one phase region defining the so-called Widom line. In proximity of the Widom line, maxima of the thermodynamic response functions, like specific heat and isothermal compressibility, are also present and converge to the Widom line close to the critical point [21,52]. Since this phenomenology is typical of a critical point, a Widom line has been found also in the supercritical region above the liquid–gas critical point of water [96,97]. The experimental studies of water inside the deep supercooled region have long been hampered by the high crystallization rate of water, and only recently, the Widom line has been detected at $p = 1$ bar [25]. For this reason, the computer simulation studies have been very useful to identify this important line in the research on this topic [1].

In the critical-point-free (CPF) scenario [17,18], the liquid–liquid phase transition extends to negative pressure until it crosses the superheated liquid–gas spinodal [18]. This scenario has been related to the dynamic transition discussed for supercooled water.

In the stability-limit conjecture (SLC) [15], the liquid–gas spinodal extends to negative pressures and reenters from negative to positive pressure as the limit of stability of the liquid with respect to another liquid phase. This spinodal at positive P would be responsible for the anomalous increase of thermodynamic fluctuations [98]. Such a scenario has been realized in a patchy particles [99], but not for water models.

The singularity-free (SF) scenario [19,20] is the only one without singular behavior, and the hydrogen bonds (HB) are solely responsible for the volume–entropy anticorrelation. This would be the origin of the large low- T thermodynamic fluctuations. In the other three scenarios, the anomalous fluctuations in the supercooled region of the phase diagram are hypothesized to be associated with the coexistence of two liquid phases.

A valuable approach for developing and understanding the four scenarios has been the study of analytic thermodynamic models for water-like systems. An important class of such models are so-called two-state models which hypothesize an equilibrium between LDL-like and HDL-like local environments at the molecular scale; see Refs. [37,100–104] for recent examples. As the LDL-like and HDL-like fractions vary with temperature T and pressure P , the thermodynamic anomalies of water, such as the density maximum, can be reproduced, at least qualitatively. For example, recent work by Anisimov, Caupin, and colleagues has been devoted to the thermodynamic implications of two-state models so as to reveal underlying patterns of behavior that unify the various expressions of fluid polyamorphism not only in water, but also in such systems as liquid helium and sulfur [105]. The two-liquid picture also emerges from experiments, see, for example, Refs. [106,107].

Of the four scenarios for supercooled water listed above, the SLC was developed first [6,15], but was subsequently ruled out as a viable option because it predicts the intersection of the metastable extension of the

liquid–gas binodal with the re-entrant liquid spinodal in the supercooled region [3]. Such an intersection would normally be a liquid–gas critical point, and so, the SLC was disregarded because it is difficult to imagine the physical reasons for the occurrence of such a critical point in the supercooled regime of water. However, as a counter-argument, Speedy reasoned in 2004 that a re-entrant spinodal and binodal could intersect without creating a critical point [108].

There is now renewed interest in re-entrant spinodals, stimulated by observations of these phenomena in simulations of patchy colloid systems [99] and models of silicon-like liquids at negative pressure [109,110], and by steady progress by experiments in measuring the properties of water at negative pressure [111–113]. So motivated, Chitnelawong et al. recently re-examined the thermodynamic implications of an intersection between a re-entrant liquid spinodal and the liquid–gas binodal in the supercooled region [98]. This study used a two-state model developed in 1994 [17], which reproduces the predictions of either the liquid–liquid phase transition (LLPT) hypothesis or the SLC, depending on the choice of the model parameters. Reference [98] examines in detail the evolution of the phase boundaries and spinodals present in this model when the critical point of the LLPT merges with the binodal and spinodals associated with the liquid–gas transition. The results provide a clear example of a binodal that terminates on a re-entrant spinodal at a point that is not a conventional critical point, confirming Speedy’s reasoning in 2004 [108].

The main results of Ref. [98] are summarized schematically in Fig. 1. In Fig. 1a is shown the T – P phase diagram for the LLPT hypothesis, where the binodal of the LLPT and its accompanying spinodals remain distinct from and do not intersect the binodal or spinodals of the gas–liquid phase transition. Figure 1b shows the case where the binodals of the LLPT and the gas–liquid phase transition cross. This crossing actually corresponds to a triple point. That is, under these conditions, the gas–liquid binodal divides into two distinct binodals, one corresponding to coexistence of gas and LDL, and the other corresponding to coexistence of gas and HDL. These two binodals form a triple point with the LDL–HDL binodal. The metastable extension of each binodal beyond the triple point terminates on a spinodal, but none of these terminal points (termed “Speedy points” in Ref. [98]) are conventional critical points. The reason is that only one of the two phases involved in the coexistence becomes unstable at the spinodal; the other phase remains a distinct and observable metastable phase. For example, at the red open circle in Fig. 1, the HDL phase becomes unstable, while the gas phase remains a well-defined metastable phase. This Speedy point occurs within the stability field of LDL, and so, while there is still a well-defined supercooled liquid under these conditions, it is a distinct liquid from the HDL observed at higher T .

Reference [98] thus demonstrates how the predictions of the SLC can be realized in a thermodynamically self-consistent way when both a liquid–liquid phase tran-

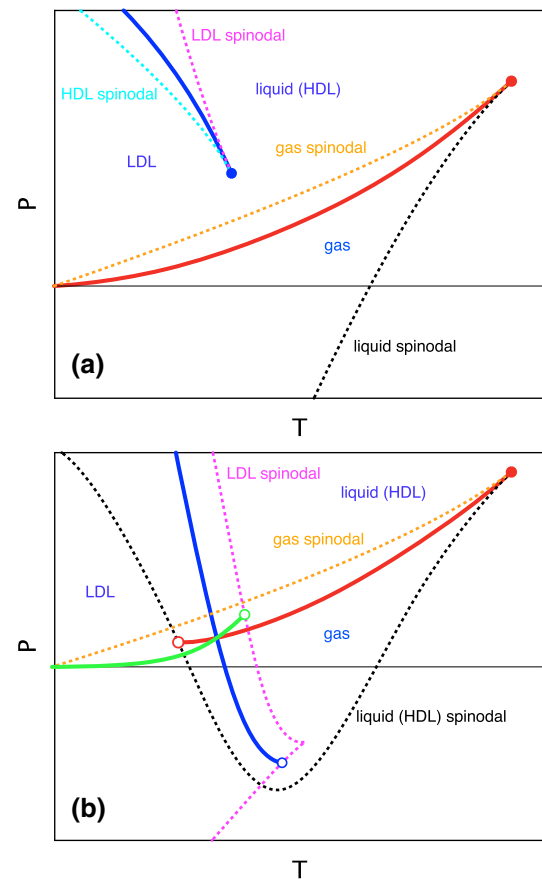


Fig. 1 Schematic T – P phase diagrams for **a** the LLPT scenario and **b** the CPF scenario with a re-entrant spinodal as predicted by the SLC. Stability regions of each phase are labeled with blue text. Filled circles are critical points, and open circles are Speedy points. Spinodals are shown as dashed lines, and binodals are shown as solid lines. The blue solid line is the HDL–LDL binodal; the red solid line is the gas–liquid/HDL binodal; and the green solid line is the gas–LDL binodal

sition and a liquid–gas phase transition occur in the same system. The phase behavior illustrated in Fig. 1b also clarifies the details of how to realize an example of the CPF scenario, since no conventional critical points occur in this phase diagram other than the gas–liquid critical point. Most estimates for the location of a liquid–liquid critical point in supercooled water suggest that the phase diagram in Fig. 1a is more likely to be relevant for the case of real water. This is also discussed in ref. [22] where the different scenarios are reproduced by tuning a single parameter in a cooperative model. Nonetheless, Ref. [98] has clarified the nature of Speedy points, which should be a relevant limiting behavior for the metastable extension of a binodal beyond a triple point in a wide range of systems, including those without water-like anomalies. In addition, the thermodynamic relationships in Fig. 1b may prove useful as more systems with re-entrant spinodals are discovered.

3 Detecting the local molecular arrangements underlying water's anomalous behavior with molecular dynamics simulations

In order to quantify the weight of the two liquids of water upon moving in the supercooled region, order parameters are extremely useful. Among all the order parameters capable of characterizing water's local molecular arrangements, the local structure index (LSI), when combined with potential energy minimization [33,34], remained for a long time as the only one able to produce clear bimodal distributions with two maxima separated by a well-defined minimum for all the different water models where it had been applied so far [33,34,114–123]. We note that, while the existence of two competing thermodynamically distinct liquid states would produce bimodal distributions of the order parameter, bimodality could also arise in other situations. The minimization procedure consists in considering not the instantaneous configurations or real dynamics but their inherent structures, IS, representing the corresponding local basins of attraction in the potential energy surface [124,125]. If instead, the LSI is calculated at the instantaneous configurations or real dynamics, the resulting distributions are not bimodal [31,32]. In practical terms, the LSI for a central molecule i at time t , $I(i, t)$, is calculated by ordering the rest of the molecules by the radial distance r_j between the oxygen of the molecule i and j : $r_1 < r_2 < r_j < r_{j+1} < \dots < r_{n(i,t)} < r_{n(i,t)+1}$, where $n(i, t)$ is chosen so that $r_{n(i,t)} < 3.7 \text{ \AA} < r_{n(i,t)+1}$. Then, $I(i, t)$ is given by:

$$LSI(i, t) = I(i, t) = \frac{1}{n(i, t)} \sum_{j=1}^{n(i, t)} [\Delta(j; i, t) - \bar{\Delta}(i, t)]^2 \quad (1)$$

where $\Delta(j; i, t) = r_{j+1} - r_j$ and $\bar{\Delta}(i, t)$ is the average over all molecules of $\Delta(j; i, t)$. Thus, $I(i, t)$ senses the inhomogeneity in the radial distribution within the sphere of radius around 3.7 \AA . A molecule i at time t with well tetrahedral local order and a low local density gives a high value of $I(i, t)$, while a molecule with defective tetrahedral order and high local density yields values of $I(i, t) \sim 0$.

Figure 2 displays the LSI distributions for two water models: SPC/E [126] and TIP4P/2005 [127]. The evident neat separation between the two peaks of the distribution not only enables an easy quantification of the two competing states (an accomplishment that can be also reached by other structural indicators provided proper deconvolution techniques are applied) but stated the LSI as the only existing structural index that provided a means to safely classify water molecules between the two states. However, a recent study has raised certain concerns on its ability to properly detect local structural ordering and to fit certain predictions of

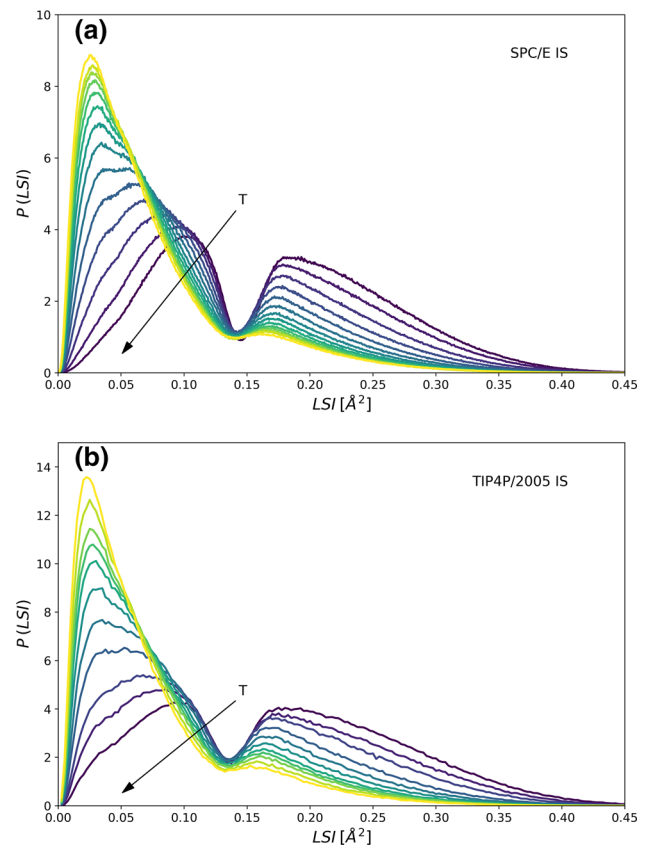


Fig. 2 LSI (at the inherent structure scheme) for SPC/E and TIP4P/2005 for a series of temperatures from below to above the corresponding melting points. The arrows depict the direction of increasing temperature. The LSI is given in units of \AA^2

the two-state model, mainly at high temperature where thermal distortions are more important [37]. A similar critique [37] was made to the d_5 indicator (calculated simply as the distance to the fifth neighbor when the molecules are ranked in order by considering their distances to the central one), an indicator that has provided relevant information on the second critical point of water in a recent work [35]. It is also worth noting that the LSI is not a parameter-free indicator, but it depends on the threshold $r_{n(i,t)}$. Changes in this value do not modify the nice bimodality of the resulting distribution, but they do alter the positions and, more importantly, the relative populations of the two peaks [34]. Additionally, as already indicated, the LSI is sensitive to the translational order up to the second coordination shell of the central molecule. Namely, the LSI has been devised in a way to distinguish between low local density molecules, where there is a clear gap between the first and second coordination shell (as typical for well tetrahedrally coordinated molecules), and distorted high local density ones, in which one or more neighbors from the second shell have collapsed toward the first one (interstitial molecules). However, it is not the degree of order/disorder of the second shell what should necessarily matter, but its impact on the first

shell, particularly its effect on the hydrogen bond coordination of the central molecule, which might either energetically stabilize it in a locally favored structure or promote the rearrangement of its hydrogen bond network.

A recent advance in this field has been the introduction of the ζ index [36,37]. Similar to the LSI, this indicator also senses the translational order up to the second shell, but it additionally incorporates explicitly the role of hydrogen bonding. Specifically, the ζ index [36,37] measures the difference between the distance $d_{j'i}$ of the closest neighbor molecule j' not hydrogen bonded to the central molecule i , and the distance $d_{j''i}$ of the farthest neighbor molecule j'' that forms a hydrogen bond (HB) with molecule i : $\zeta(i) = d_{j'i} - d_{j''i}$, considering that two water molecules are hydrogen bonded when the O–O distance is lower than 3.5 Å, and the O–H...O angle is greater than 140°. While still being structurally based by definition, this index represents a conceptual advance over previous ones since it introduces the role of molecular interactions, which are expected to be at the heart of water's anomalous behavior (particularly hydrogen bonding). From a practical point of view, the ζ index has shown success in fitting the behavior predicted by the two-state model. However, the index distributions do not display the nice (two well-separated peaks) bimodality shown by the LSI for the different models applied (the ζ index shows such a kind of bimodal behavior only for TIP5P water model and exclusively at low temperatures within the supercooled regime) [36,37,119,120].

Based on the above-described knowledge and leaving aside structural preconceptions, a new index has been recently built on the basis of molecular interactions, the V_4 indicator [128]. This index represents a parameter-free structural indicator for water that has provided neat bimodal distributions for the different water models studied, in both the normal liquid and supercooled regimes. Specifically, V_4 discriminates between molecules with four or more strong interactions, and molecules where the local tetrahedral coordination is distorted since the fourth attractive interaction is not compatible with a good quality hydrogen bond (undercoordinated molecules) [128]. Thus, while being successful in estimating the fractions of the two competing local molecular arrangements, V_4 accurately classifies water molecules within these two kinds of species [128]. Moreover, when calculated for inherent structure configurations, it corrects the tendency to overestimate the fraction of understructured molecules (in which former indicators incur) by discriminating between mere thermal distortions from truly structural changes [128]. This is central both to properly rationalize water's structure since the undercoordinated molecules are responsible for the salient peaks in the radial distribution functions, and also for dynamics, since undercoordinate and overcoordinate molecules are expected to become key defects that enable the hydrogen bond rearrangement events that trigger water's relaxation dynamics [129–131].

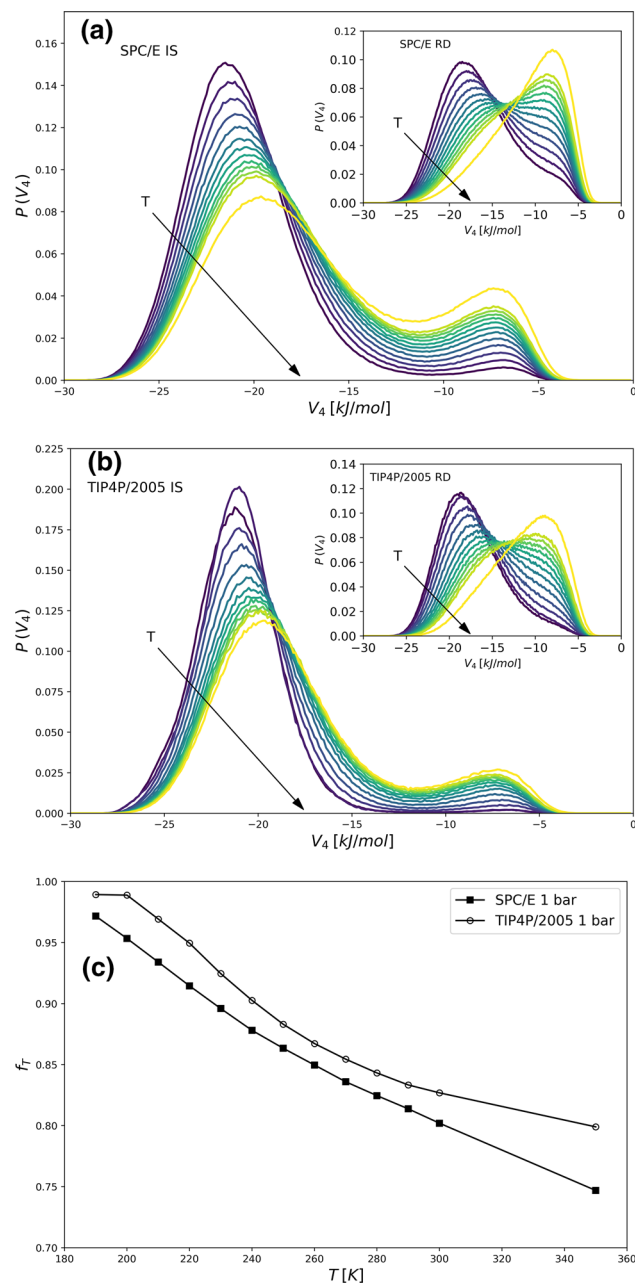


Fig. 3 **a** V_4 for SPC/E and **b** TIP4P/2005, both for inherent structures (main), and equilibrium configurations (inset) and at 1 bar. The temperature ranges go from 190K to 350K in both water models. The arrows depict the direction of increasing temperature; **c** fraction of T and D molecules as a function of temperature

Figure 3a and b illustrates the V_4 distributions for SPC/E and TIP4P/2005, respectively, for several temperatures (above and below the corresponding melting points), both at the instantaneous and at the IS configurations. Neat bimodal distributions are evident for the two schemes and models. The energy minimization improves the interactions of the molecules under the low-energy peak moving such peak to the left, while the position of the other peak is not altered. The molecules

under the peak of the left at the IS scheme present a fourth neighbor interacting with an energy of around the typical value for a good quality linear hydrogen bond, thus implying the existence of a first coordination shell close to the optimal tetrahedral bonding geometry and, as such, were termed as T (tetrahedral) molecules. The left peak includes also a small fraction of overcoordinated molecules (which at supercooled temperature becomes comparable with the fraction of undercoordinated molecules). The high-energy peak of the IS distribution, in turn, implies the existence of molecules with a distorted hydrogen bond coordination which were called D molecules (distorted or defect molecules). The two species inter-convert in time at a fixed temperature, but the relative abundance of T and D molecules significantly varies with temperature (Fig. 3c). Since the T molecules are the dominant population at the IS, even above the melting temperature, water can be described as a random tetrahedral network with relatively few network defects, the number of which increases as the temperature is raised. In this picture, the low-density liquid, LDL, consists of a virtually pure T phase, while the high-density liquid, HDL, is a mixture of a few defect molecules surrounded by T ones.

While additional work is still needed, the clear-cut parameter-free V_4 indicator has already yielded very relevant information for the two-liquid picture [128]. For instance, work with this indicator has found remarkable similarity of the oxygen–oxygen radial distribution functions (RDFs) of T and D molecules with experimental low- and high-density amorphous ices [132] (LDA and HDA), respectively. This fact evidences the high- and low-density liquid equilibrium (HDL–LDL equilibrium) as a thermally distorted version of the HDA–LDA equilibrium. The structure of the D molecules has also been found to be quite well defined and temperature independent (from total energy profile and partial RDFs information), while these molecules seem to significantly cluster as temperature is lowered [128]. Additionally, the employment of this index has been successful in explaining the anomalous rise in the isobaric heat capacity (C_p) of water at low temperature: since both local molecular arrangements display normal liquid behavior, the anomaly can be explained as resulting from the inter-conversion between both kinds of molecular classes [128].

4 Supercooled nanodroplets

Studies of micro- and nanoscale droplets of water have provided significant insights over the past decade. Small water droplets are common in natural and industrial contexts and are especially important for understanding the atmosphere and climate as well as droplet infections in virology. Droplets are valuable in the study of supercooled water because they naturally resist crystallization, relative to bulk samples, due to a combination of finite size and surface effects [133–135]. Notably, micron-scale droplets were used in recent experimental

work presenting evidence for a maximum of the isothermal compressibility of deeply supercooled water and identify this maximum with the Widom line [2, 25].

Not only can water droplets be cooled to lower T than bulk water, but also the Laplace pressure inside nanoscale droplets can be significantly greater than ambient. Li et al. have shown that the Laplace pressure inside nanodroplets is high enough to contribute to suppressing ice formation [136]. In a series of recent works, Malek, Saika-Voivod, and coworkers have studied the nature and implications of the Laplace pressure of water nanodroplets using simulations with the TIP4P/2005 potential. References [137] and [138] address methodological questions related to efficiently gathering adequate statistics from simulations of nanodroplets and clarifying the numerical evaluation of the Laplace pressure. Reference [139] then presents a detailed study of how the properties of water nanodroplets change as a function of T and the number of molecules N in the droplet. This study focuses on the supercooled region and demonstrates that the Laplace pressure reaches values as high at 2000 atm at $T = 180$ K for the smallest nanodroplets studied ($N = 100$). These are the T and P conditions at which bulk TIP4P/2005 begins to undergo a liquid–liquid phase transition, and Ref. [139] shows that the influence of the bulk LLPT on the properties of the droplets can be discerned, despite their small size.

For example, an unusual inversion of the droplet density profile occurs as the droplets cool. At high T , the density of the water inside a droplet decreases monotonically as a function of the distance r from the droplet center of mass, as would be expected for a simple liquid, as shown in Fig. 4. However, at lower T , the density of the liquid at the surface of the droplet is higher than the density in the droplet core. The behavior is consistent with the trend in bulk TIP4P/2005 water

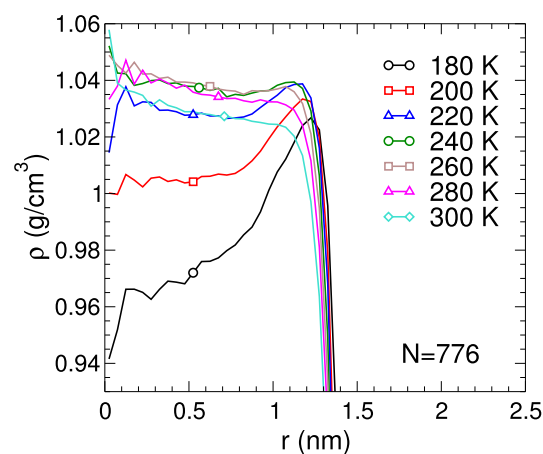


Fig. 4 Density profiles of TIP4P/2005 water nanodroplets of size $N = 776$ molecules taken from Ref. [139]. The local density ρ within the droplet is evaluated from the average volume of Voronoi cells for molecules located at a distance r from the droplet center of mass, as described in detail in Ref. [139]

that LDL forms when cooling through the Widom line associated with the LLPT. That is, a LDL-like region with a well-developed hydrogen bond network preferentially forms in the droplet core, surrounded by a surface layer in which the hydrogen bond network is disrupted, and therefore denser, due to proximity to the droplet interface with the vapor phase. However, if the droplets are small enough, the increase of the Laplace pressure on cooling is large enough to push the droplets into the regime of HDL, and consistent with this, the core switches to an HDL-like density. Reference [139] thus demonstrates that supercooled water nanodroplets display complex behavior arising from a superposition of surface effects, Laplace pressure, and the physics of the LLPT. These findings suggest that experimental characterization of supercooled water nanodroplets provides a way to search for signs of the LLPT under conditions where the bulk liquid is difficult to study due to ice crystallization [2, 25].

A related question concerns the variation of the liquid–vapor surface tension γ of water with T in the supercooled region. A number of experimental [140–142] and simulation studies [143–146] have sought to clarify what if any anomalies occur in γ for supercooled water. Upon crossing either the Widom line or the coexistence line of the LLPT, theoretical work predicts that as T decreases γ should increase faster than would be expected if there is no LLPT [147, 148]. In Ref. [149], Saika-Voivod and coworkers exploit the data obtained from their nanodroplet simulations to estimate γ for a planar liquid–vapor interface under deeply supercooled conditions. The results confirm the prediction that γ increases as T decreases at a much higher rate below the Widom line than above it. Wang et al. have also recently studied γ for supercooled TIP4P/2005 water, and they obtain a similar result [150]. Figure 5 shows the comparison of the results of Ref. [149] and Ref. [150], along with earlier higher T results from Vega and

Miguel [151]. These studies confirm that measurements of γ may be useful for seeking evidence of the LLPT in supercooled water.

5 Cooperative effects in water

Many of the most common atomistic models assume that all water interactions are strictly pairwise. This hypothesis is inconsistent with many experimental [152–157] and theoretical evidences [158–160]. For example, in their seminal paper [161], Barnes et al. showed that models containing only pair-additive interactions are not able to reproduce the correct HB interaction energy, even for small water clusters. More recently, Góra and coworkers calculated the interaction energies of large water clusters $(\text{H}_2\text{O})_n$, $n = 6, 16, 24$, from many-body expansion, up to six-body terms, based on *ab initio* potentials. They showed that for the hexamer two-body terms constitute about 82% of the total interaction energy, while three-body 17%, four-body 2%, with smaller contributions from five- and six-body terms [162]. The values for the $n = 24$ cluster change to, respectively, 74%, 23%, and 3%, with a cumulative contribution of five- and six-body terms of 0.2%, where the six-body term can be safely neglected. These results clearly show that the larger the number of water molecules in the cluster, the larger the contribution coming from terms with at least three bodies.

Researchers have explored different approaches to include the many-body interactions in water models within the classical physics approximation [163]. Depending on the level of description, we can distinguish between atomistic and coarse-grained models.

Different polarizable models [164–166] have been proposed with interesting results. Among them, the AMOEBA polarizable atomic multipole model adjusts its parameters in agreement with *ab initio* results for water clusters and experimental data over a broad temperature range to overcome the limits of the classical physics description [167]. AMOEBA is successful on protein–ligand binding and computational X-ray crystallography, but needs further tuning to describe solvation of small biomolecules, aromatic interactions, or dynamical properties away from ambient conditions [168].

The drawback for these approaches is a considerable increase of the computational cost that prevent these models to be affordable for large-size and long-time simulations. This makes them unsuitable to reach the thermodynamic limit needed in phase transitions studies or to adopt them in large-scale biological computations. Furthermore, energy decomposition analysis, including charge densities from density functional theory calculations for cyclic water trimer and tetramer, suggests that charge transfer is the leading source of cooperativity, while polarization effects have only marginal influence [169]. Hence, although sophisticated, polarizable models could be insufficient to include the cooperative effects.

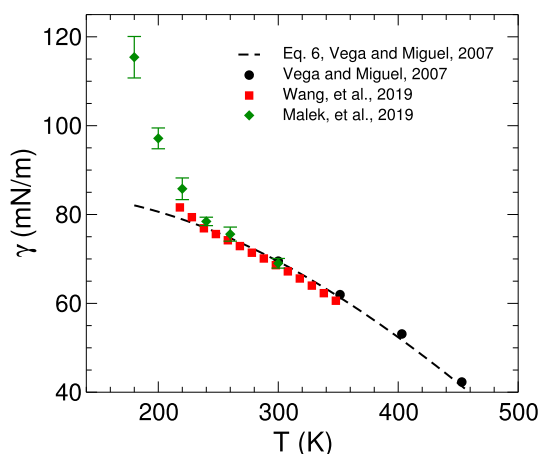


Fig. 5 Comparison of estimates for γ for TIP4P/2005 from Refs. [149–151]. The dashed line is taken from Ref. [151] and provides an extrapolation into the supercooled region based on data obtained at higher T . The data from Ref. [149] are the same as the green points shown in Fig. 5b of that work

At a more coarse-grained level, molecular models with explicit three-body interactions [170] have been used for studies related to the water phase diagram [171] and, in particular, crystal phases [172, 173]. However, the metastable supercooled region of the water phase diagram is almost inaccessible to these models [1]. Indeed, they overestimate the water diffusion constant, even after machine-learning parameter refinement [174], on a large range of temperatures, making water dynamics too fast [1]. One possible reason for this is that they assume that many-body interactions with order higher than three are negligible. This hypothesis is debatable and not necessarily true [162]. For example, estimates on the minimum-energy configurations of water clusters $(\text{H}_2\text{O})_n$, for $n \leq 21$, calculated with non-polarizable and polarizable models, find structural differences only for clusters with $n \geq 5$ [175, 176]. These works support the hypothesis that five-body contributions are relevant at low T .

An alternative approach consists in adopting a Landau-type mean-field free energy based on the two-state model introduced by Rötgen for water in 1892 [177] and, later, modified adding cooperativity by Strässler and Kittel for general order–disorder transitions in 1965 [178]. The two-state model assumes that liquid water (or any other liquid) is made of subsystems, each in one of two states with different local properties, such as density, energy, and degeneracy. If x is the fraction, or concentration, of liquid subsystems with lower energy, $1-x$ is the fraction of those in the liquid excited state. If there is no cooperativity, the total free energy is given by a linear combination of those associated with each liquid state. If a cooperativity parameter larger than zero is introduced as an effective interaction among different liquid states, then the total free energy is quadratic in x to the leading order. Strässler and Kittel demonstrated that, given a nonzero cooperativity, depending on the choice of the phenomenological parameters, the quadratic free energy can give rise to a transition between two phases, each in one of the two states, and that the phase transition can be first or second order [178]. If x is an order parameter characterizing the liquid as in the Rötgen model, this approach is able to reproduce the different scenarios for water, i.e., the SF, the LLC, the CPF, or the SLC, depending on the choice of the model parameters and, in particular, the cooperative parameter. These results have been shown with different flavors in a series of insightful papers by Tanaka, without cooperativity [179] and with cooperativity [180], and, in a less direct way, by Poole et al. [17]. In Ref. [17], although the authors state in a note that there is “lack of cooperativity” in their treatment, the cooperative parameter is given by the width of the phenomenological Gaussian that defines the range of volumes over which a significant fraction of HBs is in the state with lower energy, density, and degeneracy. As we will discuss in the following, the same kind of free energy—i.e., quadratic in the two-state order parameter and with a tunable cooperativity—can be derived starting from a molecular Hamiltonian of the HBs, instead of assuming, directly, a Landau-type expression for it.

The starting point is the Sastry et al. Hamiltonian model for water [181]. This model assumes that the total water volume is given by two contributions: one associated with the van der Waals interaction among water molecules, as in a lattice-gas for a simple liquid, another coming from the directional interaction of the HBs. When a HB is formed, the bonded molecules are in a state of (a) low density, because of the HB volume contribution, (b) low energy, because of a pairwise interaction among molecular bonding variables, and (c) low degeneracy, because the bonding variables have much less bonded configurations than non-bonded. With these minimal hypotheses, this elegant model can be solved in a molecular field approximation, generating a Gibbs free energy that has the features of those without cooperativity, as discussed above within the approach à la Landau. Its free energy qualitatively rationalizes the water density anomaly and the large increase of the response functions at low temperature, as in the experiments for liquid water near and below the melting temperature, without the need of any thermodynamic singularity (SF scenario) [181].

To include the effect of cooperativity, Franzese, Stanley (FS), and coworkers added to the Sastry et al. Hamiltonian a term that gives rise to an effective many-body interaction, up to the order of the five molecules comprised in the first coordination shell of a water molecule. The FS model, suitable for analytic calculations [21, 182, 183] and Monte Carlo (MC) simulations [74, 184–190], is described in details elsewhere [74, 184, 187, 190–192]. It coarse-grains the water molecules positions, introducing a density field, but takes into detailed account the HBs contributions that generate local heterogeneities in the density. Thanks to an efficient cluster MC algorithm [193, 194] based on a percolation mapping [195], the FS model can equilibrate in the supercooled regime of liquid water and at extreme pressures P .

As in the Sastry et al. Hamiltonian, the FS model has a parameter, v_{HB} , accounting for the local change of volume due to HB formation, and another, J , that is the characteristic energy excitation for breaking a directional HB. Furthermore, it has an additional cooperativity parameter, J_σ , that is the characteristic energy of the many-body (non-additive) interaction. To analyze the effect of the cooperativity in water, J_σ can be tuned. However, the physical constrain $J_\sigma \ll J$ must hold always, because it corresponds to the fact that the HB cooperativity is relevant only when the HBs are formed [192].

The FS model has been studied to reveal the influence of the cooperativity in the phase diagram [22], the dynamics of hydration water [23, 74, 185, 186], and to rationalize the water diffusion anomaly in terms of cooperative rearranging regions [188]. In particular, the model reproduces the different scenarios of supercooled water by tuning the relative values of J_σ and J (Fig. 6).

For $J_\sigma = 0$, the FS model is, by definition, the same as the Sastry et al. model for the SF scenario. For moderate cooperativity, i.e., $0 < J_\sigma \lesssim J/2$, a liquid–liquid

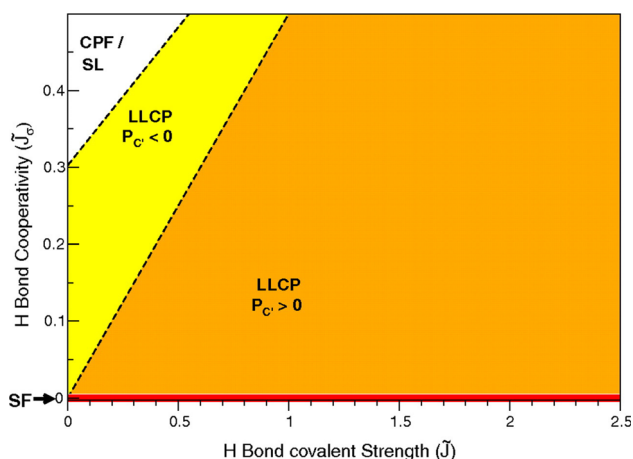


Fig. 6 Accessible thermodynamic scenarios for the FS model for different values of the covalent (directional) component and cooperative component of the HBs, when the other parameters of the model (e.g., v_{HB}) are constant. Respectively, \tilde{J} and \tilde{J}_σ are J and J_σ in units of the van der Waals energy (energy parameter of the Lennard–Jones potential). The SF scenario corresponds to the case $\tilde{J}_\sigma = 0$ for any \tilde{J} (red line). For any $\tilde{J}_\sigma > 0$, the system displays a liquid–liquid phase transition. Depending on the values of \tilde{J} and $\tilde{J}_\sigma > 0$, the phase transition ends in a LLCP with positive, or negative critical pressure $P_{C'}$ (orange region, or yellow region, respectively), or at the liquid–gas spinodal, as in the CPF scenario (white region). In the latter region, the liquid spinodal retraces to negative pressure as in SL conjecture. Dashed lines are calculated by mean field and verified by MC calculations. Reprinted figure from [22]

phase transition occurs at positive pressure and ends in a critical point, as in the LLCP scenario. Within this range of values for J_σ , the larger is J_σ , the lower is P and the higher is T of the LLCP. For larger values ($J_\sigma \gtrsim J/2$), the LLCP occurs at negative pressure and, for increasing J_σ at any constant J , the LLCP approaches the liquid-to-gas stability limit under tension.

This is true until, for large-enough HB cooperativity, the liquid–liquid phase transition reaches the limit of stability of the liquid and the LLCP is no longer accessible. This case corresponds to the CPF scenario. The FS model under these conditions shows that the liquid-to-gas spinodal, with positive slope in the P – T thermodynamic plane, merges with the liquid-to-liquid spinodal, with negative slope in the P – T plane. As a consequence, the two merging spinodals give rise to a re-entrant fluid-to-fluid spinodal, as in the SL conjecture.

Therefore, the FS model shows that all the scenarios can be understood as a consequence of the same mechanism, controlled by the amount of cooperativity of the HB interaction. The four are plausible, and which one is the correct scenario for water depends, within this framework, on how strong is the cooperative HB component, if any. According to estimates for the cooperative HB contribution made from experimental data [196–

200], Stokely et al. conclude that the scenario holding for supercooled liquid water has the LLCP at positive pressure [22].

6 Mode coupling interpretation of water dynamics and fragile-to-strong transition in water

Thermodynamic features and structural modifications that water shows in the supercooled region appear to be strongly interconnected to its slow glassy dynamics and to dynamical crossovers.

When the slow dynamics of a liquid is studied, one of the most used physical quantities is the self intermediate scattering function (SISF), which is the spatial Fourier transform of the self density correlation function. This quantity can be directly calculated with molecular dynamics simulations, and it is also the time Fourier transform of the dynamical structure factor that can be measured with quasi-elastic and inelastic neutron scattering. The SISF probes the dynamics of the atoms or molecules of the liquid, and it is given by:

$$F_s(q, t) = \frac{1}{N} \sum_{i=1}^N \langle \rho_q(t) \rho_{-q}(0) \rangle = \frac{1}{N} \sum_{i=1}^N e^{i\mathbf{q} \cdot [\mathbf{r}_i(t) - \mathbf{r}_i(0)]}, \quad (2)$$

where $\rho_q(t)$ is the Fourier q -component of the microscopic density at time t , \mathbf{q} is the exchange wave vector, and $\mathbf{r}_i(t)$ the position of the atom or of the molecule at time t .

The most general feature of supercooled and glassy dynamics of liquids is the developing upon cooling of a two-step relaxation decay and the stretching of the slowest relaxation over decades in time upon decreasing temperature in the time correlation functions.

The mode coupling theory (MCT) [201,202] interprets the slow dynamics of water in the mild supercooled regime. The idea behind the MCT is the cage effect, a transient trapping of a particle of the liquid by its nearest neighbors. When the temperature of the system is lowered at constant pressure, a particle remains trapped by the cage formed by neighbors for longer and longer time. Correspondingly, the SISFs do not change with time and a plateau develops for the time the particle is confined inside the cage. When the cages relaxes, the particle is free to move and the correlators slowly decay to zero. Eventually, in the idealized version of the theory, this trapping leads to the complete structural arrest of the liquid at the MCT temperature T_C and below because all cages are frozen. This means that below T_C the ideal system turns to a glassy state.

As stated in “Introduction,” in 1996 the MCT behavior was first observed in water by Gallo et al. [39] and Sciortino et al. [40]. In these seminal studies, the appearance upon supercooling of two-step relaxation

and the cage effect of water simulated with the SPC/E model was shown.

They used the following formula to describe the analytic form of the translational SISF which takes into account the MCT prediction:

$$F_s(q, t) = (1 - f_q)e^{-(t/\tau_s)^2} + f_q e^{-(t/\tau)^\beta}. \quad (3)$$

The Gaussian function with time constant τ_s takes into account the initial ballistic motion inside the cage, while the stretched exponential function, known as the Kohlrausch–Williams–Watts function, takes into account the structural α -relaxation, with time constant τ and the stretching parameter $\beta < 1$ that indicates a stretched dynamics.

The α -relaxation behavior of supercooled water was experimentally confirmed by Torre et al. [41].

The model of Eq. 3 and the MCT predictions successfully describe the SISFs of TIP4P water [49] and TIP4P/2005 water [50] too.

In Fig. 7, we show the SISFs calculated for the oxygen atoms of water simulated with the TIP4P/2005 model [50] at $q = Q_0 = 2.25 \text{ \AA}^{-1}$, where the MCT behavior is best evident. This figure shows the behavior of this correlator for water from ambient temperature down to the supercooled regime. The TIP4P/2005 water potential is one of the most popular models for water as it is able to reproduce many experimental water quantities in a large range of temperatures and pressures [127]. For this potential, the presence of the LLCP and the Widom line has already been found in thermodynamics calculations [203] and recently rigorously confirmed [95].

We see from Fig. 7 that, as the temperature goes down, the timescale of the long-time decay becomes slower and slower with respect to the initial decay of the correlators, which weakly depends on the temperature. From the point of view of the single-particle microscopic dynamics, the first decay corresponds to the ballistic regime and the long-time decay to zero to the structural α -relaxation of the liquid. The fit of the SISFs according to Eq. 3 is shown as continuous line superimposed to the data, in the upper panel of Fig. 7.

After the fast relaxation, the SISF reaches a plateau value f_q , called non-ergodicity parameter. The relevant timescale of the slow relaxation to zero, the α -relaxation, follows, according to the MCT, a power law given by:

$$\tau \sim (T - T_C)^{-\gamma}. \quad (4)$$

T_C and γ are parameters of theory, typically dependent on pressure. We call a liquid, the relaxation time of which follows Eq. 4, a fragile liquid.

From Eq. 4, we see that upon approaching T_C from above, the α -relaxation time of the liquid becomes slower and slower and diverges at T_C : This corresponds to the transition to the glassy state, characterized by structural arrest when the SISF settles on the value of f_q ceasing to decay.

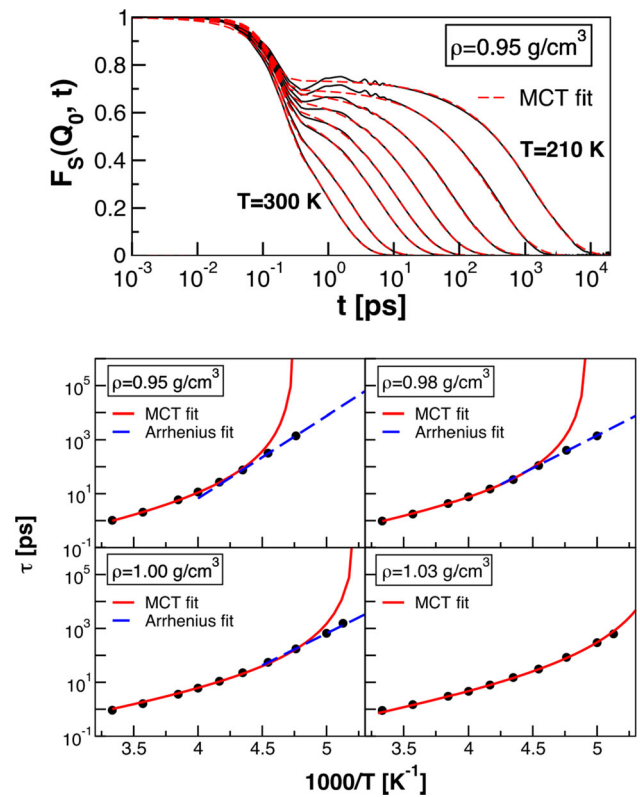


Fig. 7 Top frame: SISFs of oxygen of bulk water simulated with the TIP4P/2005 potential at $\rho = 0.95 \text{ g/cm}^3$ from 300 K down to 200 K. The red curve superimposed to the data point is the fit according to Eq. 3. Bottom frame: α -relaxation times τ as function of $1000/T$. Each panel corresponds to a different density of bulk water. The continuous red line is the MCT power law fit via Eq. 4. The dashed blue line is the Arrhenius fit via Eq. 5. The FSC takes place for $\rho = 0.95, 0.98$, and 1 g/cm^3 . The relaxation time for $\rho = 1.03 \text{ g/cm}^3$ is described by Eq. 4 in the whole interval of studied temperatures. Reprinted from [50], with the permission of AIP Publishing

From Fig. 7, we see that all the SISFs of water decay to zero. This is not because the investigated temperatures are far above T_C , but because in many liquids few degrees above T_C , new relaxation mechanisms set on and let the particle escape from the cage and the correlators decay to zero. These mechanisms are temperature activated. They are called hopping phenomena and they are included in the extended MCT. Their effect is a smearing out of the divergence of the α -relaxation time. When hopping dominates the dynamics of the liquids, the α -relaxation time is described by an Arrhenius law:

$$\tau \sim e^{-E_A/(k_B T)}, \quad (5)$$

where E_A is the activation energy of the liquid. We call a liquid whose relaxation time follow Eq. 5 a strong liquid. Therefore, for these liquids where hopping phenomena restore ergodicity, like water, the α -relaxation time shows upon cooling a crossover from the MCT

power law behavior of Eq. 4, to the Arrhenius behavior of Eq. 5. This crossover is called fragile-to-strong crossover (FSC) and takes place at a temperature T_L , inside the supercooled regime few degrees above T_C . We mention that the α -relaxation behavior of a fragile liquid, including water, can be fitted also with the Vogel–Fulcher–Tamman phenomenological formula [204]:

$$\tau \sim e^{BT_0/(T-T_0)}, \quad (6)$$

where B is the fragility parameter and T_0 is an ideal glass transition temperature located below the experimental glass transition temperature T_G , see, for example, for water [46, 47, 57]. We also note that for liquids that do not show the FSC, fragile liquids, like o-terphenyl, the VFT law is able to fit the relaxation data down to the glass transition temperature [204]. For water, this is not possible neither in experiments nor in simulations [42, 46, 47, 57].

We note that a lot of work on the slow dynamics of water was experimentally carried out by C. Austin Angell. The role of MCT in the interpretation of the experiments on supercooled liquids was already underlined by Ediger, Angell, and Nagel in their well-known review [205]. Likewise, the fragile-to-strong behavior in glass formers was extensively analyzed already in Ref. [206]. More specifically, C. A. Angell in Ref. [42] showed that water close to T_g behaves as a strong glass former suggesting a fragile-to-strong transition to match the fragile behavior of water for mild supercooling.

In the lower panel of Fig. 7, the α -relaxation times τ extracted from the SISFs of TIP4P/2005, are shown as function of the inverse temperature, for four different densities $\rho = 0.95, 0.98, 1.00$, and 1.03 g/cm^3 . In three out of the four densities studied in Ref. [50], the relaxation times of water show a FSC, which means that the behavior crosses from the MCT power law at higher temperatures to the Arrhenius law at low temperature. In the fourth case, instead, the relaxation times could be described by the MCT law in the full interval. The occurrence or non-occurrence of the crossover from power law to Arrhenius in water is related to different paths on the phase diagram of water and highlight the strong connection with the thermodynamics.

In the next section, we will discuss these connections. Before that, we want to show how the mechanism of hopping sets in for water. This phenomenon has been recently studied through the stretching dynamics of water in the oxygen van Hove self correlation functions (VHSCF), which is the Fourier transform of the SISF in the real space (r, t) .

The VHSCF of TIP4P/2005 water was investigated upon cooling in Ref. [51]. In the upper frame of Fig. 8, the svFHs calculated from molecular dynamics simulation of water at a density $\rho = 1.00 \text{ g/cm}^3$ and $T = 220 \text{ K}$ are reported. The curves are grouped in three time intervals corresponding to the three regimes of the dynamics: the short time ballistic regime (left), the cage regime (middle), and the structural relaxation regime (right). At early times, the VHSCF broadens

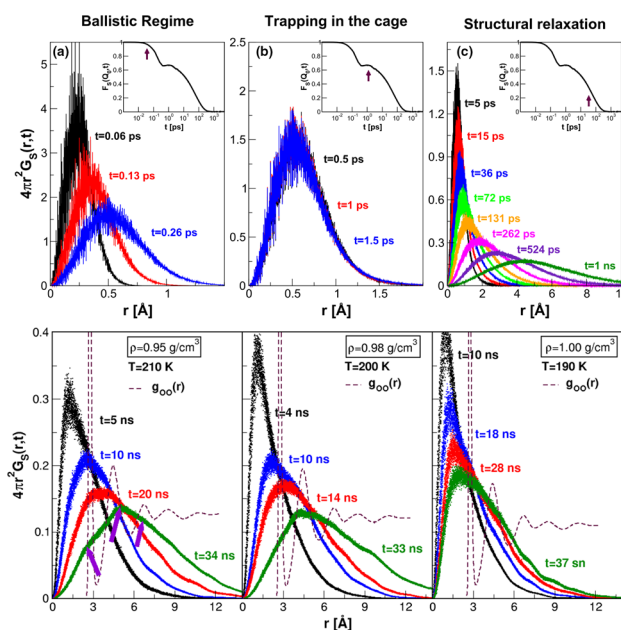


Fig. 8 Oxygen VHSCFs. Top frame: radial VHSCF at $T = 220 \text{ K}$ for density $\rho = 1.00 \text{ g/cm}^3$ for various instants of time. The VHSCF is displayed in **a** the ballistic time interval, **b** the intermediate “cage” regime, and **c** the long-time diffusive regime. In the insets, we plot the same correlator in the (Q, t) space, the self-intermediate scattering function (SISF). Each arrow marks the time region spanned by the VHSCF of the main panel. Bottom panel: radial VHSCF in the long-time diffusive regime calculated for $\rho = 0.95 \text{ g/cm}^3$, $\rho = 0.98 \text{ g/cm}^3$, and $\rho = 1.00 \text{ g/cm}^3$. For each density, the VHSCF is shown at $T = T_C$, with T_C the respective mode coupling temperature. The $g_{OO}(r)$ at T_C are also reported and rescaled to make the comparison more clear. In the first panel, arrows mark the exact position of the hopping peaks at $t = 34 \text{ ns}$. Reprinted from [51], with the permission of AIP Publishing

and its peak moves to larger distances as the time evolves, because the molecule is moving ballistically away from its starting position. This corresponds to the initial Gaussian decay of the SISFs, as highlighted in the inset. At intermediate time, the curves do not evolve in time because the water molecules are trapped inside the cage. This corresponds to the plateau of the SISFs. When the water relaxes because the cages dissolve, molecules are free to diffuse and the VHSCF at long time start to evolve again in time. In the diffusive regime, the VHSCF is well approximated with a Gaussian, so it is characterized by a single maximum evolving in time toward longer distances.

In the bottom frame of Fig. 8, the VHSCFs at very long time are shown for the three density values displaying the FSC at their respective T_C . These VHSCFs are plotted together with the oxygen-oxygen radial distribution functions, computed at the same thermodynamic conditions and rescaled by a constant factor to enhance the comparison. Below the FSC, water is behaving as a strong liquid where the dynamics is driven by hopping phenomena. In this regime, cages are

frozen and water molecules can escape the cage of nearest neighbors only by hopping toward outer coordination shells. This mechanism becomes clear in VHSCFs, when the long-time curves develop multiple peaks. As the time increases, the peaks become more pronounced. These peaks are aligned with the peaks of the radial distribution functions, which give the energetically favored positions to which water molecules can hop to.

7 Connections between dynamic crossovers of translational relaxations and thermodynamics

The results on the slow dynamics of water show that upon cooling, water always follows the predictions of the MCT in the region of mild supercooling. Depending on the thermodynamic path, water may or may not show the FSC. The four thermodynamic paths investigated in Refs. [50, 51] are shown in the phase diagram of Fig. 9 at the corresponding densities shown in the bottom panel of Fig. 7.

We see that, when the path does not intersect the Widom line, water remains a fragile liquid without showing dynamics dominated by hopping effects, down to the lowest temperature where it was possible to equilibrate the simulations. This is the case of water at $\rho = 1.03 \text{ g/cm}^3$. For the other three densities, $\rho = 0.95, 0.98$, and 1.00 g/cm^3 , we observe that the followed paths intersect the Widom line and correspondently water shows the FSC at the Widom line, and below hopping phenomena set on.

The coincidence of the occurrence of the FSC with the Widom line establishes the non-trivial connection between the dynamics and the thermodynamics of bulk

supercooled water. In the one-phase region, above the Widom line, water fluctuations are more dominated by HDL local structures, while below it they are more dominated by LDL local structures. The high-density liquid is characterized by a fragile dynamics, while the low-density liquid by a strong hopping-activated dynamics. These studies show therefore that the translational dynamics of water depends strongly on the local density experienced by the water molecules and that hopping is more favored where water is less dense. This is also confirmed by an analysis of the VHSCF for water molecules based on local order [207], showing that the dynamics is slower when the density of water decreases.

Also, the dynamics of hydration water has been studied along these lines with the density correlators [68–72, 208–210]. Recently, a study of hydration water of a globular protein, lysozyme, has been studied by means of molecular dynamics simulations both with the pure hydration water [71, 208, 211] and with water and trehalose [70, 72]. Trehalose is a disaccharide commonly used for organic cryopreservation [212]. Focusing on translational dynamics and mild supercooling, therefore on picosecond and nanosecond timescales, these studies have evidenced that after the first fast relaxation, hydration water shows two translational structural relaxations [210]. The first slow relaxation is the analogous α -relaxation of bulk water and was also measured in neutron scattering experiments for lysozyme at low hydration [213, 214]. The second one is a longer relaxation which arises from the dynamic coupling of water with the protein. The α -relaxation times are very similar to the bulk for the pure hydration water and mildly slower when trehalose is added to the solution. This relaxation shows a FSC at circa 5 degrees above the temperature of FSC for bulk water in the case of pure lysozyme hydration water. An increase of 20 degrees with respect to bulk water is found when trehalose is added to the aqueous solution. Therefore, the phenomenology of the α -relaxation is similar for bulk water and pure hydration water and qualitatively similar also when trehalose is added to the solution. A mild decrease of the activation energy on the strong side of the α -process is observed when going from bulk to pure hydration water to hydration water with lysozyme.

The long relaxation is a feature that it is present only in hydration water [71]. For pure hydration water, relaxation times are much slower than the α -relaxation times and they show a strong-to-strong crossover that coincides with the so-called protein dynamical transition [215, 216]. The protein dynamical transition is a well-known feature of hydrated proteins. Upon cooling, there is a specific temperature where the mean square fluctuations of the protein atoms become consistently inhibited. Upon addition of trehalose to the solution, the long relaxation is enormously slowed down and it keeps on showing the strong-to-strong transition in correspondence of the Protein Dynamical Transition. Correspondently, the damping of protein fluctuations below the protein dynamical transition is much more enhanced [72].

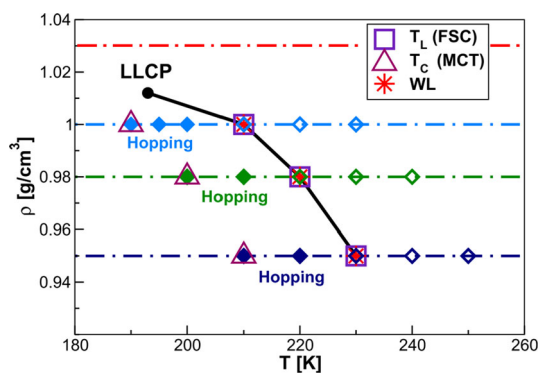


Fig. 9 ρ – T thermodynamic phase diagram containing the location of the LLCPP [203], FSC $T_L(\rho)$, MCT $T_C(\rho)$ and the Widom Line. The four isodensity paths investigated are shown with dot-dashed lines. For the three paths intersecting the WL, an empty symbol indicates that the state point is above the FSC and does not show hopping effects, while a full symbol indicates that the state point is below the FSC and water does show hopping effects. The FSC line corresponds with the Widom line. Reprinted from [51], with the permission of AIP Publishing

We also note that in protein hydration the hopping due to the α -relaxation is also present. Interestingly, additional hopping phenomena of the water molecules, connected to the long relaxation, also arise [208].

Dynamic crossovers in water are therefore also very important to assess the reciprocal influence of water and biological substrate both for translational and for rotational relaxations as also illustrated in the next Section.

We must also mention here that in the region below the MCT crossover temperature, where hopping processes dominate, a connection between thermodynamics and the VFT relation is given by the Adam–Gibbs relation that connects the viscosity to the configurational entropy [217]. The Adam–Gibbs equation is based on the concept of the cooperative rearranging regions [218].

In this context, the region below T_C is dominated by the potential-energy landscape [219–222] and the glass transition occurs at the Kauzmann temperature where the configurational entropy vanishes.

8 Two dynamic crossovers in hydrogen bond relaxation of FS hydration water

Dielectric relaxations in water probe water's dipole rotational dynamics, which occurs in the HB network [223]. As stated in “Introduction,” dielectric spectroscopy experiments for lysozyme at low hydration show two distinct dynamic crossovers for the proton relaxation time in the supercooled regime [74], at $T \sim 252$ K and $T \sim 181$ K (Fig. 10a). Crossovers at similar temperatures have been seen recently also in self-diffusion of a thin supercooled water film, layered on crystalline ice, by using a pulsed-laser-heating technique to measure the ice growth rate [224]. Simulations and mean-field calculations for hydration water represented with the FS model (Sect. 5) allow us to understand the origin of these two crossovers [23, 74, 185, 186].

In Ref. [185], Kumar et al. explore how the cooperativity affects the properties of the high- T dynamic crossover for the HB correlation time. They compare the results obtained for two thermodynamic scenarios: SF with $J_\sigma/J = 0$ and LLCp with $J_\sigma/J = 0.1$. For both scenarios, they find that the dynamic crossover occurs from a non-Arrhenius to an Arrhenius regime, and they relate its origin to the HB fluctuations due to the local rearrangement of the network. More precisely, they make four experimentally testable predictions [184, 185]. For both scenarios, (i) the time of the HB correlation at the crossover, τ_L , is independent on P (*isochronism*), (ii) the activation energy at the crossover, $E_A(P)$, decreases linearly as P increases, and (iii) the crossover temperature $T_L(P)$ decreases linearly as P increases. Additionally, they find that (iv) the fragility index $E_A/(k_B T_L)$ has a different dependence on P for LLCp and SF scenarios. For the former, it increases as P increases, but for the latter, it remains constant. Quasi-elastic neutron scattering (QENS) experiments on water hydrating lysozyme con-

firm the predictions (i)–(iii) [184, 226]. Nevertheless, they are not able to discriminate between the LLCp and SF scenarios, as the prediction of the difference between the two lays within the error bars of the experiments [184].

With further Monte Carlo simulations and mean-field calculations exploring lower T for the FS model [23, 74], Mazza et al. clarify that the high- T dynamics crossover is only apparently between a non-Arrhenius and an Arrhenius behavior, but it is in fact a non-Arrhenius-to-non-Arrhenius crossover, followed by a non-Arrhenius-to-Arrhenius crossover at lower $T \sim 181$ K (Fig. 10b), as seen in the experiments measuring the proton relaxation time of water hydrating lysozyme powder. They find that the crossover at high- T , previously reported in [185], is indeed between two Vogel–Fulcher–Tamman (VFT) behaviors. They relate the origin of the crossover at $T \sim 252$ K to a transition for the water protons from a diffusive high- T regime to a subdiffusive low- T regime. The crossover at $T \sim 181$ K is between a VFT and an Arrhenius regime. This crossover corresponds to the local rearrangement of the HBs into a tetrahedrally ordered network due to the cooperative effect. They show that these changes are not related to the interaction with the confining interface, consistent with the interpretation of recent experiments [224].

To further strengthen this interpretation, they show that the two crossovers correspond to two maxima in the specific heat C_P . The high- T C_P -maximum is originated by the P -dependent maxima of the enthalpy fluctuations due to the formation of the HB network. The low- T C_P -maximum is due to the local rearrangement of the HB network due to the cooperativity effect, and it is almost independent on P [23, 74].

9 The diffusion anomaly

The diffusion constant D of normal liquids decreases if we increase P at constant T . Experiments show that water, instead, has an anomalous P -dependence of D , with up to a 60% increment [227, 228] for increasing $P < 200$ MPa [160].

Simulations of classical [229], *ab initio* [230], or lattice [231] water models, find structural relations between the increase of D and, e.g., the HB weakening [44, 232], or the configurational entropy [221], or the orientational order [233]. Although these works include the effect of the proliferation of HB defects with increasing P on D , they do not account for the cooperative rearrangement of water under pressure.

The situation is more controversial when water is confined. For example, experiments in zeolites [234], hydrophilic nanopores [235], and hydrophobic carbon nanotubes [236] show that D decreases by orders of magnitude when the available space to water decreases. However, for water confined below 2 nm, experiments find a surprisingly fast mass transport [237]. Simulations of confined water show a similar controversy. For example, MD simulations of SPC/E-water between two

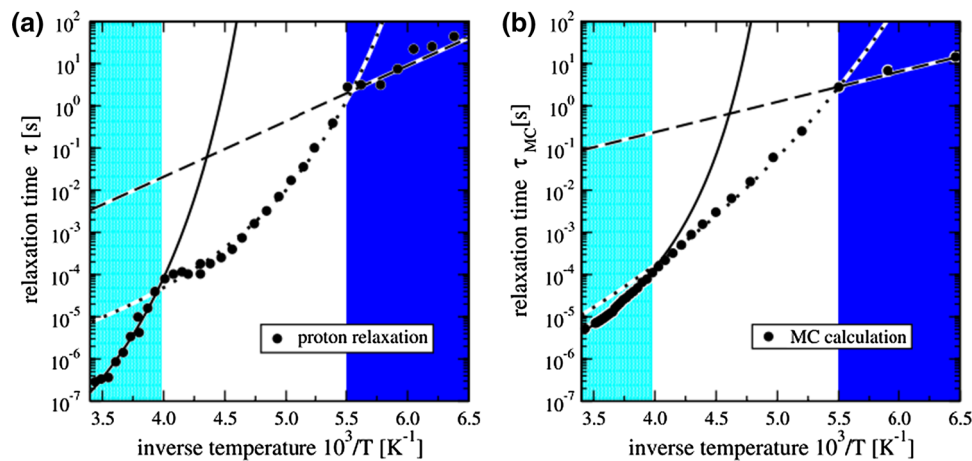


Fig. 10 Experiments and simulations showing two dynamic crossovers in the HB relaxation time τ of hydration water. The crossover at $T \sim 252$ K is from a non-Arrhenius to a non-Arrhenius regime and the crossover at $T \sim 181$ K is non-Arrhenius to Arrhenius. In both panels, solid and dotted lines are fittings to VFT behaviors, while the dashed line is an Arrhenius function. **a** Relaxation time τ from dielectric spectroscopy experiments on hydrated lysozyme, and **b** Monte Carlo calculation of the relaxation time τ_{MC} for a water monolayer. The authors relate

the differences between the two plots to two factors: (i) Experiments are carried out at constant sample hydration h , which reduces the effective P when T decreases, while simulations are performed at constant $P = 0.1$ MPa, and (ii) the fluctuations in the O–O distance and the HB network according to the FS model may enlarge the probability for a proton to be delocalized with respect to classical simulations at high- T . This effect is maximum at $T \sim 250$ K [225], close to the high- T crossover. Reprinted figure from [74]

large hydrophobic graphite-like plates display a large decrease of diffusion for separations below 1.3 nm [238], or a diffusion faster than bulk depending on the details of the numerical approach [239]. Under similar conditions, between 6 and 1.4 nm, TIP4P/2005-water shows oscillatory diffusion and rotational dynamics, with the speedups and slowdowns correlated with oscillations in structure, hydration pressure, and free energy [240]. Other authors find a similar discrepancy for carbon nanotubes with diameters below 1 nm [241–243]. In strong hydrophilic confinement, water was found to have a dichotomic behavior [55–57, 244, 245]; the first two layers close to a strongly hydrophilic surface are extremely slowed down and show subdiffusive behavior also upon supercooling (bound water). The rest of the water (free water) show dynamics that are similar to bulk water.

To contribute to this debate, de los Santos and Franzese performed simulations of a FS water monolayer, confined between hydrophobic walls at 0.5 nm distance [189]. They consider 75% hydration and, using diffusive MC, estimate $D_{||}$ according to the Einstein formula

$$D_{||} \equiv \lim_{t \rightarrow \infty} \frac{\langle |\mathbf{r}_i(t + t_0) - \mathbf{r}_i(t)|^2 \rangle}{4t}, \quad (7)$$

where \mathbf{r}_i is the projection of the position of the molecule i onto the plates. They have found that $D_{||}$ has a non-monotonic behavior, with maxima and minima along isotherms, over a P -range of about 0.1 GPa. They analyzed the anomaly in terms of the joint probability $W_{\nu,\mu}$ of finding ν molecules with (i) enough free volume avail-

able for diffusion in their surrounding and (ii) within a cooperative rearranging region (CRR) with a number μ of HBs. They have found that $D_{||}$ depends linearly on $W_{\nu,\mu}$ (Fig. 11), and that $W_{\nu,\mu}(P, T)$ depends on both (1) the average number of HBs per molecule, $\langle n_{HB} \rangle$, and (2) the free volume, $\langle n_F \rangle$, in units of average molecular volume.

This result clarifies the mechanisms of the diffusion anomaly. When P increases along an isotherm, the number of HBs $\langle n_{HB} \rangle$ decreases, and the normalized free volume, $\langle n_F \rangle$, available for diffusion increases (inset Fig. 11). Hence, the cost in energy for a molecule to move decreases, while the free-volume increase partially compensates the density increase due to pressurization. These two mechanisms cause the increment of diffusion in a limited range of T and P . Outside this region, $D_{||}$ recovers a normal behavior because the number of HB defects is small (at small P), or there are not enough HBs (at high P).

Furthermore, the analysis by de los Santos and Franzese shows that the described competition occurs within CRRs of approximately 1 nm. Hence, it explains why water under sub-nm confinement, as a consequence of the breaking of the CRRs, is dominated by single-molecule diffusion and diffuses faster than when confined above 1 nm, where the cooperative rearrangement slows it down. It is intriguing to observe that the 1-nm length scale characterizes the limit below which water loses many of its macroscopic features, including the hydrophobic effect [246].

From all the considerations presented in Sects. 5, 8, and 9, it is clear that many-body interactions play a relevant role in water, and a proper water model should

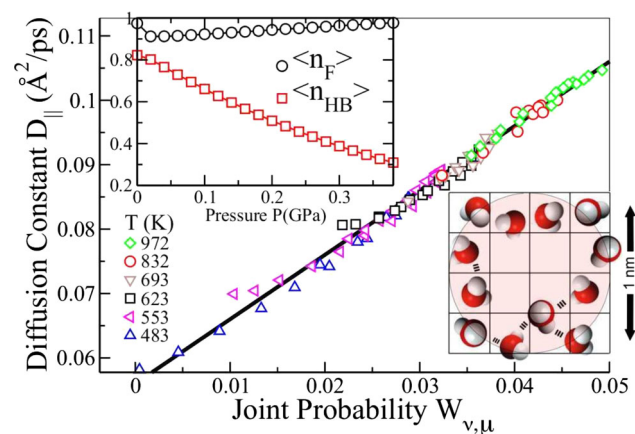


Fig. 11 Upper inset: average free volume in units of molecular volume, $\langle n_F \rangle$, and average number of HBs per molecule, $\langle n_{HB} \rangle$, at constant T as a function of P . The liquid–gas phase transition at low P results in a discontinuity in $\langle n_F \rangle$. At higher P both quantities are monotonic, but with opposite behavior. Main panel: $D_{||}(P, T)$ for six isotherms, each represented by a different symbol, collapses onto a single linear function of $W_{\nu, \mu}(P, T)$, showing that $W_{\nu, \mu}$ controls $D_{||}$. Lower inset: schematic drawing of a CRR of about 1 nm size (shaded), with $\nu = 12$ and $\mu \propto 5$ (HBs represented by thick dashed lines). Reprinted figure with permission from Ref. [189]. Copyright (2012) by the American Physical Society

include them [161, 163]. The cooperativity allows us to properly understand the rich variety of phenomena that water displays, including thermodynamic, structural and diffusion anomalies [247], as well as polyamorphism [7–10, 13]. The FS model offers a tractable way to account for these many-body correlations, namely by including them via a five-body term for the whole first coordination shell of each water molecule [23, 74, 182, 183, 185, 186, 190, 192]. It allows us to perform analytic and numerical calculations on large-scale systems, particularly relevant for biological problems [248–256]. Specifically, the findings are: (i) All the possible scenarios for water’s anomalies belong to the same framework and differ only for the amount of HB cooperativity [22] (see Sect. 5); (ii) there are two dynamic crossovers of the HB relaxation time for protein hydration water, one corresponding to the HB formation, the other, at much lower T , to its rearrangement due to the HB cooperativity [23, 74] (see Sect. 8); and (iii) the water diffusion anomaly is explained by the HB cooperative rearranging regions [188] (see Sect. 9).

10 Mobility–viscosity decoupling in supercooled water and aqueous solutions

The simplest model to describe the translational diffusivity of a spherical solute of hydrodynamic radius r in a continuum solvent having bulk viscosity η is the classical hydrodynamic model expressed by the Stokes–Einstein relationship (SER) [257]:

$$D_t = \frac{k_B T}{A \eta r}, \quad (8)$$

where k_B is the Boltzmann constant, T is the temperature, and A is a coefficient whose value depends on the boundary conditions for the interaction of the moving particle with the solvent (6π for slip or 4π for stick). The SER gives a good estimation of the diffusion coefficient for solutes with sizes much larger than that of the solvent molecules, but it fails when the size of the solute molecule approaches the size of the solvent. It also fails to describe the structural relaxation time of a glass-forming liquid, including water and aqueous solutions, when it is cooled below a temperature T_c higher than the glass transition temperature, T_g , (usually for $1.18 < T_c/T_g < 1.28$) [258], and the magnitude of the decoupling is larger for probes with smaller sizes [259]. That temperature is related to the crossover temperature where the viscosity changes from power law to Arrhenius or VFT behavior [260], and it is related to the MCT crossover temperature and to the FSC temperature described in the previous sections [258]. Below T_c the relation between the diffusion coefficient and the viscosity follows a fractional Stokes–Einstein relation (FSER)

$$\frac{D}{T} \propto \left(\frac{1}{\eta} \right)^\alpha, \quad (9)$$

where α is a temperature-independent decoupling factor ($0 \leq \alpha \leq 1$). The lower is the α , the stronger is the diffusion–viscosity decoupling.

In the case of an ionic solute of charge, z_i , and radius, r_i , the ionic molar electrical conductivity, λ_i , is related to the solution viscosity through the Walden law (WaL):

$$\lambda_i \eta = \frac{z_i^2 e F}{6 \pi r_i}, \quad (10)$$

where F is the Faraday’s constant. This relationship can be obtained from the SER considering the Nernst–Einstein equation, which links the ionic diffusion coefficient with the ionic conductivity (valid at infinite dilution) [261]. Therefore, conductivity–viscosity decoupling is also expected in supercooled pure and mixed ionic melts or aqueous and non-aqueous salt solutions when the glass transition is approached [262, 263] which can be expressed by the fractional Walden law (FWaL):

$$\lambda_i \propto \left(\frac{1}{\eta} \right)^\beta \quad (11)$$

where β is the conductivity decoupling factor ($0 \leq \beta \leq 1$), which is the conductivity counterpart of the α diffusion decoupling factor.

Several models have been proposed to explain the breakdown of the SER or WaL, or mobility–viscosity decoupling, and most of them assume the existence

of dynamical spatial heterogeneities or mesoscopic domains with different mobility [264–272]. A review with a detailed description of these models that apply to glass forming liquids has been recently published [273].

10.1 Experimental transport properties of pure water

Supercooled water and aqueous solutions may exhibit a decoupling behavior different to that of classical liquids. Before discussing the transport properties of supercooled aqueous solutions, it is convenient to review briefly the information available on the transport properties of supercooled pure water.

Viscosity data for supercooled water that extends close to the homogeneous nucleation temperature (T_h) were reported by Hallet [274] and Osipov et al. [275] down to 249 K and 238 K, respectively. Dehaoui et al. [276] determined the viscosity of supercooled water down to 239 K by resorting to the measurement of the diffusion coefficients of polystyrene mesoparticles with radius $a = 175 \pm 3$ nm in the fluid, assuming that the SER holds for such big probes. These are the best available viscosity results for supercooled water that below 251 K are much lower than those reported by Osipov et al. [275].

The translational diffusion coefficient, D_T , of water in the supercooled regime has been measured by Price et al. [277] down to 238 K by using PGSE NMR. More recently, Xu et al. [224] extended the temperature range down to 126 K, deep into the no-man's land region, by heating a thin film of amorphous water with short IR laser pulses that converts the AWS into supercooled water, which in turns solidifies as crystalline ice at a rate that is measured by infrared reflection absorption spectroscopy (IRAS). Finally, the diffusion coefficient was calculated from the ice growth rate by using the Wilson–Frenkel model.

The rotational correlation time, τ_R , of liquid and supercooled water, at temperatures down to 236 K, was determined using ^{17}O and ^2H NMR spin relaxation of water-in-oil emulsions [278–280]. Qvist et al. [280] have noted that τ_R is an integral relaxation time, and the effect of librations can be removed by defining the rotational diffusion coefficient $D_R \equiv S_V^2/(6\tau_R)$, where S_V is the librational-order parameter obtained from MD simulations.

The three transport coefficients exhibit a super-Arrhenius behavior below ≈ 260 K, and they can be fitted using a power law [276, 277, 280]:

$$X(T) = X_0 \left(\frac{T}{T_S} - 1 \right)^{-\gamma} \quad (12)$$

where $X = \eta, \tau_R, D_T$, and $X_0 = \eta_0, \tau_{R0}, D_{T0}$, and $\gamma < 0$ for D_T . X_0, T_S and γ can be interpreted within the framework of idealized mode-coupling theory, this theory predicts a stretched exponential decay of the time correlation functions of translational diffusion. A better fit it was found with a bi-exponential func-

tion at all temperatures for rotational correlation functions. Moreover, T_S and γ values are rather different for η , τ_R , and D_T , a fact that cannot be explained by mode coupling theory, which predicts universal behavior. Qvist et al. [280] also discarded a mixture model of water with strongly bonded (slowly rotating) and weakly bonded (rapidly rotating) molecules to explain the bi-exponential time correlation functions. According to Tanaka, the origin of the super-Arrhenius behavior of τ_R would be thermally induced changes in the tetrahedral hydrogen-bond network, related to the possible existence of two types of hydrogen bonding, resembling a water two-state model scenario [101].

Hestand and Skinner [281] render an alternative analysis of the translational diffusion coefficients measured deep into the no-man's land using experimental and molecular dynamics simulation with the E3B3 water model. They propose that the high-temperature and low-temperature data obeying the Arrhenius law correspond to the diffusion of “pure” HDL (fragile liquid) and LDL (strong liquid), respectively, while the region between these two Arrhenius regimes indicates a continuum transition between the two liquid states of supercooled water. This transition has also been observed for the diffusion coefficient of supercritical TIP4P/2005 water when crossing the Widom line (WL) [96]. Similar conclusions were obtained by Tanaka and coworkers [282] using the TIP5P and ST2 water models in the framework of the two-state description of the supercooled water dynamics (see next subsection).

10.2 Diffusion–viscosity decoupling in pure water

Harris [283] found slight deviations to the SER at temperatures above 258 K, which can be accounted for using a decoupling factor $\alpha = 0.94$ using the FSER. In the range $235 \text{ K} < T < 258 \text{ K}$, the decoupling is more pronounced, and α decreases down to 0.67, being smaller than that observed for glass forming liquids close to T_g . Dehaoui et al. [276] reanalyzed the SER using the more reliable viscosity data and found $\alpha \approx 1$ at high temperature and $\alpha \approx 0.8$ at low temperature, in good agreement with the MD simulations using the ST2 model [284, 285] and the mW model [286].

Due to the lack of viscosity data below T_h , the possibility of testing the SER in the no-man's land region using the diffusion data by Xu et al. [224] is discarded in bulk water. There have been some attempts of testing the validity of the classical hydrodynamics model in deeply supercooled water (down to 200 K) confined in mesoporous silica (MCM-41-S), with pore diameters in the range 1.4–1.8 nm, by measuring the self-diffusion and the translational relaxation time using NMR and QENS spectroscopy, respectively [63]. A crossover from VFT to Arrhenius behavior was observed at 225 K for both quantities, while the ratio $D\tau/T$ remains almost constant down to 250 K and then increases steeply (up

to a factor 40 at 200 K) below the crossover temperature [63].

Whether the dynamical behavior of confined supercooled water is of relevance for supercooled bulk water is still an open question [287], mainly because the dynamical properties of confined supercooled water are sensitive to finite size effects, since the characteristic length of the dynamics cannot extend further than the typical pore size [287]. However, it is worthy to note that the decoupling factor of the FSER for confined water is $\alpha = 0.74$ in the fragile side that switches to $\alpha \approx 2/3$ in the strong side ($T < 225$ K), in good agreement with the dynamical facilitation predictions [271], considering that nanoconfined water in pores smaller than 2 nm behaves as a one-dimensional fluid. It should be noted that the use of the relaxation time as a proxy of the shear viscosity, as proposed by Xu et al. [224], has been criticized due to the evidence that the ratio τ/η depends of temperature [276, 288].

In the framework of the LLCP hypothesis, water dynamic anomalies are expected when the Widom line is approached, leading to the breakdown of the SER. Kumar et al. [289] analyzed this point by molecular dynamic calculations of the diffusion coefficient and the α -relaxation times between 0 and 200 MPa, using TIP5P and ST2 water models. It was observed that the product $D\tau_\alpha/T$ is constant for both models at high temperatures, but increases with decreasing temperature. Thus, the crossover to a more structured low-density liquid (LDL) when approaching the Widom line at $T_W(p)$ appears to be correlated with the breakdown of the SER and with the growth of dynamic heterogeneities.

In order to shed some light on the microscopic origin of the dynamic anomalies, Bagchi and coworkers [290] have performed molecular dynamics simulations with the TIP5P water model, focusing on the mechanism of inter-conversion between 5 and 4 hydrogen-bonded molecules, and the propagation of such events in bulk. The molecular trajectories at low temperatures show that large-amplitude rotational jumps propagate like strings, following the mechanism proposed by Laage and Hynes [131], with a characteristic propagation length that increases with decreasing temperature.

Using this model, the authors observed that the SER is valid at temperatures above 270 K, but large deviations occur at temperatures below 260 K where the diffusion-viscosity relation can be described with the FSER with decoupling factor $\alpha = 0.5$. The origin of the dynamical heterogeneities is attributed to the fact that water molecules visited by defects exhibit a rather large diffusivity, while those not visited are negligible.

An alternative microscopic view of the diffusion-viscosity decoupling is described by Tanaka and coworkers [282] using the two-state model. Figure 12a shows the product of the translational diffusion coefficient and the rotational relaxation time, which is equivalent to the ratio D_T/D_R , for the TIP5P model. In the fast-water dominant state ($T > T_{\text{mix}}^+$), translational motion couples to rotation, but the activation energy for reori-

entation becomes considerably higher than translation in the slow-water dominant state, so the reorientation will slow down much faster than the translation upon cooling, which leads to the breakdown of the Stokes-Einstein-Debye relation (SEDR),

$$D_T\tau_R = \frac{2a^2}{9}, \quad (13)$$

where a is the effective hydrodynamic radius. As observed in Fig. 12a, the fast-water dominant state follows the SEDR, and the decoupling behavior can be perfectly described by the prediction of the two-state model, indicating that the anomalous breakdown is a consequence of the slow-water dominant state upon cooling and not from glassiness.

The fact that rotation slows down much more than translation in deeply supercooled water is observed in real water, as shown in Fig. 12b, from the data for rotational diffusion [280].

10.3 Mobility-viscosity decoupling in aqueous solutions

The studies of decoupling in supercooled aqueous solutions are much more scarce than in pure supercooled water, in spite of the fact that aqueous solutions are much easily supercooled.

The conductivity-viscosity decoupling for ionic solutes in aqueous solutions is present even well above the glass transition temperature of the mixtures [291]. The first experimental report of conductivity-viscosity decoupling in supercooled aqueous solutions was reported by Moynihan et al. [292] for concentrated aqueous LiCl solutions ($0.12 < x_{\text{LiCl}} < 0.25$), which can be easily supercooled at moderate cooling rates. A crossover of the water diffusion dynamics was also observed by QENS for a supercooled LiCl solution ($x_{\text{LiCl}} = 0.12$) at ≈ 225 K, suggesting a breakdown of the SER occurring at the same temperature as in supercooled water [293]. Suzuki and Mishima [294] proposed that hydration water in supercooled LiCl solutions corresponds to HDL, which is the dominant phase of liquid water at pressures above the liquid-liquid transition line. Similar findings have been found also in studies regarding the phase diagram of water and NaCl [81, 82], and studies regarding the structure and dynamics of aqueous solutions of alkali halides [295, 296]. These results, along with experimental and MD simulation data on supercooled and NaCl aqueous solutions [297, 298], lead to the conclusion that the effect of the electric field near the ions will be equivalent to the pressure effect in promoting the HDL phase of water. This effect is also known as the electrostrictive effect of ions on water.

By studying the conductivity of NaCl in supercooled trehalose aqueous solutions, Miller et al. [299] found that $\alpha = 0.64$, that is, a decoupling stronger than that found for smaller polyols as glucose and glycerol. MD simulations for the diffusion of ions in trehalose-water mixtures indicate the presence of slower domains, con-

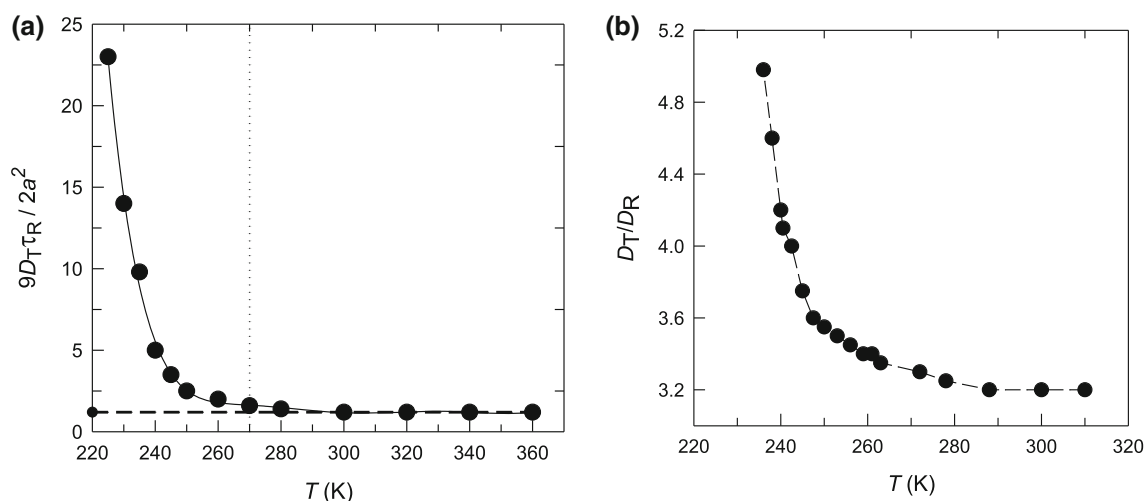


Fig. 12 **a** Breakdown of the Stokes–Einstein–Debye relation in TIP5P water model (points) and two-state model (continuous line) [282]. Dashed line represents the fast water contribution, see Ref. [282]. **b** Breakdown of the Stokes–Einstein–Debye relation in real water [280]

sisting mostly of trehalose, and faster domains that include the ions and their accompanying hydration shells [299].

A systematic study of the conductivity–viscosity decoupling for electrolytes with different ionic sizes (LiCl, NaCl, KCl, CsCl, $(C_4H_9)_4NBr$, $(C_4H_9)_4NI$, and fluorescein anion) in supercooled aqueous sucrose and trehalose solutions indicates that the magnitude of the deviations to the WaL (Eq. 10) increases, with decreasing ionic size [300,301]. It should be emphasized that the WaL is deduced considering only the viscous friction of ions in the solvent, even when the dielectric friction due to the electrostatic ion–dipole interactions is more important in the case of small ions [302].

Figure 13 shows the ratio D/D_{SE} for different solutes in supercooled aqueous trehalose and sucrose solutions, as a function of the reduced inverse temperature, T_g/T . Clearly, for ionic solutes the decoupling increases monotonically, following the behavior observed for the diffusion of water [303], and supporting the MD results showing that ions would move in water rich domains with low local viscosity [299].

Regarding the supercooled non-ionic aqueous solutions, those containing methanol and polyols such as glycerol, sucrose, and trehalose [303–305] are the most studied because of their application in the cryopreservation of biomolecules, tissues, and organs. The translational diffusion of ferrocenemethanol was measured in aqueous sucrose and trehalose solutions [305], and deviation to SER was observed at $T_g/T = 0.75$, as shown in Fig. 13. Thus, the breakdown of the SER for this non-ionic solute, as occur with the self-diffusion of trehalose and sucrose in aqueous solutions, exhibits a remarkable difference with that observed for ionic solutes.

The diffusion of water in a methanol aqueous solution ($x_{CH_3OH} = 0.22$) was studied using NMR by Malmace et al. [306]. A cross-over temperature at 223 K was detected where the diffusion is super-Arrhenius at higher temperature and Arrhenius at lower tempera-

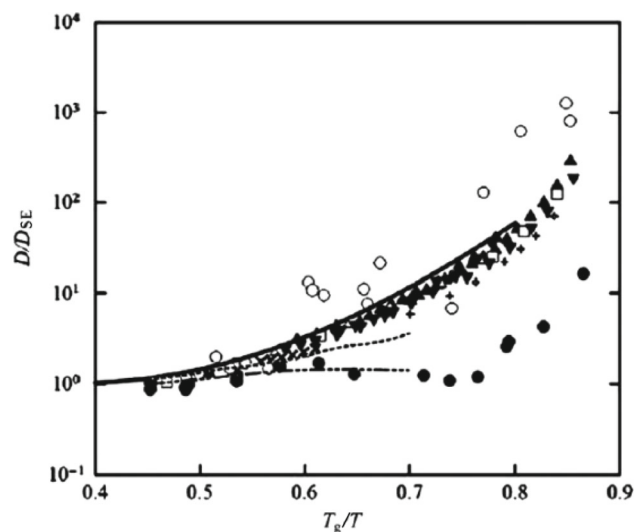


Fig. 13 Stokes–Einstein plot for the diffusion of: ferrocenemethanol (filled circles), NaCl (filled up-pointing triangles), KCl (empty up-pointing triangles), CsCl (filled down-pointing triangles), Bu_4NBr (bold pluses) in sucrose aqueous solutions; fluorescein disodium anion (empty circles), NaCl (empty squares), and Bu_4NI (bold times) in trehalose aqueous solutions. The diffusion of trehalose in trehalose aqueous solutions (long dash-dotted line), sucrose in aqueous solutions (dotted line), and water in these disaccharides aqueous solutions (continuous line) was taken from Ref. [303]. Reproduced from Ref. [273] with permission from the Royal Society of Chemistry

ture, suggesting a fragile-to-strong transition at that temperature. For the diffusion of glycerol in supercooled aqueous solutions determined by 1H NMR, Chen et al. [304] concluded that the decoupling reduced temperature (T/T_g) decreases with increasing water content in the glycerol mass fraction range $w = 0.85 - 1.0$. However, this apparent composition dependence of

the decoupling temperature was due to an erroneous extrapolation of the viscosity of the mixtures in the supercooled region, as shown by Corti and coworkers analyzing the diffusion of ferrocenemethanol in supercooled glycerol–water mixtures [307].

Decoupling of the rotational mobility in supercooled water was reported by Banerjee et al. [308], using electron spin resonance spectroscopy, and TEMPOL as a spin probe. The rotational mobility of the probe exhibits deviations from the SEDR, which increase sharply for $T < 225$ K. Two coexisting fractions of the probe were observed, having different mobility and fragility. The slower fraction is strong and predominates at low temperatures, below the fragile-to-strong dynamic crossover, while the fragile (non-Arrhenius) behavior predominates at high temperatures.

11 Do amorphous ices turn into deeply supercooled liquids before they crystallize?

As stated in “Introduction,” assuming a thermodynamic connection between amorphous water and the supercooled liquid [3], hyperquenched glassy water (HGW) [309,310] is the prime example that has the most straightforward connection to liquid water. Its preparation procedure involves liquid droplets, which immediately turn into a glassy, non-crystalline solid when splat-cooled through impact on a metal plate kept at cryoconditions ($T < 150$ K) [311]. Also for high-density amorphous ice (HDA) prepared by compression of HGW or through rapid cooling of the pressurized liquid, the direct relation between the liquid and amorphous solid is evident [312,313]. By contrast, other routes of preparation do not immediately suggest a relation between the amorphous solid and the liquid. For instance, liquid water is not encountered when preparing amorphous ices from cubic or hexagonal ice through high-energy irradiation [314–316] or pressure-induced amorphization [7,317]. This statement applies in particular to unrelaxed HDA (uHDA) [7] and to amorphous ices accessed through solid–solid transformations via uHDA, such as low-density (LDA) [8] and very-high-density amorphous ice (VHDA) [318]. Also when preparing amorphous solid water (ASW), liquid water is not involved—ASW is formed by water vapor deposition on a cryogenic metal plate [319].

While it is natural to assume that HGW and HDA (produced from liquid water or HGW) revert back to liquid water upon reheating, this is not so straightforward for ASW, LDA, HDA (produced from crystalline ice), or VHDA. For HGW, the transition from the glassy solid back to the ultraviscous liquid has been observed at 136 K [320,321], supporting the thermodynamic connection between HGW and liquid water. This connection has been inferred on the basis of the calorimetric glass-to-liquid transition, *i.e.*, a step-like increase in heat capacity indicating the unfreezing of relaxational degrees of freedom. The calorimetric traces

for HGW and all other amorphous ices mentioned above are summarized in Figure 9 of the 2016 colloquium by Amann-Winkel et al. [13]. Most notably, the traces for HGW, ASW, and LDA are all highly similar, indicating a glass transition onset, *i.e.*, T_g of 136 K. This striking similarity, together with their undistinguishable molecular structures [322], has led to the suggestion that also ASW and LDA turn into the same ultraviscous liquid as HGW does above 136 K [323,324]. In any case, upon heating through the glass-to-liquid transition the transformation from the immobile, non-ergodic state to the mobile, ergodic state needs to take place. The glass-to-liquid transition is repeatable when performing cooling and heating cycles [320,321], *i.e.*, this allows one to switch back and forth between the mobile, viscous liquid and the immobile, rigid solid.

The calorimetric trace for HDA is even more interesting: It indicates a glass-to-liquid transition with an onset of 116 K [325], *i.e.*, 20 K lower than the T_g of LDA/ASW/HGW. Furthermore, the increase in heat capacity at T_g is roughly four times higher for HDA than for HGW/LDA/ASW [325]. If there is indeed a thermodynamic connection of the amorphous ices with liquid water, the finding of two distinct glass transitions strongly suggests the existence of two distinct types of liquid water differing by about 25% in density: high-density liquid (HDL) and low-density liquid water (LDL) [325]. In other words, two distinct liquids may exist metastably in the temperature range between 116 and 150 K, *i.e.*, in the stability domain of crystalline ice. If valid, such a scenario would then be direct support for two-liquid theories aiming at explaining the anomalous properties of supercooled liquid water, such as the liquid–liquid phase transition hypothesis [16]. The suggestion of the existence of two distinct glass transitions associated with two distinct liquids is strengthened when inspecting them in more detail: T_g (HDA) increases with pressure (up to 0.8 GPa), whereas T_g (LDA) decreases, as assessed both in terms of simulation [326] and experimental work [327,328]. The latter is based on observations of the volumetric glass transition [327] and a kinetic analysis of volumetric changes [328] of samples kept isobarically at high pressure.

However, the possible connection between amorphous ices and liquid water has also been contested. Many of the arguments denying such a connection are summarized by Loerting, Brazhkin, and Morishita in chapter III.E of ref. [329] and by Amann-Winkel et al. in ref. [13]. In essence, the key arguments suppose that amorphous ices may entirely or in parts be composed of distorted nanocrystals [330], show crystal-like phonons [331,332] and/or that there is no diffusive, translational motion of water molecules [333]. The latter would imply that the calorimetric step would not reflect a glass-to-liquid transformation, but one above which only orientational motions are unlocked. Recent work has indicated diffusive processes above both glass transition temperatures [334,335]. Furthermore, crystal-like point defect dynamics could be excluded on the basis of doping and isotope substitution experiments [336]. In spite

of these findings, the question whether or not above their glass transition temperatures amorphous ices turn into ultraviscous liquids is still disputed [337]. This question is afflicted with added complexity since, not far above their T_g s, all amorphous ices/ultraviscous liquids experience irreversible phase transformations. LDA/LDL at ambient and low pressure shows crystallization to cubic ice (ice I_c), HDA/HDL at ambient pressure experiences a first-order like polyamorphic transition to LDA/LDL and at elevated pressures HDA/HDL crystallizes to high-pressure ices such as ices VI, IX, or XII [338–341]. In the pressure range up to 1.6 GPa, the two T_g s are found between 110 and 160 K [342], and the crystallization temperature T_x varies from 140 to 185 K [339]. At ambient pressure, HDA experiences the onset to the polyamorphic transition to LDA at $T_{poly} = 132$ K or lower [343]. This leaves us with a window of about 16 K between T_g and T_{poly} , in which the ultraviscous HDL phase can be studied at ambient pressure. Also, under high-pressure conditions the window for the study of HDL is narrow, if it exists at all [340]. T_x for LDA depends on how meticulously ice seeds have been avoided in the preparation: For samples significantly contaminated with ice I, T_x is 135 K or below, but T_x can be up to 150 K for fully amorphous samples [344]. At 140 K, a difference in nucleation/crystal growth rates of 18 (!) orders of magnitude [135] can be seen between the thin ASW films prepared by Jenniskens and Blake [345] and the HGW samples prepared by Hage et al. [346]. This leaves a window of no more than 14 K between T_g and T_x for the study of ultraviscous LDL at ambient pressure for the HGW samples, but entirely closes the window for thin ASW films.

Taken together, the non-crystalline states show a very rich behavior in the window just above T_g involving competition between relaxations toward metastable equilibrium and transformations to more stable phases, which by themselves may be either metastable as well (such as ice I_c , ice XII or LDA/LDL) or thermodynamically stable (such as ice VI). For this very reason, it is highly important to study the tiny window between T_g and T_x in detail—a research area that has largely been neglected in the literature, with only a handful of pertinent studies. In fact, this window may hold the key to solve important pieces of the riddle concerning water’s anomalous nature. For instance, based on decompression experiments, Winkel et al. suggest that “the sudden macroscopic phase separation at 0.07 GPa and 140 K represents the observation of a first-order transition between an ultraviscous high-density bulk liquid (HDL) and an ultraviscous low-density bulk liquid (LDL)” [347]—making the case for a first-order liquid–liquid phase transition at the origin of water’s anomalous properties such as the density maximum, heat capacity minimum, and isothermal compressibility minimum [6].

A crucial, still largely lacking experiment that would be needed to make a compelling case for liquid phases in this window is (i) the repeatability when observing the glass transition in subsequent heating scans and

(ii) its reversibility in cooling scans. Both items are hard to test in experiments on amorphous ices just because the window is so narrow before crystallization interferes. There are some notable exceptions in this regard: Seidl et al. have shown repeatability of the volumetric glass transition in up to six subsequent heating scans [327], and Mayer and co-workers have also investigated the repeatability of the calorimetric glass transition [324, 348, 349]. This situation represents an experimental challenge and leads us to raise the following key questions: “For how long can the ultraviscous liquids be kept above T_g before they crystallize? Is it long enough to fully equilibrate the liquid and develop ergodicity before crystallization interferes?”. An affirmative answer to the latter question necessitates that activation barriers against crystallization are sufficiently high, *i.e.*, thermal fluctuations at 110–160 K rather promote the formation of ultraviscous liquids than crystallites.

Unfortunately, amorphous ice research has so far paid barely any attention to compare structural relaxation times with crystallization times. One of the studies addressing this question directly is the dielectric relaxation work by Lemke et al. [350]. In this work, the structural relaxation times are extracted through frequency-dependent dielectric loss measurements as a function of temperature. The crystallization times of LDA (as well as the polyamorphic transformation times of HDA) were determined through time-evolution experiments at several temperatures above and near T_g by monitoring the dielectric loss at specific frequencies. Some of the experimental results collected in [350] are summarized in Fig. 14. The dielectric relaxation times decrease with increasing temperature and reach 100 s at about 110 K for HDA (blue triangles) and 125 K for LDA (red diamonds). This defines the dielectric glass transition temperatures, which are somewhat lower than the calorimetric ones because of the much lower heating rates involved in the dielectric experiments (1 K/h *vs.* 10 K/min). The polyamorphic transformation HDA→LDA is observed near 125 K and the crystallization LDA→ice I_c near 150 K. This results in a window of about 15 K and 25 K for the study of HDL and LDL, respectively. Within this window, the dielectric relaxation times drop to slightly below 1 s. At the same time, the polyamorphic transformation times drop from about 10^6 to 10^4 s in this window (blue circles for HDL→LDL), and also, the crystallization times of LDL are $> 10^4$ s up to 145 K (red squares). The ratio between polyamorphic transformation times and HDL relaxation times is $> 10^4$ at 125 K (green circles), *i.e.*, 15 K above T_g (HDL). In other words, more than 10,000 dielectric relaxation times are available for equilibration prior to the 25% density change associated with the polyamorphic transition. Similarly, the ratio between crystallization and LDL relaxation times is $> 10^4$ at 145 K (green squares), 20 K above T_g (LDL). Again, also for equilibration of LDL there are ample dielectric relaxation times available in the window above its T_g .

The situation is similar for HDL also at ambient and high-pressure conditions, where it is of utmost impor-

tance to properly anneal the HDA samples to increase their thermal stability. This finding has been brought to the attention of the community first by Nelmes et al. [351] and Winkel et al. [347]: A proper annealing procedure shifts the polyamorphic transition up by 20 K at ambient pressure, a prerequisite that is required to allow for the observation of the HDA glass transition [325]. Also the crystallization temperatures T_x at high pressure are shifted upward significantly by annealing of HDA, extending the window in which HDL can be studied and thus shrinking the no-man's land, in which only crystalline ices can be observed [352]. Stern et al. have demonstrated that high annealing temperatures and pressures are beneficial in this respect, allowing for the preparation of the thermally most stable amorphous ices HDA and VHDA [338–340,352]. The microscopic picture behind these findings involves the complete amorphization and elimination of nanocrystalline remnants of ice I that act as crystallization seeds through high-pressure annealing [352–354]. Samples obtained after proper annealing have been employed for neutron scattering [355] and ^2H -NMR measurements [356,357] addressing the relaxation dynamics in HDA. The relaxation times and thermal stabilities found in these experiments agree well with the data in Fig. 14. Stern, Seidl-Nigsch, and Loerting have demonstrated that in the pressure range up to 0.3 GPa, the state accessed in the narrow window above T_g is independent of preparation history. As a consequence T_x , no longer depends on the thermodynamic path—as expected for a liquid after equilibration [340]. Also, the X-ray diffractograms and calorimetry scans of HDA that are recorded after annealing this amorphous ice at 0.2 GPa are barely any different, no matter whether VHDA or uHDA is used as starting point in the thermodynamic path to prepare it [347]. An analysis in terms of timescale ratios similar to the one in Fig. 14 for annealed HDA at high-pressure conditions is still missing in the literature. Crystallization rates under pressure have been estimated for annealed HDA by Stern et al. at 0.1–1.9 GPa [340] and for unannealed HDA by Handle et al. at 0.1–1.1 GPa [328,343,358]. A direct comparison between relaxation times and crystallization times has so far only been made for uHDA at 0.1 GPa and 0.2 GPa at 125 K, 130 K and 135 K [343]. These results show that the ratio of crystallization and structural relaxation times is very close to 1 for uHDA. As compared to uHDA, annealed HDA shows orders of magnitude lower crystallization rates, which implies that above T_g the timescale ratio will be somewhere between 10^3 and 10^6 at 0.1–0.2 GPa. Albeit not measured systematically and quantitatively, this appears to be quite similar to the situation depicted in Fig. 14, *i.e.*, HDL has thousands of relaxation times at its disposal before it crystallizes at 0.1–0.2 GPa.

At higher pressures, the situation is different: T_x becomes path-dependent [340]. This is because T_x (HDA) increases less with pressure than T_g (HDA), *i.e.*, the window in which ultraviscous water may be observed closes at 0.3 GPa, with $T_g > T_x$ between 0.3 and 0.8 GPa. In this pressure range, the amorphous solid

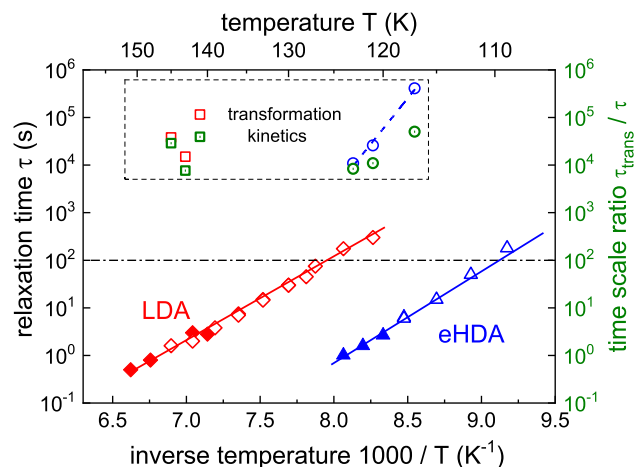


Fig. 14 Arrhenius plot of timescales τ_{trans} that are required for the crystallization of LDA (red squares at 140–150 K in dashed box) and for the polyamorphic HDA→LDA transformation (blue circles at 115–125 K in dashed box) together with timescales of dielectric relaxation τ for LDA/LDL (red diamonds) and HDA/HDL (blue triangles). Filled symbols correspond to time constants obtained directly from the position of the susceptibility maxima; open symbols are obtained via frequency–temperature superposition, see also Refs. [325,350,359] for spectral data and more details. The ratio of timescales τ_{trans}/τ is given as green symbols for HDA (squares with centre dot) and for LDA (circles with centre dot). All measurements were done at ambient pressure. Figure adapted from Ref. [350]

experiences a solid–solid transformation to ice polymorphs. Above 0.8 GPa, there is a dynamics anomaly, where T_g suddenly drops from 165 K for HDA to 120 K for VHDA [328]. The observation of path dependence for T_x of VHDA, the most stable amorphous ice form above 0.8 GPa, implies that it never turns into a liquid upon heating. That is, while the glass transition for HDA could be a glass-to-liquid transition, the glass transition for VHDA is probably a glass-to-glass transition. The very large window between T_g and T_x of about 50–70 K for VHDA at 0.8–1.9 GPa is not occupied by an ultraviscous liquid, but presumably by an amorphous ice that only shows rotational degrees of freedom [340]. This conjecture supersedes the earlier suggestion by Handle and Loerting that VHDA may also turn into a liquid above 0.8 GPa [328]. The dynamic anomaly discovered in Ref. [328] can then be interpreted as a crossover from translational motion to rotational motion of H_2O molecules above T_g . In other words, while there are three distinct amorphous ices, here we suggest that there are only two distinct supercooled liquids, which can be observed and studied at pressures up to 0.3 GPa. That is, the sudden transition from high- to low-density amorphous ice upon decompression at 0.07 GPa and 140 K which involves the propagation of a sharp interface between the two [347] can indeed be understood as the first experimental observation of a first-order liquid–liquid transition in bulk water. It still remains open how this transition develops at higher

temperatures and whether or not a liquid–liquid critical point is involved. This question cannot be answered in bulk water experiments on timescales between seconds and days, but requires experiments (and simulations) on the nano- or microsecond, where both the heating process and the probing of the sample take place in this ultrafast manner. Yet, at the same time the technique needs to be slow enough to ensure thermal equilibration of the sample [3].

Here, the most promising study up to now is the work by Kim et al. [26]. In essence, they used a femtosecond laser for ultrafast heating of HDA immediately followed by x-ray laser pulses to probe radial density functions. They found evidence for a transition at 200 K, which is separated from crystallization. This could be indicative of a crossing of the Widom line or a liquid–liquid transition.

12 Simulations of amorphous ice

Simulation studies on water were reviewed in detail by Loerting and Giovambattista in 2006 [360] and Giovambattista et al. in 2013 [361].

There is continuing interest to understand the behavior of amorphous ice in the context of the potential energy landscape (PEL) [125]. The PEL is a high-dimensional surface describing the potential energy of the system as a function of the coordinates of its N constituent molecules. Despite its complexity, the properties of the PEL have been used successfully to elucidate the nature of many glass-forming liquids, including water; see Ref. [222] for a recent example.

In simulations of amorphous ice, the system explores a wide range of the PEL as it transforms from LDA ice to HDA ice and back again. Giovambattista and coworkers have recently focused on the case of ST2 water, in which the LLPT of the equilibrium liquid is well characterized [362], and in which the glass is known to undergo a dramatic LDA-to-HDA transition upon compression. In Ref. [363], distinct “megabasins” in the PEL are found for LDA and HDA ice, and the transformations between the amorphous ices are shown to display all the thermodynamic features of a first-order transition between out-of-equilibrium phases corresponding to these two megabasins. Similar results were found using TIP4P/2005 [364]. Reference [365] extends the PEL approach by considering many different samples of both LDA and HDA ice prepared by widely different means. As expected for a glass, differences in preparation history significantly influence the form of the LDA–HDA transformation. However, Ref. [365] shows that these differences are clearly correlated with the initial depth of the sample in its PEL megabasin. Finally, Ref. [366] shows that the usual thermodynamic state variables (e.g., N , V , and T) can be augmented by a small number of additional quantities calculated from the PEL to produce a set of variables sufficient for predicting how a given sample of glassy water will respond, e.g., to compression or heat-

ing, regardless of how that sample was prepared. That is, at least in the case of ST2 water, the glass can be successfully described by state variables, just like in an equilibrium system. In sum, these works show that despite the complexity of behavior observed for the amorphous ices, this complexity can be rationalized in quasi-thermodynamic terms, suggesting that the out-of-equilibrium glass is strongly influenced by the same physics that is responsible for the occurrence of a LLPT in the equilibrium free energy surface.

Of course, one must be careful when comparing results from simulations and experiments on glasses, because the timescales on which glasses are prepared in simulations are normally many orders of magnitude shorter than in experiments. Nonetheless, results such as those in Ref. [365] show that even instantaneously quenched simulated glasses exhibit the qualitative features of the LDA–HDA transformation, suggesting that some of the behavior of the amorphous ices is insensitive to the quench rate.

13 Polyamorphism, liquid–liquid transition, and nano-segregation in salty aqueous solutions

In salt solutions, no-man’s land impenetrability can be circumvented and thermodynamical structural properties of deeply supercooled water can be studied for temperatures and pressures that are not accessible for pure water due to ice nucleation. This “trick” has, however, its own drawbacks.

At one extreme, very high salt concentration, most of the water molecules belong to the ion’s hydration shell, and this results in the partial destruction of the topological elements found in bulk water [367–372]: the solute presence hinders the formation of the open tetrahedral network of hydrogen bonds, and prevents ice formation and growth, at least on a macroscopic scale. As a consequence, for most ionic solutes there exist definite proportions between water molecules and salt content (R = moles of water/moles of salt), close to the eutectic composition, for which the solution behaves as a good glass former, but it does no more retain water anomalies [373,374]. The structure of water in the vitrified solid solutions has been shown to be similar to that of the high density ice amorphous phases (eHDA, uHDA) [370–372], as the electrostrictive effect of the salt is roughly similar to that of an applied external pressure [295,375].

At the other extreme, salt solvation at dilute concentrations does not dramatically disturb water properties, but as dilution is increased the system behaves as a bad glass former, like water, and by entering the no-man’s land the system desalts and freezes into cubic ice, unless hyper-fast cooling ($> 10^6$ K/s) is employed to force the system to freeze in a low-density amorphous state (LDA) [376–378]. Hyperquenched dilute solutions have indeed been shown to be structurally very simi-

lar to pure LDA [376]. However, Suzuki and Mishima suggested the presence of pure LDA domains and a distorted, high-density-like water network in the vicinity of the ions [78]. In any case, the problem of the existence on an inaccessible region of the phase diagram is not solved, even if it is observed that the ice nucleation rate is much slower in these solutions [376–378].

In the last ten years, several structural and dynamical studies on $\text{LiCl}\cdot\text{RH}_2\text{O}$, $\text{LiBr}\cdot\text{RH}_2\text{O}$, and $\text{NaCl}\cdot\text{RH}_2\text{O}$ solutions were performed, employing X-ray diffraction, neutron diffraction with isotopic substitution and small angle scattering under high pressure, transient grating light scattering, and using different methods of amorphization, including hyperquenching [376], and pressure-induced amorphization [370, 371, 377, 378], to force the solutions in an amorphous, either LDA or HDA, state.

The main conclusions derived are resumed in Fig. 15.

At very high dilutions ($R = 40$), LiCl aqueous solutions show the same trends as pure water upon lowering the temperature, but the radial distribution functions of the water molecules are, as observed for other salt solutions, distorted with respect to those of the neat solvent. In the liquid at ambient conditions, ions solvation induces a shrinkage of the second neighbor's shell with consequent loss of tetrahedrality. The hyperquenched glassy phase (HGW) can be associated with the pure LDA state of water, despite the presence of salt, instead. Indeed, on lowering the temperature through the supercooled phase to the HGW one, the H bonds recover linearity and the network tetrahedrality increases. The structure of the salty HGW is thus similar to that of pure HGW, although all the peaks of the radial distribution functions are broader, suggesting that the distortions induced by the salt on the structure of water persist in this state and determine a variety of different local configurations within the H-bond network [376]. Moreover, the number of neighboring water molecules decreases upon cooling as in the HGW phase, thus confirming that this amorphous form of the solution can be associated with the LDA polymorph of water. Changes of the hydration shell of the ions are little [376], and there is also little or no evidence for phase separation in the hyperquenched glass of this work. Indeed, the number of direct or water separated ion contacts does not show a statistically relevant increase in the HGW phase.

The study of LiCl (Br) RH_2O and NaCl RH_2O solutions in a broad concentration range ($3 < R < 20$) shows that two regimes can be clearly distinguished with a rather sharp change close to the eutectic concentration, $R = 6$ and $R = 10.5$, respectively [371, 376–379]. Eutectic solutions are good glass formers and produce homogeneous samples at standard cooling rates (10 K/s) with an average microscopic structure resembling that of pure, equilibrated eHDA. The glass is stable upon temperature annealing at ambient pressure, and no crystallization is observed when crossing the glass transition temperature (Fig. 15). When annealed under high pressure, the salty eHDA sample transforms to a higher density phase, named salty VHDA, which

mimics the equivalent observation in pure water. The transition has been ascribed to a change in local coordination around the Li ion. This transition has been shown to be reversible, and coexistence of the two states has been observed when annealing the recovered salty VHDA state at ambient pressure. However, neutron diffraction and small-angle neutron scattering experiments show that the corresponding undercooled liquid shows no hints of such transition [372].

For $6 < R < 8$, glass-forming LiCl and LiBr solutions produce nanophase segregation between a most likely pure water phase and an undercooled liquid with $R \approx 6$, the characteristic dimensions of the phase segregation being of about 3 nm [372, 380–382]. These water clusters are small enough to avoid crystallization of ice under further cooling, but LDA patches are formed and embedded into a mother glassy salt solution. When annealed at ambient pressure these nano-segregated patches of LDA transform into cubic ice at about 150 K (Fig. 15), while the glassy matrix undergoes a glass-to-liquid transition (at about 140 K) and subsequently recrystallizes into ice I_h and the LiCl hydrates at about 180 K.

For $R > 8$, LiCl solutions can be amorphized in a homogeneous sample only by fast quenching techniques. However, under annealing at ambient pressure, the samples quickly separate (at about 150 K) into pure ice and some LiCl hydrate (Fig. 15). If standard quenching rates are used the sample segregates, upon cooling, into a glassy concentrated LiCl solution of $R = 6$ and a water rich phase, freezing to hexagonal ice. These samples experience pressure-induced amorphization to HDA at $P > 1$ GPa. The densification of the sample under pressure is mainly due to the I_h to HDA transition.

However, pressure-induced amorphization in these samples can be used to force the sample in a HDA state in the presence of salt and opens the perspective of studying the HDA to LDA transition upon increasing the dilution.

We refer the interested reader to Ref. [383] for further prospects of the topic as well as an even more detailed review of the existing studies in both experiments and simulations.

14 Glassy dynamics at grain boundaries in ice

The study of mechanical deformation processes at grain boundaries (GB) in ice is very important, as stated in “Introduction,” and computer simulations offer a privileged point of view as far as structural changes occurring during pre-melting are observed [384].

Recently, the pre-melting phenomena in pristine coincident-site-lattice GBs in ice I_h were investigated for temperatures just below the melting point [385]. In particular, two boundaries relevant in ice, namely the $\Sigma 35$ and $\Sigma 14$ symmetric tilt GBs, which have

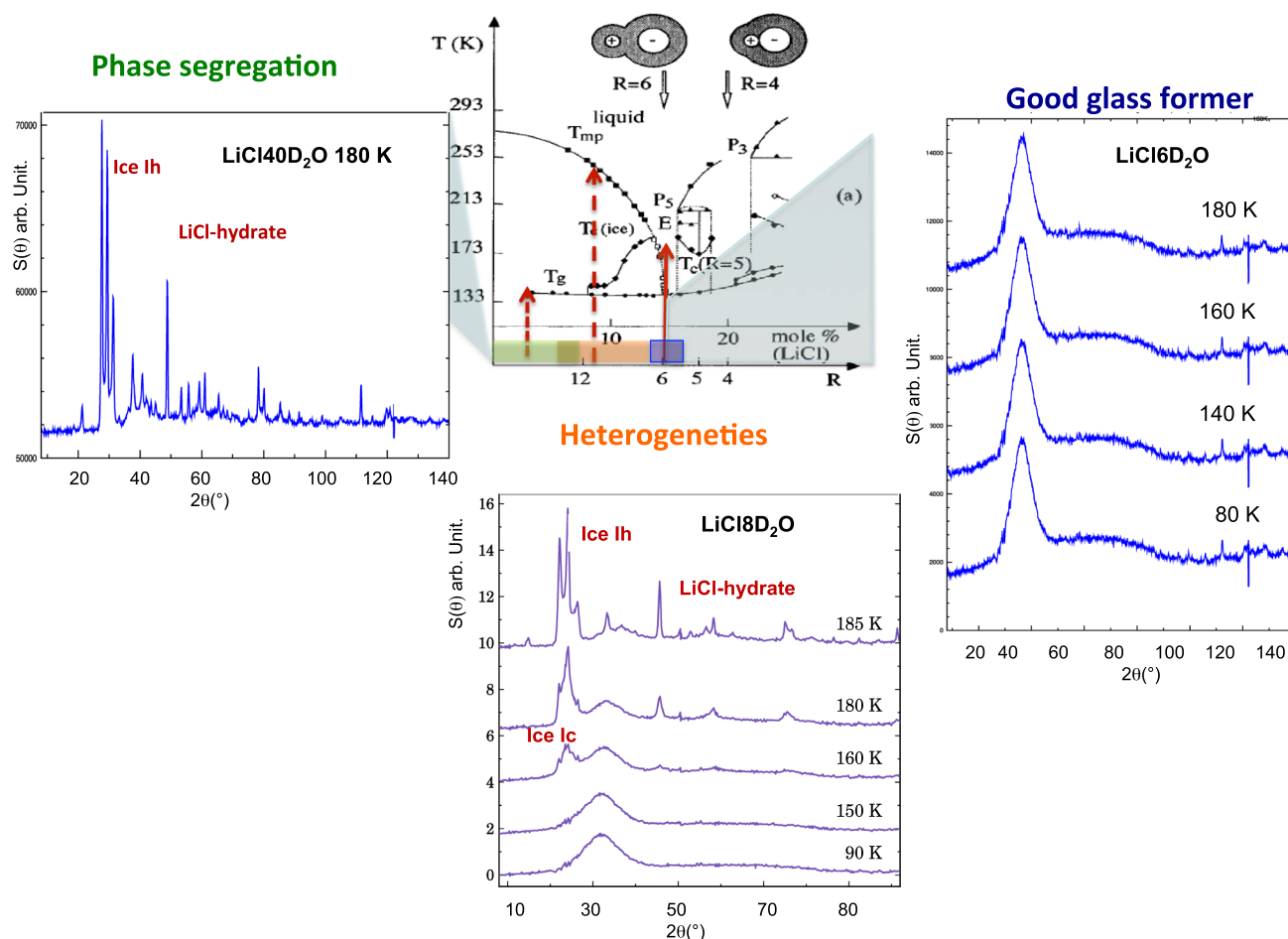


Fig. 15 Summary of the structural transformations undergone by LiCl-RD₂O solutions by annealing the three representative $R = 40$, $R = 8$ and $R = 6$ amorphized samples (by hyperquenching techniques at $R = 40$, fast cooling (10^2 K/s) for $R = 8$, or simple cooling at $R = 6$)

been observed experimentally [386–389], were studied. Density-functional-theory (DFT)-based *ab initio* molecular dynamics (AIMD) simulations were performed on a 156-molecule cell based on the PBE functional [390]. Figure 16 depicts the relaxed initial configuration, the final configuration after 100ps, and individual displacement magnitude as a function of time for a water molecule that belongs to the bulk region (black), and another that is part of the GB region (blue). As expected, the displacements are very small in the bulk region, featuring only vibrational motion. For the molecules in the GB, however, the displacements are substantially larger. Moreover, these displacements are not homogeneous, in that some molecules move substantially while others do not, and they are not smooth functions of time, but instead discrete sequences of fast jumps separated by relatively long-lived noisy plateaus. These two properties are hallmark signatures of glassy dynamics.

Since AIMD simulations are very limited in terms of size and simulation time, classical molecular dynamics (MD) simulations were also performed on a 10800-molecule cell based on the TIP4P/Ice model [391] at a temperature 5 K below the model's melting tempera-

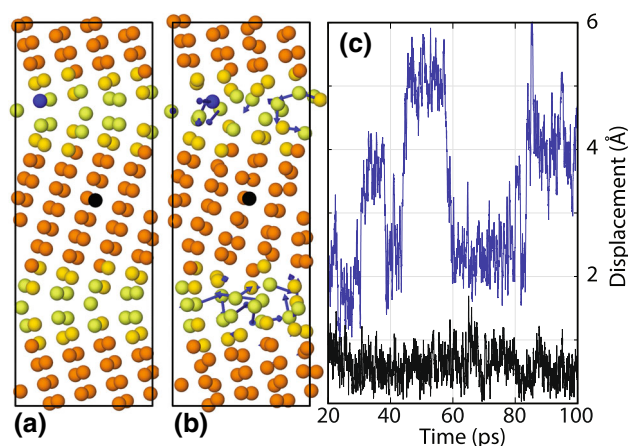


Fig. 16 AIMD snapshots of oxygen positions in the $\Sigma 35$ symmetric tilt boundary for the **a** initial, and **b** final states, with the blue arrows indicating the displacement magnitude relative to the initial state. **c** The displacement as a function of time for oxygen marked blue and black in **a** and **b**. Reproduced from Ref. [385] with permission from the PCCP Owner Societies

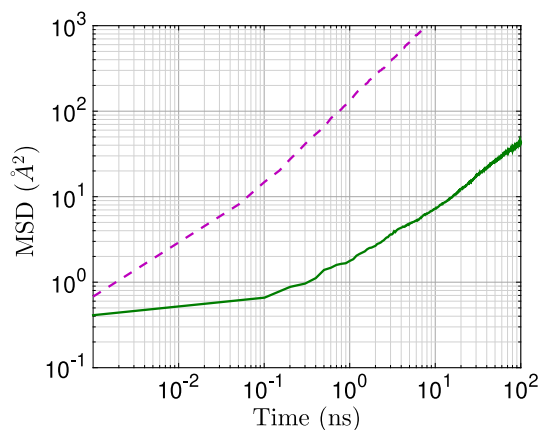


Fig. 17 MSD as a function of time of the GB molecules (green) for the $\Sigma 35$ case and for the bulk supercooled TIP4P/Ice liquid at the same temperature (purple). Reproduced from Ref. [385] with permission from the PCCP Owner Societies

ture. By looking at individual trajectories, the nature of the molecular mobility is very similar compared to the AIMD results, displaying jump-like, heterogeneous displacements in the GB region. Figure 17 shows the mean square displacement (MSD) of water molecules at the GB region compared to the bulk supercooled liquid at the same temperature. The GB translational diffusion is found to be subdiffusive, i.e., of the form $\sim t^\gamma$, [392,393] on the timescales of ~ 10 ns up to at least $0.1 \mu\text{s}$ with an exponent $\gamma = 0.75 \pm 0.01$ for the $\Sigma 35$ case. The bulk supercooled liquid at the same temperature, on the other hand, diffuses normally on these time scales, suggesting that the anomalous diffusion is an effect due to the confinement of the pre-melt layer by the surrounding crystalline grains.

The jump-like motion of the type shown in Fig. 16 can be modeled in terms of the continuous-time random-walk framework which are characterized by waiting-time (WTD) and jump-length (JLD) distributions and can model anomalous diffusion processes [392–396]. Using the results from the classical MD simulations, the walkers were identified with the positions of the oxygen atoms in the MD simulations and the corresponding WTD and JLD was determined. Figure 18 displays the resulting WTD and JLD. Whereas the latter decays exponentially with large L , the former decays according to a power law for long waiting times τ . Specifically, the asymptotic behavior of the WTD for the $\Sigma 35$ GB is $\phi(\tau) \sim \tau^{-1-\gamma}$ which gives rise to a $\text{MSD} \sim t^\gamma$ [392]. The continuous-time random-walk analysis gives an exponent $\gamma = 0.81 \pm 0.01$ for $\Sigma 35$, which agrees well with the direct MD MSD results. This implies that the observed subdiffusive behavior is a result of intermittent molecular motion seen in both AIMD and MD simulations. The heavy-tailed character of the WTDs is very similar to that observed for the dynamics for both fragile and strong glass formers [397,398], indicating the similarity

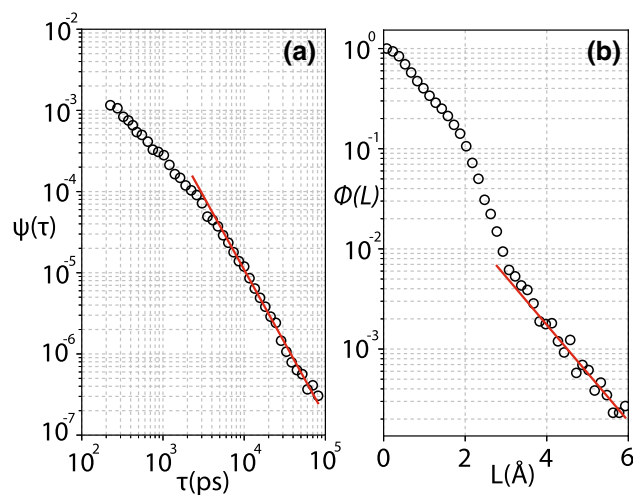


Fig. 18 (a) WTD as a function of the waiting time τ and (b) JLD as a function of the jump length L , for the GB molecules in the $\Sigma 35$ case. Reproduced from Ref. [385] with permission from the PCCP Owner Societies

between the molecular motion in GBs in ice and that seen in glassy systems.

15 Conclusions and Perspectives

Here, we reviewed recent progress in the field of supercooled water. In recent years, advances in experimental and computational techniques and apparatus have permitted the unraveling of many characteristics of this fascinating and important liquid. In the meantime, a picture of a liquid emerges with many important features yet to be understood or discovered.

Regarding the possible extension of the work with the V_4 index, one possibility would be to apply it to glassy relaxation events in the supercooled state. We note that, differently from other order parameters, this index finds that the D, distorted molecules or defects, are in strong minority within this regime [399] and, thus, their fraction is similar to the fraction of mobile molecules. Another interesting possibility for this indicator stems from its energetic rather than structural origin, since in principle it could be applied to non-bulk or nanoconfined environments if properly adapted.

Studies of supercooled nanodroplets present both challenges and opportunities. Precise experimental control and measurement of the size of such droplets remain difficult, but progress in this area will provide a way to study water samples that are supercooled, under pressure, and resistant to crystallization. These are all key ingredients for accessing the conditions of the LLPT. Water nanodroplets containing solute molecules are also of interest, since the physics of the LLPT may influence the location of the solute in the droplet, as recently shown in the simulation study of Ref. [400]. This result suggests that the location of a solute within the nanodroplet could be used as a probe to infer infor-

mation about the density profile of the droplet and, for example, reveal the conditions where a LDL-like region appears in the core of the droplet as T decreases.

We discussed the relevance of many-body HB interactions and their cooperativity in water. We briefly reviewed different approaches to include the cooperativity effects in water models, and we discussed how tunable cooperative parameters give insight into the relation among the different scenarios for supercooled water. In particular, the FS Hamiltonian model recovers all the scenarios by increasing the cooperativity, from zero for the SF scenario, to finite for the LLCP hypothesis, to large for the CPF and the SLC scenarios. However, many open questions remain in this respect. For example, it is still not clear whether the charge transfer or the polarization is the leading source of HB cooperativity [169, 401], how the HB cooperativity changes with the local geometry [402, 403], near interfaces [404], or in ionic aqueous solutions [405]. Also, experimentally it is unsettled how to quantify the HB cooperativity in bulk water, extending the techniques adopted for small water clusters, e.g., infrared spectroscopic study [152, 157].

This uncertainty has as a consequence a variety of approaches to model water and its cooperativity, often with a tradeoff between accuracy and computational cost. They differ about, e. g., the order up to which many-body interactions are included, or how these interactions change with T and P . Quantum *ab initio* calculations debate these questions, but are limited, mainly, in water clusters size [162, 401, 406].

As a consequence, the quest for a water model that could include proper many-body interactions in an effective way for large-scale simulations is still open. For example, common coarse-grained models for biological simulations have been developed in the attempt to include at least some effects related to water, e.g., in MARTINI [407] or SIRAH [408] force fields. However, the adopted coarse graining scale, at four water molecules, does not allow them to include the cooperativity of the HBs, leaving unanswered the question of how can we account for them in biological modeling. An alternative approach, based on the FS water model, has been applied with interesting results to several large-scale studies with biological motivation [74, 248–251, 253–256, 409].

In the supercooled regime structure, thermodynamics and dynamics are closely connected in ways that can help us to understand the influence that water exerts on other compounds when it is in solution or confined [1]. Close to the LLCP water shows a fragile-to-strong crossover that it is connected to the Widom line. The presence of this crossover can help to signal the presence of a LLCP also in confinement or in solutions [46, 47, 57, 81, 410]. In this respect, of particular importance is water in biosolutions, where the change of status from a HDL to a LDL upon cooling can exert a strong influence on biological functions [71, 411]. For example, the switch to activated processes, and therefore a major change in relaxation mechanisms connected to a change in the structure, can influence the distribution of solutes close to large biomolecules.

We discussed the dynamic crossovers in HB relaxation as a function of P in hydration water. QENS experiments on hydrated proteins [184] verify the predictions of the FS model about the P -dependence of isochronism, activation energy, and crossover temperature of the HB correlation at the crossover, but are unable to discriminate between the LLCP and SF scenarios. Indeed, the FS model predicts that the fragility index at the crossover should increase with increasing P for the LLCP, or remain constant for the SF scenario. Hence, reducing the error bars of such experiments could finally help us in solving the puzzle of which scenario is valid, at least, for hydration water.

Furthermore, we discussed the three characteristic temperature dependencies that are clearly observed in the proton relaxation time of protein hydration water by dielectric spectroscopy indicating a fragile-to-fragile crossover at ~ 252 K and a fragile-to-strong crossover at ~ 181 K. These crossovers can be rationalized within the FS model. The one at high- T is the result of a diffusive-to-subdiffusive transition for the water protons. The low- T crossover corresponds to the cooperative rearrangement of the HBs [74]. In hydration water, the low- T crossover occurs at the Widom line [190]. However, it is still unclear how this result relates to the bulk water, where simulations with atomistic models only find one dynamic crossover [1].

Two dynamic crossovers are observed also in the self-diffusion coefficient in nanofilms of supercooled water on top of ice, extracted from measurements of the growth rate of crystalline ice by laser-heating technique, at ~ 233 K and ~ 180 K [224]. It is quite intriguing that these temperatures are close to those of the two crossovers observed in Ref. [74]. Nevertheless, in Ref. [224] the high- T crossover is interpreted as fragile-to-strong and the low- T crossover as “strong-to-stronger.” Hence, it is still not clear whether the results of the two experiments, both for hydration water, are related.

We analyzed the water diffusion anomaly, known from experiments and numerical models, both in bulk and in confinement [237]. We showed that for nanoconfined water, it can be explained within the framework of the FS model as a consequence of the formation of HB cooperative rearranging regions (CRR) of 1 nm size [189]. When P increases, HBs in the CRR break reducing the energy cost for molecular diffusion, while the free volume increases compensating the compression and facilitating the diffusion. This analysis suggests that sub-nm confinement breaks the CRR making water diffusion under extreme confinement faster than expected. Nevertheless, a detailed checking of this interpretation in atomistic simulations is still missed. Furthermore, it is matter of debate how sub-nm fast diffusion depends on the details of the numerical approach or the HB properties [238–240]. Finally, it is an open question to understand how relevant is this cooperative mechanism in bulk water diffusion.

The decoupling of the viscosity from the translational and rotational diffusion of pure water has been explained in terms of models of dynamics heterogeneities and, alternatively, by resorting to the water

two-state model. For ionic aqueous solutions containing polyols, the decoupling of the ion mobility is associated with that of pure water, supporting the idea that ions move in water-rich domains.

In terms of amorphous ices, there has been a debate of at least 40 years whether or not the amorphous ices turn into ultraviscous liquids upon heating. Some of the key issues that have hampered a clear answer to the question are (i) many groups prepare amorphous ices starting from hexagonal ice, (ii) the crystallization temperatures of amorphous ices were different in different groups because some preparation routes lead to ice nuclei embedded in the amorphous matrix, and (iii) the glass transition temperature T_g and the crystallization temperature T_x are very close to each other. In recent years, there has been a lot of progress in this context. Protocols how to produce amorphous ices without ice nuclei and with highest T_x temperatures have been established. These T_x are so high because the amorphous ice matrix is the one that crystallizes—where in the past growth of ice seeds were mistaken as the T_x of the glassy matrix. Furthermore, quite a few studies have been devoted to prepare amorphous ices directly from liquid water instead of from crystalline ice. Specifically, low-density amorphous ice (LDA) can be prepared by ultrafast cooling of micron-sized droplets, where water vitrified in this way is called hyperquenched glassy water (HGW). Also, high-density amorphous ice (HDA) can be prepared starting from the liquid by subjecting HGW to pressure. This removes arguments about crystalline remnants and about a distorted crystalline nature for suitably prepared amorphous ices. The amorphous ices made in these ways are ideal to map the T_g s and T_x s for both LDA and HDA. These studies have shown that there is a window of up to 20 K between T_g and T_x in the pressure range up to 0.3 GPa, in which the amorphous ices turn into ultraviscous liquids. It could even be shown that many thousand relaxation times pass before crystallization turns these ultraviscous liquids into crystalline solids. These findings strengthen the suggestion made back in 2008 by Winkel et al., who for the first time claimed to have observed the liquid–liquid transition in bulk water experimentally by decompressing amorphous ice at 140 K to below 0.07 GPa. Now that the window is known, in which the ultraviscous low-density (LDL) and high-density liquids (HDL) exist, future studies should aim at preparing these liquids in the narrow window of stability, revert back and forth between the two with hysteresis—and characterize the nature of the liquids based on different methods that allow to study the sample, while it is kept under pressure and low temperature. Such experiments could be elastic and inelastic scattering, laser spectroscopy, heat conduction or heat capacity measurements, to name just a few.

Among the different approaches employed to probe water in the no-man's land based on the use of environments favoring supercooling, as confinement in nanoporous systems or hydration of macromolecules, solvation revealed to be the less invasive on the structure of the water network [372]. A model system that

has been used in a number of fundamental studies in such sense is aqueous LiCl [370], for which vitrification takes place easily at concentrations of 10 mol% or above, and the water local structure is not significantly distorted with respect to the bulk liquid [412]. The high-salt concentration behavior of these solutions has been largely characterized experimentally [372] and revealed the lack of a causality link between the observed polymorphism in the glassy state and the existence of a liquid–liquid transition in the undercooled salty solution. However, for being significative for the bulk water case, this link should be investigated for much higher dilution solutions. The access to a higher degree of dilution is prone to the use of very fast cooling rates in order to force the system to freeze in an amorphous state at ambient pressure; then, the deep undercooled state is inaccessible to usual techniques, such as neutron or x-ray diffraction and small-angle scattering, like for the bulk water case. However, in the case of salty solutions the relevant nucleation timescales appear to be much slower than in bulk water and compatible with those which can be probed with ultrafast spectroscopies or X-FEL fast diffraction techniques. An exciting prospective is then to access the deeply undercooled state of those systems in a much larger temperature range than pure water, by applying these new techniques, and then extrapolate the pure water behavior.

With regard to the role of the internal liquid-like layers at GBs, since they are commonplace in the polycrystalline structures of large ice masses, one avenue of future investigation should be directed toward understanding the role of these confined supercooled liquid layers on grain dynamics under the influence of external stresses. Specific questions in this context include how the internal pre-melt channels of the GB network may enhance mass transport and how the liquid-like nature of these channels affects friction in GB sliding processes.

In this review, we did not cover the results on *ab initio* simulations of water. We refer the reader, for example, to Refs. [413–418]. In this context, deep neural networks have been recently used to speed up *ab initio* calculations maintaining the accuracy of the *ab initio* techniques [419–422].

The disclosure of supercooled water's full chemical–physical behavior is important both for the pure liquid and for the influence that it has in solutions or in confinement. Thanks to experimental and computational studies in the next years we have a chance to improve our understanding of the thermodynamic scenario, the structural characteristics of the low-density and high-density liquids, the dynamics including the crossovers and the relation between translations and rotations, together with the influence of the hydrogen bond network on them. Finally, a lot of research is and will be also related to applications like micron-sized droplets common in Earth's atmosphere and responsible for climate conditions, hydration water, especially close to large biomolecules, cryopreservation, glacier and ice sheets connected to Earth climate, grain and

grain boundaries present in many natural and artificial phenomena, among other relevant applications.

Acknowledgements V.F.-L., J.B., C.M.T., C.G., R.B., and T.L. gratefully acknowledge financial support by the Austrian Science Fund (FWF, project I1392) and Deutsche Forschungsgemeinschaft (DFG, grant no. BO1301/12-1 and grant no. BO1301/15-1). J.B., V.F.-L., and C.M.T. are recipients of a DOC fellowship of the Austrian Academy of Sciences. L.E.C. and G.F. acknowledge support by Spanish grant PGC2018-099277-B-C22 (MCIN/AEI/10.13039/501100011033/ERDF “A way to make Europe”). L.E.C. acknowledges support by grant no. 5757200 (APIF_18_19 Universitat de Barcelona). G.F. acknowledges support by ICREA Foundation (ICREA Academia prize). I.d.A.R. and M.d.K. acknowledge support from CNPq, Fapesp grant 2016/23891-6 and the Center for Computing in Engineering & Sciences—Fapesp/Cepid no. 2013/08293-7. IdAR and MdK acknowledge the National Laboratory for Scientific Computing (LNCC/MCTI, Brazil) for providing HPC resources of the SDumont supercomputer. URL: <http://sdumont.lncc.br>. J.M.M.d.O., F.S., and G.A.A. acknowledge support from CONICET, UNS, and ANPCyT (PICT2015/1893 and PICT2017/3127). P.H.P. thanks NSERC Canada, ACENET, and Compute Canada for support. G.A.A. and H.R.C. acknowledge support from CONICET, UBA, and CNEA for organizing the 3rd International Workshop “Structure and Dynamics of Glassy, Supercooled and Nanoconfined Fluids,” Buenos Aires (Argentina), July 2019, which was the germ of this review work.

Author contribution statement

P.G. and G.A. conceived the idea and organized the general framework. All authors wrote parts of the paper and revised the final manuscript.

References

1. P. Gallo, K. Amann-Winkel, C.A. Angell, M.A. Anisimov, F. Caupin, C. Chakravarty, E. Lascaris, T. Loerting, A.Z. Panagiotopoulos, J. Russo, J.A. Sellberg, H.E. Stanley, H. Tanaka, C. Vega, L. Xu, L.G.M. Pettersson, *Chem. Rev.* **116**(13), 7463 (2016)
2. P. Gallo, H.E. Stanley, *Science* **358**(6370), 1543 (2017)
3. P.G. Debenedetti, *J. Condens. Matter Phys.* **15**(45), R1669 (2003)
4. O. Mishima, H.E. Stanley, *Nature* **396**(6709), 329 (1998)
5. C.A. Angell, *Ann. Rev. Phys.* **34**(1), 593 (1983)
6. R.J. Speedy, C.A. Angell, *J. Chem. Phys.* **65**(3), 851 (1976)
7. O. Mishima, L.D. Calvert, E. Whalley, C. Ld, W. E, L.D. Calvert, E. Whalley, *Nature* **310**, 393 (1984)
8. O. Mishima, L.D. Calvert, E. Whalley, *Nature* **314**(6006), 76 (1985)
9. O. Mishima, *J. Chem. Phys.* **100**(8), 5910 (1994)
10. P.H. Handle, T. Loerting, F. Sciortino, *Proc. Natl. Acad. Sci. U.S.A.* **114**(51), 13336 (2017)
11. C.G. Salzmann, *J. Chem. Phys.* **150**(6), 060901 (2019)
12. G. Franzese, H.E. Stanley, in *Water and Life: The Unique Properties of H₂O*. ed. by R.M. Lynden-Bell, S. Conway Morris, J.D. Barrow, J.L. Finney, C. (Harper (CRC Press, 2010)
13. K. Amann-Winkel, R. Böhmer, F. Fujara, C. Gainaru, B. Geil, T. Loerting, *Rev. Mod. Phys.* **88**, 1 (2016)
14. H.E. Stanley, J. Teixeira, A. Geiger, R.L. Blumberg, *Physica A* **106**, 260 (1981)
15. R.J. Speedy, *J. Phys. Chem.* **86**(6), 982 (1982)
16. P.H. Poole, F. Sciortino, U. Essmann, H.E. Stanley, *Nature* **360**(6402), 324 (1992)
17. P.H. Poole, F. Sciortino, T. Grande, H.E. Stanley, C.A. Angell, *Phys. Rev. Lett.* **73**(12), 1632 (1994)
18. C.A. Angell, *Science* **319**(5863), 582 (2008)
19. H.E. Stanley, J. Teixeira, *J. Chem. Phys.* **73**(7), 3404 (1980)
20. S. Sastry, P.G. Debenedetti, F. Sciortino, H.E. Stanley, *Phys. Rev. E* **53**(6), 6144 (1996)
21. G. Franzese, H.E. Stanley, *J. Condens. Matter Phys.* **19**(20), 205126 (2007)
22. K. Stokely, M.G. Mazza, H.E. Stanley, G. Franzese, *Proc. Natl. Acad. Sci. U. S. A.* **107**, 1301 (2010)
23. M.G. Mazza, K. Stokely, H.E. Stanley, G. Franzese, *J. Chem. Phys.* **137**(20), 204502 (2012)
24. S. Woutersen, B. Ensing, M. Hilbers, Z. Zhao, C.A. Angell, *Science* **359**(6380), 1127 (2018)
25. K.H. Kim, A. Späh, H. Pathak, F. Perakis, D. Mariedahl, K. Amann-Winkel, J.A. Sellberg, J.H. Lee, S. Kim, J. Park, K.H. Nam, T. Katayama, A. Nilsson, *Science* **358**(6370), 1589 (2017)
26. K.H. Kim, K. Amann-Winkel, N. Giovambattista, A. Späh, F. Perakis, H. Pathak, M.L. Parada, C. Yang, D. Mariedahl, T. Eklund et al., *Science* **370**(6519), 978 (2020)
27. P.L. Chau, A.J. Hardwick, *Mol. Phys.* **93**(3), 511 (1998)
28. J.R. Errington, P.G. Debenedetti, *Nature* **409**(6818), 318 (2001)
29. Y.I. Naberukhin, V. Voloshin, N. Medvedev, *Mol. Phys.* **73**(4), 917 (1991)
30. A. Oleinikova, I. Brovchenko, *J. Condens. Matter Phys.* **18**(36), S2247 (2006)
31. E. Shiratani, M. Sasai, *J. Chem. Phys.* **104**(19), 7671 (1996)
32. E. Shiratani, M. Sasai, *J. Chem. Phys.* **108**(8), 3264 (1998)
33. G.A. Appignanesi, J.A.R. Fris, F. Sciortino, *Eur. Phys. J. E* **29**(3), 305 (2009)
34. S.R. Accordino, J.A.R. Fris, F. Sciortino, G.A. Appignanesi, *Eur. Phys. J. E* **34**(5), 48 (2011)
35. M.J. Cuthbertson, P.H. Poole, *Phys. Rev. Lett.* **106**(11), 115706 (2011)
36. J. Russo, H. Tanaka, *Nat. Comm.* **5**(1), 3556 (2014)
37. R. Shi, J. Russo, H. Tanaka, *J. Chem. Phys.* **149**(22), 224502 (2018)
38. R. Foffi, J. Russo, F. Sciortino, *J. Chem. Phys.* **154**(18), 184506 (2021)
39. P. Gallo, F. Sciortino, P. Tartaglia, S.H. Chen, *Phys. Rev. Lett.* **76**(15), 2730 (1996)
40. F. Sciortino, P. Gallo, P. Tartaglia, S.H. Chen, *Phys. Rev. E* **54**(6), 6331 (1996)
41. R. Torre, P. Bartolini, R. Righini, *Nature* **428**(6980), 296 (2004)

42. C. Angell, J. Phys. Chem. **97**(24), 6339 (1993)
43. K. Ito, C.T. Moynihan, C.A. Angell, Nature **398**(6727), 492 (1999)
44. F.W. Starr, S. Harrington, F. Sciortino, H.E. Stanley, Phys. Rev. Lett. **82**(18), 3629 (1999)
45. F.W. Starr, C.A. Angell, H.E. Stanley, Phys. A: Stat. Mech. Appl. **323**, 51 (2003)
46. L. Liu, S.H. Chen, A. Faraone, C.W. Yen, C.Y. Mou, Phys. Rev. Lett. **95**(11), 117802 (2005)
47. A. Faraone, L. Liu, C.Y. Mou, C.W.C.W. Yen, S.H.S.H. Chen, J. Chem. Phys. **121**(22), 10843 (2004)
48. F. Mallamace, C. Branca, C. Corsaro, N. Leone, J. Spooen, S.H. Chen, H.E. Stanley, Proc. National Acad. Sci. **107**(52), 22457 (2010)
49. P. Gallo, M. Rovere, J. Chem. Phys. **137**(16), 164503 (2012)
50. M. De Marzio, G. Camisasca, M. Rovere, P. Gallo, J. Chem. Phys. **144**(7), 074503 (2016)
51. M. De Marzio, G. Camisasca, M. Rovere, P. Gallo, J. Chem. Phys. **146**(8), 084502 (2017)
52. L. Xu, P. Kumar, S.V. Buldyrev, S.H. Chen, P.H. Poole, F. Sciortino, H.E. Stanley, Proc. Natl. Acad. Sci. U. S. A. **102**(46), 16558 (2005)
53. M. De Marzio, G. Camisasca, M. Rovere, P. Gallo, Front. Phys. **13**(1), 136103 (2018)
54. P. Kumar, G. Franzese, H.E. Stanley, Phys. Rev. Lett. **100**, 105701 (2008)
55. P. Gallo, M. Rovere, E. Spohr, Phys. Rev. Lett. **85**(20), 4317 (2000)
56. P. Gallo, M. Rovere, E. Spohr, J. Chem. Phys. **113**(24), 11324 (2000)
57. P. Gallo, M. Rovere, S.H. Chen, J. Phys. Chem. Lett. **1**(4), 729 (2010)
58. D. Corradini, S.V. Buldyrev, P. Gallo, H.E. Stanley, Phys. Rev. E **81**(6), 061504 (2010)
59. E.G. Strelakova, D. Corradini, M.G. Mazza, S.V. Buldyrev, P. Gallo, G. Franzese, H.E. Stanley, J. Biol. Phys. **38**(1), 97–111 (2012)
60. S.H. Chen, L. Liu, A. Faraone, Phys. Rev. Lett. **97**, 189803 (2006)
61. F. Mallamace, M. Broccio, C. Corsaro, A. Faraone, U. Wanderlingh, L. Liu, C.Y. Mou, S.H. Chen, J. Chem. Phys. **124**(16), 161102 (2006)
62. F. Mallamace, M. Broccio, C. Corsaro, A. Faraone, D. Majolino, V. Venuti, L. Liu, C.Y. Mou, S.H. Chen, Proc. Natl. Acad. Sci. U. S. A. **104**(2), 424 (2007)
63. S.H. Chen, F. Mallamace, C.Y. Mou, M. Broccio, C. Corsaro, A. Faraone, L. Liu, Proc. Natl. Acad. Sci. U.S.A. **103**(35), 12974 (2006)
64. H. Frauenfelder, G. Chen, J. Berendzen, P.W. Fenimore, H. Jansson, B.H. McMahon, I.R. Stroe, J. Swenson, R.D. Young, Proc. Natl. Acad. Sci. U. S. A. **106**(13), 5129 (2009)
65. S.H. Chen, L. Liu, X. Chu, Y. Zhang, E. Fratini, P. Baglioni, A. Faraone, E. Mamontov, J. Chem. Phys. **125**(17), 171103 (2006)
66. J. Swenson, Phys. Rev. Lett. **97**(18), 189801 (2006)
67. S. Cervený, J. Colmenero, A. Alegría, Phys. Rev. Lett. **97**(18), 189802 (2006)
68. A. Iorio, G. Camisasca, P. Gallo, J. Mol. Liq. **282**, 617 (2019)
69. A. Iorio, G. Camisasca, P. Gallo, Sci. China Phys. Mech. Astron. **62**(10), 1 (2019)
70. D. Corradini, E.G. Strelakova, H.E. Stanley, P. Gallo, Sci. Rep. **3**, 1218 (2013)
71. G. Camisasca, M. De Marzio, D. Corradini, P. Gallo, J. Chem. Phys. **145**(4), 044503 (2016)
72. G. Camisasca, M. De Marzio, P. Gallo, J. Chem. Phys. **153**(22), 224503 (2020)
73. P. Kumar, Z. Yan, L. Xu, M.G. Mazza, S.V. Buldyrev, S.H. Chen, S. Sastry, H.E. Stanley, Phys. Rev. Lett. **97**(17), 177802 (2006)
74. M.G. Mazza, K. Stokely, S.E. Pagnotta, F. Bruni, H.E. Stanley, G. Franzese, Proc. Natl. Acad. Sci. U. S. A. **108**(50), 19873 (2011)
75. C.A. Angell, E.J. Sare, J. Chem. Phys. **49**(10), 4713 (1968)
76. C.A. Angell, E.J. Sare, J. Chem. Phys. **52**(3), 1058 (1970)
77. H. Kanno, J. Phys. Chem. **91**(7), 1967 (1987)
78. Y. Suzuki, O. Mishima, Phys. Rev. Lett. **85**(6), 1322 (2000)
79. Y. Suzuki, O. Mishima, J. Chem. Phys. **117**(4), 1673 (2002)
80. O. Mishima, J. Chem. Phys. **126**(24), 244507 (2007)
81. D. Corradini, M. Rovere, P. Gallo, J. Chem. Phys. **132**(13), 134508 (2010)
82. D. Corradini, P. Gallo, J. Phys. Chem. B **115**(48), 14161 (2011)
83. E. Schulson, P. Duval, *Creep and Fracture of Ice* (Cambridge University Press, Cambridge, 2009)
84. J.G. Dash, A.W. Rempel, J.S. Wettlaufer, Rev. Mod. Phys. **78**(3), 695 (2006)
85. L. Benatov, J.S. Wettlaufer, Phys. Rev. E **70**(6), 061606 (2004)
86. E.S. Thomson, L. Benatov, J.S. Wettlaufer, Phys. Rev. E **82**(3), 039907 (2010)
87. E.S. Thomson, H. Hansen-Goos, J.S. Wettlaufer, L.A. Wilen, J. Chem. Phys. **138**(12), 124707 (2013)
88. J.G. Dash, H. Fu, J.S. Wettlaufer, Rep. Prog. Phys. **58**(1), 115 (1995)
89. T. Bartels-Rausch, V. Bergeron, J.H.E. Cartwright, R. Escribano, J.L. Finney, H. Grothe, P.J. Gutiérrez, J. Haapala, W.F. Kuhs, J.B.C. Pettersson, S.D. Price, C.I. Sainz-Díaz, D.J. Stokes, G. Strazzulla, E.S. Thomson, H. Trinks, N. Uras-Aytemiz, Rev. Mod. Phys. **84**(2), 885 (2012)
90. F. Sciortino, I. Saika-Voivod, P.H. Poole, Phys. Chem. Chem. Phys. **13**, 19759 (2011)
91. T.A. Kesselring, G. Franzese, S.V. Buldyrev, H.J. Herrmann, H.E. Stanley, Sci. Rep. **2**(1), 1–6 (2012)
92. T.A. Kesselring, E. Lascaris, G. Franzese, S.V. Buldyrev, H.J. Herrmann, H.E. Stanley, J. Chem. Phys. **138**(24), 244506 (2013)
93. J.C. Palmer, F. Martelli, Y. Liu, R. Car, A.Z. Panagiotopoulos, P.G. Debenedetti, Nature **510**(7505), 385 (2014)
94. F. Smallenburg, P.H. Poole, F. Sciortino, Mol. Phys. **113**(17–18), 2791 (2015)
95. P.G. Debenedetti, F. Sciortino, G.H. Zerze, Science **369**(6501), 289 (2020)
96. P. Gallo, D. Corradini, M. Rovere, Nat. Comm. **5**, 1 (2014)
97. D. Corradini, M. Rovere, P. Gallo, J. Chem. Phys. **143**(11), 114502 (2015)

98. P. Chitnelawong, F. Sciortino, P.H. Poole, J. Chem. Phys. **150**(23), 234502 (2019)
99. L. Rovigatti, V. Bianco, J.M. Tavares, F. Sciortino, J. Chem. Phys. **146**(4), 041103 (2017)
100. V. Holten, J.C. Palmer, P.H. Poole, P.G. Debenedetti, M.A. Anisimov, J. Chem. Phys. **140**(10), 104502 (2014)
101. Y. Tanaka, Eur. Phys. J. E **35**, 3 (2012)
102. R.S. Singh, J.W. Biddle, P.G. Debenedetti, M.A. Anisimov, J. Chem. Phys. **144**(14), 144504 (2016)
103. J.W. Biddle, R.S. Singh, E.M. Sparano, F. Ricci, M.A. González, C. Valeriani, J.L.F. Abascal, P.G. Debenedetti, M.A. Anisimov, F. Caupin, J. Chem. Phys. **146**(3), 034502 (2017)
104. F. Caupin, M.A. Anisimov, J. Chem. Phys. **151**(3), 034503 (2019)
105. M.A. Anisimov, M. Duška, F. Caupin, L.E. Amrhein, A. Rosenbaum, R.J. Sadus, Phys. Rev. X **8**(1), 011004 (2018)
106. L. Kringle, W.A. Thornley, B.D. Kay, G.A. Kimmel, Science **369**(6510), 1490 (2020)
107. C. Huang, K.T. Wikfeldt, T. Tokushima, D. Nordlund, Y. Harada, U. Bergmann, M. Niebuhr, T. Weiss, Y. Horikawa, M. Leetmaa et al., Proc. Natl. Acad. Sci. U. S. A. **106**(36), 15214 (2009)
108. R.J. Speedy, J. Condens. Matter Phys. **16**(37), 6811 (2004)
109. J. Russo, K. Akahane, H. Tanaka, Proc. Natl. Acad. Sci. U. S. A. **115**(15), E3333 (2018)
110. G. Zhao, Y.J. Yu, J.L. Yan, M.C. Ding, X.G. Zhao, H.Y. Wang, Phys. Rev. B **93**, 14 (2016)
111. F. Caupin, J. Non-Cryst. Solids **407**, 441 (2015)
112. G. Pallares, M.E.M. Azouzi, M.A. Gonzalez, J.L. Aragonés, J.L.F. Abascal, C. Valeriani, F. Caupin, Proc. Natl. Acad. Sci. U. S. A. **111**(22), 7936 (2014)
113. V. Holten, C. Qiu, E. Guillermin, M. Wilke, J. Rička, M. Frenz, F. Caupin, J. Phys. Chem. Lett. **8**(22), 5519 (2017)
114. D.C. Malaspina, J.A.R. Fris, G.A. Appignanesi, F. Sciortino, E.P.L. Europhys. Lett. **88**(1), 16003 (2009)
115. S.R. Accordino, D.C. Malaspina, J.A.R. Fris, G.A. Appignanesi, Phys. Rev. Lett. **106**(2), 029801 (2011)
116. S.R. Accordino, D.C. Malaspina, J.A. Rodriguez Fris, L.M. Alarcón, G.A. Appignanesi, Phys. Rev. E **85**, 031503 (2012)
117. J.M. Montes de Oca, J.A.R. Fris, S.R. Accordino, D.C. Malaspina, G.A. Appignanesi, Eur. Phys. J. E **39**(12), 124 (2016)
118. J.G. Constantin, A.R. Fris, G. Appignanesi, M. Carignano, I. Szleifer, H. Corti, Eur. Phys. J. E **34**(11), 126 (2011)
119. A.R. Verde, J.M. Montes de Oca, S.R. Accordino, L.M. Alarcón, G.A. Appignanesi, J. Chem. Phys. **150**(24), 244504 (2019)
120. J.M. Montes de Oca, S.R. Accordino, A.R. Verde, L.M. Alarcón, G.A. Appignanesi, Phys. Rev. E **99**(6), 062601 (2019)
121. K.T. Wikfeldt, A. Nilsson, L.G.M. Pettersson, Phys. Chem. Chem. Phys. **13**(44), 19918 (2011)
122. B. Santra, R.A. DiStasio, F. Martelli, R. Car, Mol. Phys. **113**(17–18), 2829 (2015)
123. G. Camisasca, D. Schlesinger, I. Zhovtobriukh, G. Pitsevich, L.G. Pettersson, J. Chem. Phys. **151**(3), 034508 (2019)
124. F.H. Stillinger, *Energy Landscapes, Inherent Structures, and Condensed-Matter Phenomena* (Princeton University Press, New Jersey, 2015)
125. F. Sciortino, J. Stat. Mech.: Theory Exp. **2005**(05), P05015 (2005)
126. H.J.C. Berendsen, J.R. Grigera, T.P. Straatsma, J. Phys. Chem. **91**(24), 6269 (1987)
127. J.L.F. Abascal, C. Vega, J. Chem. Phys. **123**(23), 234505 (2005)
128. J.M. Montes de Oca, F. Sciortino, G.A. Appignanesi, J. Chem. Phys. **152**(24), 244503 (2020)
129. F. Sciortino, A. Geiger, H.E. Stanley, Nature **354**(6350), 218 (1991)
130. S. Saito, B. Bagchi, I. Ohmine, J. Chem. Phys. **149**(12), 124504 (2018)
131. D. Laage, Science **311**(5762), 832 (2006)
132. J.L. Finney, A. Hallbrucker, I. Kohl, A.K. Soper, D.T. Bowron, Phys. Rev. Lett. **88**(22), 225503 (2002)
133. J. Huang, L.S. Bartell, J. Phys. Chem. **99**(12), 3924 (1995)
134. A. Manka, H. Pathak, S. Tanimura, J. Wölk, R. Strey, B.E. Wyslouzil, Phys. Chem. Chem. Phys. **14**(13), 4505 (2012)
135. H. Laksmono, T.A. McQueen, J.A. Sellberg, N.D. Loh, C. Huang, D. Schlesinger, R.G. Sierra, C.Y. Hampton, D. Nordlund, M. Beye, A.V. Martin, A. Barty, M.M. Seibert, M. Messerschmidt, G.J. Williams, S. Boutet, K. Amann-Winkel, T. Loerting, L.G.M. Pettersson, M.J. Bogan, A. Nilsson, J. Phys. Chem. Lett. **6**(14), 2826 (2015)
136. T. Li, D. Donadio, G. Galli, Nat. Comm. **4**(1), 1887 (2013)
137. S.M.A. Malek, R.K. Bowles, I. Saika-Voivod, F. Sciortino, P.H. Poole, Eur. Phys. J. E **40**(11), 98 (2017)
138. S.M.A. Malek, F. Sciortino, P.H. Poole, I. Saika-Voivod, J. Condens. Matter Phys. **30**(14), 144005 (2018)
139. S.M.A. Malek, P.H. Poole, I. Saika-Voivod, Nat. Comm. **9**, 1 (2018)
140. J. Hrubý, V. Vinš, R. Mareš, J. Hykl, J. Kalová, J. Phys. Chem. Lett. **5**(3), 425 (2014)
141. V. Vinš, M. Fransen, J. Hykl, J. Hrubý, J. Phys. Chem. B **119**(17), 5567 (2015)
142. V. Vinš, J. Hošek, J. Hykl, J. Hrubý, J. Chem. Eng. Data **62**(11), 3823 (2017)
143. Y. Lü, B. Wei, Sci. China Ser. G-Phys. Mech. Astron. **49**(5), 616 (2006)
144. Y.J. Lü, B. Wei, Appl. Phys. Lett. **89**(16), 164106 (2006)
145. F. Chen, P.E. Smith, J. Chem. Phys. **126**(22), 221101 (2007)
146. L. VIERERBLOVÁ, J. Kolafa, Phys. Chem. Chem. Phys. **13**(44), 19925 (2011)
147. M.R. Feeney, P.G. Debenedetti, Ind. Eng. Chem. Res. **42**(25), 6396 (2003)
148. J. Hrubý, in *Proceedings of the 16th International Conference on Nucleation and Atmospheric Aerosols, Kyoto, 26–30 July 2004* Eds by M. Kasahara and M. Kulmala, Kyoto University Press (2004)

149. S.M.A. Malek, P.H. Poole, I. Saika-Voivod, J. Chem. Phys. **150**(23), 234507 (2019)
150. X. Wang, K. Binder, C. Chen, T. Koop, U. Pöschl, H. Su, Y. Cheng, Phys. Chem. Chem. Phys. **21**(6), 3360 (2019)
151. C. Vega, E. de Miguel, J. Chem. Phys. **126**(15), 154707 (2007)
152. J. Cruzan, L. Braly, K. Liu, M. Brown, J. Loeser, R. Saykally, Science **271**(5245), 59 (1996)
153. M.R. Viant, J.D. Cruzan, D.D. Lucas, M.G. Brown, K. Liu, R.J. Saykally, J. Phys. Chem. A **101**(48), 9032 (1997)
154. W.A.P. Luck, J. Molecular Struct. **448**(2), 131 (1998)
155. K. Nauta, R.E. Miller, Science **287**(5451), 293 (2000)
156. C. Pérez, D.P. Zaleski, N.A. Seifert, B. Temelso, G.C. Shields, Z. Kisiel, B.H. Pate, Angew. Chem. Int. Ed. **53**(52), 14368 (2014)
157. G. Li, Y.Y. Zhang, Q. Li, C. Wang, Y. Yu, B. Zhang, H.S. Hu, W. Zhang, D. Dai, G. Wu, D.H. Zhang, J. Li, X. Yang, L. Jiang, Nature Commun. **11**(1), 5449 (2020)
158. E. Clementi, W. Kołos, G.C. Lie, G. Ranghino, Int. J. Quantum Chem. **17**(3), 377 (1980)
159. A. Rakshit, P. Bandyopadhyay, J.P. Heindel, S.S. Xantheas, J. Chem. Phys. **151**(21), 214307 (2019)
160. R. Ludwig, Angew. Chem. **40**(10), 1808 (2001)
161. P. Barnes, J.L. Finney, J.D. Nicholas, J.E. Quinn, Nature **282**(5738), 459 (1979)
162. U. Góra, R. Podeszwa, W. Cencek, K. Szalewicz, J. Chem. Phys. **135**(22), 224102 (2011)
163. G.A. Cisneros, K.T. Wikfeldt, L. Ojamäe, J. Lu, Y. Xu, H. Torabifard, A.P. Bartók, G. Csányi, V. Molinero, F. Paesani, Chem. Rev. **116**(13), 7501 (2016)
164. G.R. Medders, V. Babin, F. Paesani, J. Chem. Theory Comput. **10**(8), 2906 (2014)
165. M. Riera, E. Lambros, T.T. Nguyen, A.W. Götz, F. Paesani, Chem. Sci. **10**(35), 8211 (2019)
166. M. Riera, E.P. Yeh, F. Paesani, J. Chem. Theory Comput. **16**(4), 2246 (2020)
167. M.L. Laury, L.P. Wang, V.S. Pande, T. Head-Gordon, J.W. Ponder, J. Phys. Chem. B **119**(29), 9423 (2015)
168. J.W. Ponder, C. Wu, P. Ren, V.S. Pande, J.D. Chodera, M.J. Schnieders, I. Haque, D.L. Mobley, D.S. Lambrecht, R.A. DiStasio, M. Head-Gordon, G.N.I. Clark, M.E. Johnson, T. Head-Gordon, J. Phys. Chem. B **114**(8), 2549 (2010)
169. E.D. Glendenning, J. Phys. Chem. A **109**(51), 11936 (2005)
170. V. Molinero, E.B. Moore, J. Phys. Chem. B **113**(13), 4008 (2009)
171. V. Holtén, D.T. Limmer, V. Molinero, M.A. Anisimov, J. Chem. Phys. **138**(17), 174501 (2013)
172. L. Lupi, A. Hudait, B. Peters, M. Grünwald, R. Gotchy Mullen, A.H. Nguyen, V. Molinero, Nature **551**, 218 (2017)
173. F. Leoni, R. Shi, H. Tanaka, J. Russo, J. Chem. Phys. **151**, 4 (2019)
174. H. Chan, M.J. Cherukara, B. Narayanan, T.D. Loeffler, C. Benmore, S.K. Gray, S.K.R.S. Sankaranarayanan, Nat. Comm. **10**(1), 379 (2019)
175. T. James, D.J. Wales, J. Hernández-Rojas, Chem. Phys. Lett. **415**(4), 302 (2005)
176. J. Hernández-Rojas, F. Calvo, F. Rabilloud, J. Bretón, J.M. Gomez Llorente, J. Phys. Chem. A **114**(27), 7267 (2010)
177. W.C. Röntgen, Ann. Phys. **281**(1), 91 (1892)
178. S. Strässler, C. Kittel, Phys. Rev. **139**, A758 (1965)
179. H. Tanaka, Phys. Rev. Lett. **80**, 5750 (1998)
180. H. Tanaka, Phys. Rev. E **62**(5), 6968 (2000)
181. S. Sastry, P.G. Debenedetti, F. Sciortino, H.E. Stanley, Phys. Rev. E **53**, 6144 (1996)
182. G. Franzese, H.E. Stanley, J. Condens. Matter Phys. **14**(9), 2201 (2002)
183. G. Franzese, H. Eugene Stanley, Physica A **314**(1), 508 (2002)
184. G. Franzese, K. Stokely, X.Q. Chu, P. Kumar, M.G. Mazza, S.H. Chen, H.E. Stanley, J. Condens. Matter Phys. **20**(49), 494210 (2008)
185. P. Kumar, G. Franzese, H.E. Stanley, Phys. Rev. Lett. **100**(10), 105701 (2008)
186. P. Kumar, G. Franzese, H.E. Stanley, J. Condens. Matter Phys. **20**(24), 244114 (2008)
187. G. Franzese, F. de los Santos, J. Phys.: Condens. Matter. **21**, 504107 (2009)
188. F. de los Santos, G. Franzese, J. Phys. Chem. B **115**, 14311 (2011)
189. F. de los Santos, G. Franzese, Phys. Rev. E **85**(1), 010602 (2012)
190. V. Bianco, G. Franzese, Sci. Rep. **4**, 4440 (2014)
191. L.E. Coronas, V. Bianco, A. Zantop, G. Franzese, (2016). ArXiv e-prints [arXiv:1610.00419](https://arxiv.org/abs/1610.00419)
192. L.E. Coronas, O. Vilanova, V. Bianco, F. de los Santos, G. Franzese, (2020). ArXiv e-prints [arXiv:2004.03646](https://arxiv.org/abs/2004.03646)
193. G. Franzese, A. Hernando-Martínez, P. Kumar, M.G. Mazza, K. Stokely, E.G. Strelakova, F. de los Santos, H.E. Stanley, J. Condens. Matter Phys. **22**(28), 284103 (2010)
194. M.G. Mazza, K. Stokely, E.G. Strelakova, H.E. Stanley, G. Franzese, Comput. Phys. Commun. **180**(4), 497 (2009)
195. V. Bianco, G. Franzese, J. Mol. Liq. **285**, 727 (2019)
196. N.A. Chumakovskii, M.N. Rodnikova, J. Mol. Liq. **106**(2–3), 167 (2003)
197. D. Eisenberg, W. Kauzmann, *The Structure and Properties of Water* (Oxford University Press, New York, 1969)
198. S.J. Suresh, V.M. Naik, J. Chem. Phys. **113**(21), 9727 (2000)
199. M. Henry, ChemPhysChem **3**(7), 561 (2002)
200. M.I. Heggie, C.D. Latham, S.C.P. Maynard, R. Jones, Chem. Phys. Lett. **249**(5–6), 485 (1996)
201. W. Götze, L. Sjogren, Reports. Prog. Phys. **55**(3), 241 (1992)
202. W. Götze, *Complex Dynamics of Glass-Forming Liquids* (Oxford University Press, New York, USA, 2009)
203. J.L. Abascal, C. Vega, J. Chem. Phys. **133**(23), 234502 (2010)
204. C.A. Angell, Science **267**, 1924 (1995)
205. M.D. Ediger, C.A. Angell, S.R. Nagel, J. Phys. Chem. **100**(31), 13200 (1996)
206. R. Böhmer, K. Ngai, C.A. Angell, D. Plazek, J. Chem. Phys. **99**(5), 4201 (1993)
207. G. Camisasca, N. Galamba, K.T. Wikfeldt, L.G.M. Pettersson, J. Chem. Phys. **150**(22), 224507 (2019)

208. L. Tenuzzo, G. Camisasca, P. Gallo, *Molecules* **25**(19), 4570 (2020)
209. G. Camisasca, A. Iorio, M. De Marzio, P. Gallo, *J. Mol. Liq.* **268**, 903 (2018)
210. A. Magno, P. Gallo, *J. Phys. Chem. Lett.* **2**(9), 977 (2011)
211. M. Lagi, X. Chu, C. Kim, F. Mallamace, P. Baglioni, S.H. Chen, *J. Phys. Chem. B* **112**(6), 1571 (2008)
212. L. Cordone, G. Cottone, A. Cupane, A. Emanuele, S. Giuffrida, M. Levantino, *Curr. Org. Chem.* **19**(17), 1684 (2015)
213. S.H. Chen, L. Liu, E. Fratini, P. Baglioni, A. Faraone, E. Mamontov, *Proc. Natl. Acad. Sci. U. S. A.* **103**(24), 9012 (2006)
214. F. Mallamace, S.H. Chen, M. Broccio, C. Corsaro, V. Crupi, D. Majolino, V. Venuti, P. Baglioni, E. Fratini, C. Vannucci, H.E. Stanley, *J. Chem. Phys.* **127**(4), 045104 (2007)
215. W. Doster, S. Cusack, W. Petry, *Nature* **337**(6209), 754 (1989)
216. W. Doster, S. Cusack, W. Petry, *Phys. Rev. Lett.* **65**(8), 1080 (1990)
217. G. Adam, J.H. Gibbs, *J. Chem. Phys.* **43**(1), 139 (1965)
218. N. Giovambattista, S.V. Buldyrev, F.W. Starr, H.E. Stanley, *Phys. Rev. Lett.* **90**(8), 085506 (2003)
219. F. Sciortino, W. Kob, P. Tartaglia, *Phys. Rev. Lett.* **83**(16), 3214 (1999)
220. F. Sciortino, W. Kob, P. Tartaglia, *J. Phys. Cond. Matt.* **12**(29), 6525 (2000)
221. A. Scala, F.W. Starr, E. La Nave, F. Sciortino, H.E. Stanley, *Nature* **406**(6792), 166 (2000)
222. P.H. Handle, F. Sciortino, *J. Chem. Phys.* **148**(13), 134505 (2018)
223. I. Popov, P.B. Ishai, A. Khamzin, Y. Feldman, *Phys. Chem. Chem. Phys.* **18**(20), 13941 (2016)
224. Y. Xu, N.G. Petrik, R.S. Smith, B.D. Kay, G.A. Kimmel, *Proc. Natl. Acad. Sci. U. S. A.* **113**(52), 14921 (2016)
225. S.E. Pagnotta, F. Bruni, A. Bocedi, R. Senesi, A. Pietropaolo, *Biophys. J.* **96**, 1939 (2009)
226. X.Q. Chu, A. Faraone, C. Kim, E. Fratini, P. Baglioni, J.B. Leao, S.H. Chen, *J. Phys. Chem. B* **113**(15), 5001 (2009)
227. F.X. Prielmeier, E.W. Lang, R.J. Speedy, H.D. Lüdemann, *Phys. Rev. Lett.* **59**(10), 1128 (1987)
228. F.X. Prielmeier, E.W. Lang, R.J. Speedy, H.D. Lüdemann, *Ber. Bunsenges. Phys. Chem.* **92**, 1111 (1988)
229. M.R. Reddy, M. Berkowitz, *J. Chem. Phys.* **87**(11), 6682 (1987)
230. M.V. Fernández-Serra, E. Artacho, *J. Chem. Phys.* **121**(22), 11136 (2004)
231. M. Girardi, M. Szortyka, M.C. Barbosa, *Physica A* **386**(2), 692 (2007)
232. P.A. Netz, F.W. Starr, H.E. Stanley, M.C. Barbosa, *J. Chem. Phys.* **115**(1), 344 (2001)
233. J.R. Errington, P.G. Debenedetti, *Nature* **409**, 318 (2001)
234. W.A. Kamitakahara, N. Wada, *Phys. Rev. E* **77**(4), 41503 (2008)
235. S. Takahara, M. Nakano, S. Kittaka, Y. Kuroda, T. Mori, H. Hamano, T. Yamaguchi, *J. Phys. Chem. B* **103**(28), 5814 (1999)
236. N. Naguib, H. Ye, Y. Gogotsi, A.G. Yazicioglu, C.M. Megaridis, M. Yoshimura, *Nano Lett.* **4**(11), 2237 (2004)
237. J.K. Holt, H.G. Park, Y. Wang, M. Stadermann, A.B. Artyukhin, C.P. Grigoropoulos, A. Noy, O. Bakajin, *Science* **312**, 1034 (2006)
238. N. Choudhury, B.M. Pettitt, *J. Phys. Chem. B* **109**(13), 6422 (2005)
239. G. Cicero, J.C. Grossman, E. Schwegler, F. Gygi, G. Galli, *J. Am. Chem. Soc.* **130**(6), 1871 (2008)
240. C. Calero, G. Franzese, *J. Mol. Liq.* **317**, 114027 (2020)
241. J. Martí, M.C. Gordillo, *J. Chem. Phys.* **114**(23), 10486 (2001)
242. R.J. Mashl, S. Joseph, N.R. Aluru, E. Jakobsson, *Nano Lett.* **3**(5), 589 (2003)
243. Y. Liu, Q. Wang, T. Wu, L. Zhang, *J. Chem. Phys.* **123**(23), 234701 (2005)
244. P. Gallo, M. Rovere, S. Chen, *J. Condens. Matter Phys.* **22**(28), 284102 (2010)
245. P. Gallo, M. Rapinesi, M. Rovere, *J. Chem. Phys.* **117**(1), 369 (2002)
246. D. Chandler, *Nature* **437**(7059), 640 (2005)
247. M. Chaplin, *Nat. Rev. Mol. Cell Biol.* **7**(11), 861 (2006)
248. G. Franzese, V. Bianco, S. Iskrov, *Food Biophys.* **6**, 186 (2011)
249. V. Bianco, S. Iskrov, G. Franzese, *J. Biol. Phys.* **38**(1), 27 (2012)
250. G. Franzese, V. Bianco, *Food Biophys.* **8**(3), 153 (2013)
251. V. Bianco, G. Franzese, *Phys. Rev. Lett.* **115**(10), 108101 (2015)
252. O. Vilanova, V. Bianco, G. Franzese, *Multi-Scale Approach for Self-Assembly and Protein Folding* (Springer International Publishing, Cham, 2017), pp. 107–128
253. V. Bianco, N. Pagès-Gelabert, I. Coluzza, G. Franzese, *J. Mol. Liq.* **245**(Supplement C), 129 (2017)
254. V. Bianco, G. Franzese, C. Dellago, I. Coluzza, *Phys. Rev. X* **7**, 021047 (2017)
255. V. Bianco, G. Franzese, I. Coluzza, *ChemPhysChem* **21**(5), 377 (2020)
256. D. March, V. Bianco, G. Franzese, *Polymers* **13**, 1 (2021)
257. R.B. Bird, W.E. Stewart, E.N. Lightfoot, *Transport Phenomena* (Wiley, New York, 1960)
258. F. Fujara, B. Geil, H. Sillescu, G. Fleischer, *Z. Phys. B. Condens. Matter.* **88**(2), 195 (1992)
259. F.R. Blackburn, C.Y. Wang, M.D. Ediger, *J. Phys. Chem.* **100**(46), 18249 (1996)
260. E. Rössler, *Phys. Rev. Lett.* **65**(13), 1595 (1990)
261. J. Newman, K.E. Thomas-Alyea, *Electrochemical Systems* (Wiley, New York, 2004)
262. C.A. Angell, *Chem. Rev.* **90**(3), 523 (1990)
263. A. Voronel, E. Veliyulin, V.S. Machavariani, A. Kisliuk, D. Quitmann, *Phys. Rev. Lett.* **80**(12), 2630 (1998)
264. F.H. Stillinger, J.A. Hodgdon, *Phys. Rev. E* **50**(3), 2064 (1994)
265. I. Chang, H. Sillescu, *J. Phys. Chem. B* **101**(43), 8794 (1997)
266. M.T. Cicerone, P.A. Wagner, M.D. Ediger, *J. Phys. Chem. B* **101**(43), 8727 (1997)
267. M. Ediger, *J. Non-Cryst. Solids* **235–237**, 10 (1998)
268. X. Xia, P.G. Wolynes, *Proc. Natl. Acad. Sci. U. S. A.* **97**(7), 2990 (2000)

269. X. Xia, P.G. Wolynes, Phys. Rev. Lett. **86**(24), 5526 (2001)
270. X. Xia, P.G. Wolynes, J. Phys. Chem. B **105**(28), 6570 (2001)
271. J.P. Garrahan, D. Chandler, Proc. Natl. Acad. Sci. U. S. A. **100**(17), 9710 (2003)
272. Y. Jung, J.P. Garrahan, D. Chandler, Phys. Rev. E **69**, 6 (2004)
273. H.R. Corti, M.P. Longinotti, J. Fernández, E.R. López, A., Würger, in Experimental Thermodynamics Volume IX, Chap. 9.2, Transport in Supercooled Liquids (Royal Society of Chemistry, pp. 290–306 (2014)
274. J. Hallett, Proc. Phys. Soc. **82**(6), 1046 (1963)
275. Y.A. Osipov, B. Zheleznyi, N. Bondarenko, Zh. Fiz. Khim **51**(5), 1264 (1977)
276. A. Dehaoui, B. Issenmann, F. Caupin, Proc. Natl. Acad. Sci. U. S. A. **112**(39), 12020 (2015)
277. W.S. Price, H. Ide, Y. Arata, J. Phys. Chem. A **103**(4), 448 (1999)
278. J.C. Hindman, J. Chem. Phys. **60**(11), 4488 (1974)
279. E.W. Lang, H.D. Lüdemann, Ber. Bunsenges. Phys. Chem. **85**(7), 603 (1981)
280. J. Qvist, C. Mattea, E.P. Sunde, B. Halle, J. Chem. Phys. **136**(20), 204505 (2012)
281. N.J. Hestand, J.L. Skinner, J. Chem. Phys. **149**(14), 140901 (2018)
282. R. Shi, J. Russo, H. Tanaka, Proc. Natl. Acad. Sci. U. S. A. **115**(38), 9444 (2018)
283. K.R. Harris, J. Chem. Phys. **131**(5), 054503 (2009)
284. S.R. Becker, P.H. Poole, F.W. Starr, Phys. Rev. Lett. **97**, 5 (2006)
285. M.G. Mazza, N. Giovambattista, H.E. Stanley, F.W. Starr, Phys. Rev. E **76**, 3 (2007)
286. D.T. Limmer, *On the Fluctuations that Order and Frustrate Liquid Water* (University of California, Berkeley, 2013). PhD Thesis
287. S. Cervený, F. Mallamace, J. Swenson, M. Vogel, L. Xu, Chem. Rev. **116**(13), 7608 (2016)
288. I.N. Tsimpanogiannis, S.H. Jamali, I.G. Economou, T.J. Vlught, O.A. Moulton, Mol. Phys. **118**(9–10), e1702729 (2020)
289. P. Kumar, S.V. Buldyrev, S.R. Becker, P.H. Poole, F.W. Starr, H.E. Stanley, Proc. Natl. Acad. Sci. U. S. A. **104**(23), 9575 (2007)
290. B. Jana, R.S. Singh, B. Bagchi, Phys. Chem. Chem. Phys. **13**(36), 16220 (2011)
291. J.M. Stokes, R.H. Stokes, J. Phys. Chem. **62**(4), 497 (1958)
292. C.T. Moynihan, N. Balitactac, L. Boone, T.A. Litovitz, J. Chem. Phys. **55**(6), 3013 (1971)
293. E. Mamontov, J. Phys. Chem. B **113**(43), 14073 (2009)
294. Y. Suzuki, O. Mishima, J. Chem. Phys. **138**(8), 084507 (2013)
295. G. Camisasca, M.D. Marzio, M. Rovere, P. Gallo, J. Chem. Phys. **148**(22), 222829 (2018)
296. P. Gallo, D. Corradini, M. Rovere, Phys. Chem. Chem. Phys. **13**(44), 19814 (2011)
297. H.R. Corti, F.J. Norez-Pondal, C.A. Angell, Phys. Chem. Chem. Phys. **13**(44), 19741 (2011)
298. M.P. Longinotti, M.A. Carignano, I. Szleifer, H.R. Corti, J. Chem. Phys. **134**(24), 244510 (2011)
299. D.P. Miller, P.B. Conrad, S. Fucito, H.R. Corti, J.J. de Pablo, J. Phys. Chem. B **104**(44), 10419 (2000)
300. M.P. Longinotti, H.R. Corti, J. Phys. Chem. B **113**(16), 5500 (2009)
301. H.R. Corti, G.A. Frank, M.C. Marconi, J. Phys. Chem. B **112**(41), 12899 (2008)
302. P.G. Wolynes, Ann. Rev. Phys. **31**(1), 345 (1980)
303. M. Rampp, C. Buttersack, H.D. Lüdemann, Carbohyd. Res. **328**(4), 561 (2000)
304. B. Chen, E.E. Sigmund, W.P. Halperin, Phys. Rev. Lett. **96**, 14 (2006)
305. M.P. Longinotti, H.R. Corti, Electrochem. Commun. **9**(7), 1444 (2007)
306. F. Mallamace, C. Branca, C. Corsaro, N. Leone, J. Spooren, H.E. Stanley, S.H. Chen, J. Phys. Chem. B **114**(5), 1870 (2010)
307. J.A.T. González, M.P. Longinotti, H.R. Corti, J. Phys. Chem. B **119**(1), 257 (2014)
308. D. Banerjee, S.N. Bhat, S.V. Bhat, D. Leporini, Proc. Natl. Acad. Sci. U. S. A. **106**(28), 11448 (2009)
309. P. Brüggeller, E. Mayer, Nature **288**(5791), 569 (1980)
310. E. Mayer, P. Brüggeller, Nature **298**(5876), 715 (1982)
311. I. Kohl, L. Bachmann, A. Hallbrucker, E. Mayer, T. Loerting, Phys. Chem. Chem. Phys. **7**(17), 3210 (2005)
312. O. Mishima, Y. Suzuki, J. Chem. Phys. **115**(9), 4199 (2001)
313. J. Bachler, J. Giebelmann, T. Loerting, Proc. Natl. Acad. Sci. U.S.A. **118**(30), e2108194118 (2021)
314. A. Kouchi, T. Kuroda, Nature **344**(6262), 134 (1990)
315. M.H. Moore, R.L. Hudson, Astrophys. J. **401**, 353 (1992)
316. G. Leto, G.A. Baratta, Astron. Astrophys. **397**(1), 7 (2002)
317. T. Loerting, I. Kohl, W. Schustereder, K. Winkel, E. Mayer, ChemPhysChem **7**(6), 1203 (2006)
318. T. Loerting, C. Salzmann, I. Kohl, E. Mayer, A. Hallbrucker, Phys. Chem. Chem. Phys. **3**(24), 5355 (2001)
319. E.F. Burton, W.F. Oliver, Nature **135**(3413), 505 (1935)
320. G.P. Johari, A. Hallbrucker, E. Mayer, Nature **330**(6148), 552 (1987)
321. I. Kohl, L. Bachmann, E. Mayer, A. Hallbrucker, T. Loerting, Nature **435**(7041), E1 (2005)
322. D.T. Bowron, J.L. Finney, A. Hallbrucker, I. Kohl, T. Loerting, E. Mayer, A.K. Soper, J. Chem. Phys. **125**(19), 194502 (2006)
323. A. Hallbrucker, E. Mayer, G.P. Johari, J. Phys. Chem. **93**(12), 4986 (1989)
324. M.S. Elsaesser, K. Winkel, E. Mayer, T. Loerting, Phys. Chem. Chem. Phys. **12**(3), 708 (2010)
325. K. Amann-Winkel, C. Gainaru, P.H. Handle, M. Seidl, H. Nelson, R. Bohmer, T. Loerting, Proc. Natl. Acad. Sci. U. S. A. **110**(44), 17720 (2013)
326. N. Giovambattista, T. Loerting, B.R. Lukanov, F.W. Starr, Sci. Rep. **2**, 1 (2012)
327. M. Seidl, M.S. Elsaesser, K. Winkel, G. Zifferer, E. Mayer, T. Loerting, Phys. Rev. B **83**, 10 (2011)
328. P.H. Handle, T. Loerting, Phys. Rev. B **93**, 6 (2016)
329. T. Loerting, V.V. Brazhkin, T. Morishita, Adv. Chem. Phys. **143**, 29–82 (2009)
330. J.S. Tse, D.D. Klug, C.A. Tulk, I. Swainson, E.C. Svensson, C.K. Loong, V. Shpakov, V.R. Belosludov, R.V. Belosludov, Y. Kawazoe, Nature **400**(6745), 647 (1999)

331. H. Schober, M.M. Koza, A. Tölle, C. Masciovecchio, F. Sette, F. Fujara, Phys. Rev. Lett. **85**(19), 4100 (2000)
332. J.S. Tse, D.D. Klug, C.A. Tulk, E.C. Svensson, I. Swainson, V.P. Shpakov, V.R. Belosludov, Phys. Rev. Lett. **85**(15), 3185 (2000)
333. M. Fisher, J.P. Devlin, J. Phys. Chem. **99**(29), 11584 (1995)
334. C.R. Hill, C. Mitterdorfer, T.G. Youngs, D.T. Bowron, H.J. Fraser, T. Loerting, Phys. Rev. Lett. **116**, 21 (2016)
335. F. Perakis, K. Amann-Winkel, F. Lehmkuhler, M. Sprung, D. Mariedahl, J.A. Sellberg, H. Pathak, A. Späh, F. Cavalca, D. Schlesinger, A. Ricci, A. Jain, B. Massani, F. Aubree, C.J. Benmore, T. Loerting, G. Grübel, L.G.M. Pettersson, A. Nilsson, Proc. Natl. Acad. Sci. U. S. A. **114**(31), 8193 (2017)
336. V. Fuentes-Landete, L.J. Plaga, M. Keppler, R. Böhmer, T. Loerting, Phys. Rev. X **9**, 1 (2019)
337. C.A. Tulk, J.J. Molaison, A.R. Makhlu, C.E. Manning, D.D. Klug, Nature **569**(7757), 542 (2019)
338. J. Stern, T. Loerting, Sci. Rep. **7**, 1 (2017)
339. J.N. Stern, T. Loerting, Phys. Chem. Chem. Phys. **20**(18), 12589 (2018)
340. J.N. Stern, M. Seidl-Nigsch, T. Loerting, Proc. Natl. Acad. Sci. U. S. A. **116**(19), 9191 (2019)
341. P. Gallo, F. Sciortino, Proc. Natl. Acad. Sci. U. S. A. **116**(19), 9149 (2019)
342. T. Loerting, V. Fuentes-Landete, P.H. Handle, M. Seidl, K. Amann-Winkel, C. Gainaru, R. Böhmer, J. Non-Cryst. Solids **407**, 423 (2015)
343. P.H. Handle, M. Seidl, V. Fuentes-Landete, T. Loerting, Includes response to: "Comment on: Relaxation time of high-density amorphous ice" by GP Johari. Thermochim. Acta **636**, 11 (2016)
344. I. Kohl, E. Mayer, A. Hallbrucker, Phys. Chem. Chem. Phys. **2**(8), 1579 (2000)
345. P. Jenniskens, D.F. Blake, Astrophys. J. **473**(2), 1104 (1996)
346. W. Hage, A. Hallbrucker, E. Mayer, G.P. Johari, J. Chem. Phys. **100**(4), 2743 (1994)
347. K. Winkel, E. Mayer, T. Loerting, J. Phys. Chem. B **115**(48), 14141 (2011)
348. E. Mayer, J. Mol. Struct. **250**(2–4), 403 (1991)
349. E. Mayer, A. Hallbrucker, G. Sartor, G.P. Johari, J. Phys. Chem. **99**(14), 5161 (1995)
350. S. Lemke, P.H. Handle, L.J. Plaga, J.N. Stern, M. Seidl, V. Fuentes-Landete, K. Amann-Winkel, K.W. Köster, C. Gainaru, T. Loerting, R. Böhmer, J. Chem. Phys. **147**(3), 034506 (2017)
351. R.J. Nelmes, J.S. Loveday, T. Strässle, C.L. Bull, M. Guthrie, G. Hamel, S. Klotz, Nat. Phys. **2**(6), 414 (2006)
352. M. Seidl, A. Fayter, J.N. Stern, G. Zifferer, T. Loerting, Phys. Rev. B **91**, 14 (2015)
353. M. Seidl, K. Amann-Winkel, P.H. Handle, G. Zifferer, T. Loerting, Phys. Rev. B **88**, 17 (2013)
354. C.M. Tonauer, M. Seidl-Nigsch, T. Loerting, J. Condens. Matter Phys. **30**(3), 034002 (2017)
355. K. Amann-Winkel, F. Löw, P.H. Handle, W. Knoll, J. Peters, B. Geil, F. Fujara, T. Loerting, Phys. Chem. Chem. Phys. **14**(47), 16386 (2012)
356. F. Löw, K. Amann-Winkel, B. Geil, T. Loerting, C. Wittich, F. Fujara, Phys. Chem. Chem. Phys. **15**(2), 576 (2013)
357. F. Löw, K. Amann-Winkel, T. Loerting, F. Fujara, B. Geil, Phys. Chem. Chem. Phys. **15**(23), 9308 (2013)
358. P.H. Handle, M. Seidl, T. Loerting, Phys. Rev. Lett. **108**, 22 (2012)
359. C. Gainaru, A.L. Agapov, V. Fuentes-Landete, K. Amann-Winkel, H. Nelson, K.W. Köster, A.I. Kolesnikov, V.N. Novikov, R. Richert, R. Böhmer, T. Loerting, A.P. Sokolov, Proc. Natl. Acad. Sci. U. S. A. **111**(49), 17402 (2014)
360. T. Loerting, N. Giovambattista, J. Condens. Matter Phys. **18**(50), R919 (2006)
361. N. Giovambattista, K. Amann-Winkel, T. Loerting, *Amorphous ICES* (Wiley, New York, 2013), pp. 139–173
362. J.C. Palmer, P.H. Poole, F. Sciortino, P.G. Debenedetti, Chem. Rev. **118**(18), 9129 (2018)
363. N. Giovambattista, F. Sciortino, F.W. Starr, P.H. Poole, J. Chem. Phys. **145**(22), 224501 (2016)
364. P.H. Handle, F. Sciortino, N. Giovambattista, J. Chem. Phys. **150**(24), 244506 (2019)
365. N. Giovambattista, F.W. Starr, P.H. Poole, J. Chem. Phys. **147**(4), 044501 (2017)
366. N. Giovambattista, F.W. Starr, P.H. Poole, J. Chem. Phys. **150**(22), 224502 (2019)
367. S. Imberti, A. Botti, F. Bruni, G. Cappa, M.A. Ricci, A.K. Soper, J. Chem. Phys. **122**(19), 194509 (2005)
368. A. Botti, F. Bruni, M.A. Ricci, A.K. Soper, J. Chem. Phys. **125**(1), 014508 (2006)
369. S.E. McLain, S. Imberti, A.K. Soper, A. Botti, F. Bruni, M.A. Ricci, Phys. Rev. B **74**, 9 (2006)
370. L.E. Bove, S. Klotz, J. Philippe, A.M. Saitta, Phys. Rev. Lett. **106**, 12 (2011)
371. A.A. Ludl, L.E. Bove, A.M. Saitta, M. Salanne, T.C. Hansen, C.L. Bull, R. Gaal, S. Klotz, Phys. Chem. Chem. Phys. **17**(21), 14054 (2015)
372. L.E. Bove, F. Pietrucci, A.M. Saitta, S. Klotz, J. Teixeira, J. Chem. Phys. **151**(4), 044503 (2019)
373. B. Prevel, J. Dupuy-Philon, J.F. Jal, J.F. Legrand, P. Chieux, J. Condens. Matter Phys. **6**(7), 1279 (1994)
374. B. Prével, J.F. Jal, J. Dupuy-Philon, A.K. Soper, J. Chem. Phys. **103**(5), 1886 (1995)
375. R. Leberman, A.K. Soper, Nature **378**(6555), 364 (1995)
376. K. Winkel, M. Seidl, T. Loerting, L.E. Bove, S. Imberti, V. Molinero, F. Bruni, R. Mancinelli, M.A. Ricci, J. Chem. Phys. **134**(2), 024515 (2011)
377. G.N. Ruiz, L.E. Bove, H.R. Corti, T. Loerting, Phys. Chem. Chem. Phys. **16**(34), 18553 (2014)
378. G.N. Ruiz, K. Amann-Winkel, L.E. Bove, H.R. Corti, T. Loerting, Phys. Chem. Chem. Phys. **20**(9), 6401 (2018)
379. A.A. Ludl, L.E. Bove, D. Corradini, A.M. Saitta, M. Salanne, C.L. Bull, S. Klotz, Phys. Chem. Chem. Phys. **19**(3), 1875 (2017)
380. M.E. Gallina, L. Bove, C. Dreyfus, A. Polian, B. Bonello, R. Cucini, A. Taschin, R. Torre, R.M. Pick, J. Chem. Phys. **131**(12), 124504 (2009)
381. L.E. Bove, C. Dreyfus, A. Polian, B. Bonello, I. Malfanti, A. Taschin, R. Torre, R.M. Pick, J. Chem. Phys. **134**(3), 034514 (2011)

382. L.E. Bove, C. Dreyfus, R. Torre, R.M. Pick, J. Chem. Phys. **139**(4), 044501 (2013)
383. J. Bachler, P.H. Handle, N. Giovambattista, T. Loerting, Phys. Chem. Chem. Phys. **21**, 23238 (2019)
384. M. de Koning, J. Chem. Phys. **153**(11), 110902 (2020)
385. P.A.F.P. Moreira, R.G.d.A. Veiga, L.d.A. Ribeiro, R. Freitas, J. Helfferich, M. de Koning, Phys. Chem. Chem. Phys. **20**, 13944 (2018)
386. V.F. Petrenko, R.W. Whitworth, *Physics of Ice* (Oxford University Press, New York, 1999)
387. T. Hondoh, A. Higashi, J. Glaciol. **21**(85), 629 (1978)
388. T. Hondoh, A. Higashi, Philos. Mag. A **39**(2), 137 (1979)
389. T. Kobayashi, Y. Furukawa, J. Cryst. Growth **28**(1), 21 (1975)
390. J.P. Perdew, K. Burke, M. Ernzerhof, Phys. Rev. Lett. **77**(18), 3865 (1996)
391. J.L.F. Abascal, E. Sanz, R. García Fernández, C. Vega, J. Chem. Phys. **122**(23), 234511 (2005)
392. J. Klafter, I. Sokolov, *First Steps in Random Walks: From Tools to Applications* (OUP Oxford, 2011)
393. J. Helfferich, I. Lyubimov, D. Reid, J.J. de Pablo, Soft Matter **12**(27), 5898 (2016)
394. E.W. Montroll, G.H. Weiss, J. Math. Phys. **6**(2), 167 (1965)
395. J. Helfferich, F. Ziebert, S. Frey, H. Meyer, J. Farago, A. Blumen, J. Baschnagel, Phys. Rev. E **89**(4), 042603 (2014)
396. J. Helfferich, F. Ziebert, S. Frey, H. Meyer, J. Farago, A. Blumen, J. Baschnagel, Phys. Rev. E **89**(4), 042604 (2014)
397. M. Warren, J. Rottler, EPL **88**(5), 58005 (2009)
398. K. Vollmayr-Lee, R. Bjorkquist, L.M. Chambers, Phys. Rev. Lett. **110**, 017801 (2013)
399. A.R. Verde, J.M.M. de Oca, S.R. Accordino, L.M. Alarcón, G.A. Appignanesi, Eur. Phys. J. E **44**, 47 (2021)
400. S.M.A. Malek, V. Kwan, I. Saika-Voivod, S. Consta, J. Am. Chem. Soc. **143**(33), 13113 (2021)
401. E.A. Cobar, P.R. Horn, R.G. Bergman, M. Head-Gordon, Phys. Chem. Chem. Phys. **14**, 15328 (2012)
402. A. Kananenka, J.L. Skinner, Phys. Chem. Chem. Phys. **22**(32), 18124–18131 (2020)
403. V.M. Castor-Villegas, J. Guevara-Vela, W.E. Vallejo Narváez, Á. Martín Pendás, T. Rocha-Rinza, A. Fernández-Alarcón, J. Comput. Chem. **41**(26), 2266 (2020)
404. P. Partovi-Azar, T.D. Kühne, Phys. Status Solidi B **253**(2), 308 (2015)
405. A. Sauza-de la Vega, T. Rocha-Rinza, J. Guevara-Vela, ChemPhysChem **22**(12), 1269 (2021)
406. R.Z. Khaliullin, T.D. Kühne, Phys. Chem. Chem. Phys. **15**, 15746 (2013)
407. M. Tsanai, P.W.J.M. Frederix, C.F.E. Schroer, P.C.T. Souza, S.J. Marrink, Chem. Sci. **12**, 8521 (2021)
408. M.R. Machado, E.E. Barrera, F. Klein, M. Sónora, S. Silva, S. Pantano, J. Chem. Theory Comput. **15**(4), 2719 (2019)
409. V. Bianco, M. Alonso-Navarro, D. Di Silvio, S. Moya, A.L. Cortajarena, I. Coluzza, J. Phys. Chem. Lett. **10**(17), 4800 (2019)
410. M. De Marzio, G. Camisasca, M.M. Conde, M. Rovere, P. Gallo, J. Chem. Phys. **146**(8), 084505 (2017)
411. S.H. Chen, L. Liu, E. Fratini, P. Baglioni, A. Faraone, E. Mamontov, M. Fomina, Proc. Natl. Acad. Sci. U. S. A. **103**(24), 9012 (2006)
412. K. Winkel, M. Seidl, T. Loerting, L. Bove, S. Imberti, V. Molinero, F. Bruni, R. Mancinelli, M. Ricci, J. Chem. Phys. **134**(2), 024515 (2011)
413. M. Ceriotti, W. Fang, P.G. Kusalik, R.H. McKenzie, A. Michaelides, M.A. Morales, T.E. Markland, Chem. Rev. **116**(13), 7529 (2016)
414. D. Marx, M.E. Tuckerman, J. Hutter, M. Parrinello, Nature **397**(6720), 601 (1999)
415. K. Laasonen, M. Sprik, M. Parrinello, R. Car, J. Chem. Phys. **99**(11), 9080 (1993)
416. J.C. Grossman, E. Schwegler, E.W. Draeger, F. Gygi, G. Galli, J. Chem. Phys. **120**(1), 300 (2004)
417. A.P. Gaiduk, T.A. Pham, M. Govoni, F. Paesani, G. Galli, Nat. Comm. **9**(1), 1 (2018)
418. M. Ceriotti, J. Cuny, M. Parrinello, D.E. Manolopoulos, Proc. Natl. Acad. Sci. U. S. A. **110**(39), 15591 (2013)
419. H.Y. Ko, L. Zhang, B. Santra, H. Wang, W. E, R.A.D. Jr, R. Car, Mol. Phys. **117**(22), 3269 (2019)
420. T.E. Gartner, L. Zhang, P.M. Piaggi, R. Car, A.Z. Panagiotopoulos, P.G. Debenedetti, Proc. Natl. Acad. Sci. U. S. A. **117**(42), 26040 (2020)
421. L. Zhang, H. Wang, R. Car, E. Weinan, Phys. Rev. Lett. **126**, 236001 (2021)
422. P.M. Piaggi, A.Z. Panagiotopoulos, P.G. Debenedetti, R. Car, J. Chem. Theory Comput. **17**(5), 3065 (2021)